

ARS

JOURNAL

A PUBLICATION OF THE AMERICAN ROCKET SOCIETY

LOS ANGELES PUBLIC LIBRARY

VOLUME 30 NUMBER 4

APRIL 1960

APR 29 1960

BIND

SURVEY ARTICLE

Recent Advances in Space Solar Observatory Instrumentation

William A. Rense 313

CONTRIBUTED ARTICLES

- Experiments on the Departure From Chemical Equilibrium in a Supersonic Flow Peter P. Wegener 322
- Transport and Thermodynamic Properties in a Hypersonic Laminar Boundary Layer. Part 2 Applications Sinclair M. Scala and Charles W. Baulknight 329
- Combustion of Highly Reactive Fuels in Supersonic Airstreams Edward A. Fletcher, Robert G. Dorsch and Harrison Allen Jr. 337
- Thermal Control of the Explorer Satellites Gerhard Heller 344
- Minimum Time Flight Paths G. M. Schindler 352
- Combustion Intensity in a Heterogeneous Stirred Reactor Welby G. Courtney 356

TECHNICAL NOTES

- Estimation of Nonequilibrium Reaction Flight Regimes for Blunt Bodies at Hypersonic Speeds T. C. Adamson Jr. 358
- Bloching of Liquids in Cylindrical Tanks of Elliptic Cross Section Wen-Hwa Chu 360
- Simple Formula for Prediction and Automatic Selection R. J. Duffin and T. W. Schmidt 364
- Thermally Induced Bond Strains in Case-Bonded Propellant Grains Eric E. Unger and Bernard W. Shaffer 366
- Short Hypersonic Contour Nozzles R. E. Colgar 368
- Design Method for Spherical Grains H. M. Segal 370
- Curves for Rapid Determination of Orbital Transfer Requirements Philip J. Bonomo 371
- Nonlinear Pressure Oscillations in a Combustion Field Gerald Rosen 422
- Forced Convection Heat Transfer to Gaseous Hydrogen at High Heat Flux and High Pressure in a Smooth, Round, Electrically Heated Tube J. E. McCarthy and H. Wolf 422
- Lateral Speed Indicator Robert L. Sabin 425
- New Method for Studying Polymerization of Solid Propellants and Propellant Binders R. W. Warfield 427

DEPARTMENTS

- Technical Comments 428
- Book Reviews 430
- Technical Literature Digest 433

RUSSIAN SUPPLEMENT 373-420

MAN OUT...

MARTIN-DESIGNED CIRCULAR SPACE COMPUTERS ARE AVAILABLE **FREE** TO INTERESTED PERSONS BY WRITING TO THE SAME ADDRESS.



A fascinating project at Martin-Denver and one which offers to the truly creative engineer or scientist a personal esteem and professional recognition unequalled in today's opportunities. Please do consider being a part of this or other creative involvements at Martin-Denver and inquire of N. M. Pagan, Director of Technical and Scientific Staffing, (Dept. 4B), The Martin Company, P. O. Box 179, Denver 1, Colo.

MARTIN
DENVER DIVISION



NITROGEN TETROXIDE

Tests at Allied Chemical show Nitrogen Tetroxide ready for instant use even after 9 years of storage. Combustion tests with important liquid fuels and Nitrogen Tetroxide indicated up to 99% theoretical combustion efficiency. Additional advantages offered by N_2O_4 are listed at right.

We'll gladly supply technical literature which includes a 59-page Product Bulletin, a brochure entitled "Large Scale Handling of Nitrogen Tetroxide", and "Nitrogen Tetroxide as an Oxidizer in Rocket Propulsion". And, of course, Allied Chemical technical service is always available to users of N_2O_4 .

instantly ready oxidizer
develops up to 99% theoretical I_{sp}!

BASIC TO
AMERICA'S
PROGRESS



NITROGEN DIVISION
Dept. NT 7-12-2 40 Rector Street, New York 6, N. Y.

For specifications and local offices, see our insert in Chemical Materials Catalog, pages 475-482, and in Chemical Week Buyers Guide, pages 37-44.

- Requires no refrigeration — can be stored indefinitely in missile at launching site.

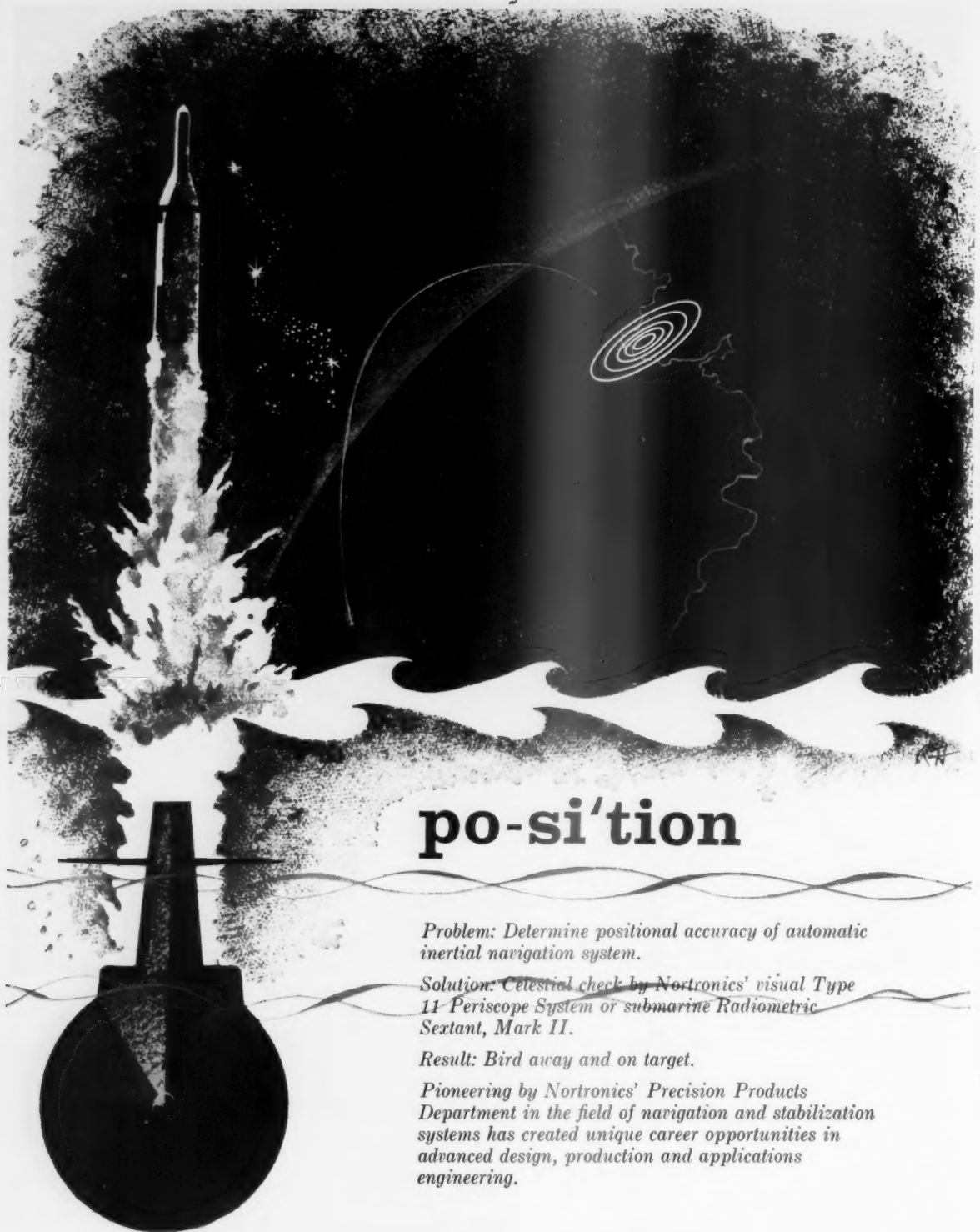
- Hypergolic with amine-type fuels — ignition is simple and reliable.

- Can be used with most fuels — including those containing carbon.

- Eliminates rough starts — which are due to accumulation of unreacted propellants in thrust chamber.

- Motors are throttleable — when N_2O_4 is used as the oxidizer.

- Immediate availability — Allied Chemical Nitrogen Tetroxide is shipped in 125- and 150-lb. steel cylinders, 1-ton containers, 30- and 50-ton tank cars.



po-si'tion

Problem: Determine positional accuracy of automatic inertial navigation system.

Solution: Celestial check by Nortronics' visual Type 11 Periscope System or submarine Radiometric Sextant, Mark II.

Result: Bird away and on target.

Pioneering by Nortronics' Precision Products Department in the field of navigation and stabilization systems has created unique career opportunities in advanced design, production and applications engineering.



NORTRONICS

A Division of **NORTHROP CORPORATION**

**PRECISION PRODUCTS DEPARTMENT
NORWOOD, MASSACHUSETTS**

Field Offices

Highway #46 2486 Huntington Drive
Teterboro, New Jersey San Marino, California

ARS JOURNAL

A PUBLICATION OF THE AMERICAN ROCKET SOCIETY

EDITOR Martin Summerfield

ASSOCIATE TECHNICAL EDITOR

Irvin Glassman

MANAGING EDITOR

Barbara Nowak

ART EDITOR

John Culin

CONTRIBUTOR

George F. McLaughlin

ASSOCIATE EDITORS

J. George Adashko, *Russian Supplement*; Ali Bulent Cambel, *Northwestern University, Book Reviews*; Charles J. Mundo Jr., *Raytheon Manufacturing Co., Guidance*; Bernard H. Pajewonsky, *Aeronautical Research Associates of Princeton, Flight Mechanics*; M. H. Smith, *Princeton University, Technical Literature Digest*

ASSISTANT EDITORS

Julie Hight, Estelle Metz, Carol Rubenstein

ADVERTISING AND PROMOTION MANAGER

William Chenoweth

ADVERTISING PRODUCTION MANAGER

Walter Brunke

ADVERTISING REPRESENTATIVES

New York

D. C. Emery and Associates
400 Madison Ave., New York, N. Y.
Telephone: Plaza 9-7460

Chicago

Jim Summers and Associates
35 E. Wacker Dr., Chicago, Ill.
Telephone: Andover 3-1154

Boston

Robert G. Melendy
17 Maugas Ave., Wellesley Hills, Mass.
Telephone: Cedar 5-6503

Los Angeles
James C. Galloway and Co.
6535 Wilshire Blvd., Los Angeles, Calif.
Telephone: Olive 3-3223

Detroit
R. F. Pickrell and Vincent Purcell
318 Stephenson Bldg., Detroit, Mich.
Telephone: Trinity 1-0790

Pittsburgh
John W. Foster
239 4th Ave., Pittsburgh, Pa.
Telephone: Atlantic 1-2977

American Rocket Society

500 Fifth Avenue, New York 36, N. Y.

Founded 1930

OFFICERS

President
Vice-President
Executive Secretary
Treasurer
Secretary and Asst. Treasurer
General Counsel
Director of Publications

Howard S. Seifert
Harold W. Ritchey
James J. Harford
Robert M. Lawrence
A. C. Slade
Andrew G. Haley
Irwin Hersey

BOARD OF DIRECTORS

Terms expiring on dates indicated

Ali B. Cambel	1962	William H. Pickering	1961
Richard B. Canright	1962	Simon Ramo	1960
James R. Dempsey	1961	William L. Rogers	1960
Herbert Friedman	1962	David G. Simons	1961
Robert A. Gross	1962	John L. Sloop	1961
Samuel K. Hoffman	1960	Martin Summerfield	1962
A. K. Oppenheim	1961	Wernher von Braun	1960
Maurice J. Zucrow		1960	

TECHNICAL COMMITTEE CHARMEN

Lawrence S. Brown, Instrumentation and Control	David B. Langmuir, Ion and Plasma Propulsion
Ali B. Cambel, Magnetohydrodynamics	Max A. Lowy, Communications
William H. Dorrance, Hypersonics	Irving Michelson, Education
James S. Farris, Guidance and Navigation	Peter L. Nichols Jr., Propellants and Combustion
Herbert Friedman, Physics of the Atmosphere and Space	Eugene Perchonok, Ramjets
George Gerard, Structures and Materials	Richard A. Schmidt, Test Facilities and Support Equipment
Martin Goldsmith, Liquid Rockets	John I. Shafer, Solid Rockets
Andrew G. Haley, Space Law and Sociology	C. J. Wang, Nuclear Propulsion
Samuel Herrick, Astrodynamics	Stanley C. White, Human Factors and Bioastronautics
Maxwell W. Hunter, Missiles and Space Vehicles	George F. Wislicenus, Underwater Propulsion
Herbert L. Karach, Systems Operations and Support	Abe M. Zarem, Power Systems



po-si'tion

A NOTE FOR TALENTED ENGINEERS:

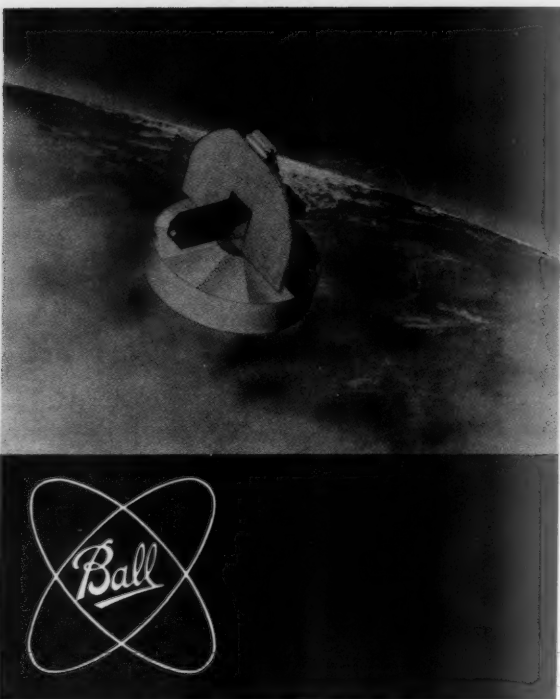
We invite your inquiry as to important positions that exist at Nortronics' Precision Products Department (formerly the Military Products Division of American-Standard).

Plan your future with Nortronics' Norwood team and stimulate your professional growth. If you can qualify in one of several electro-mechanical areas you will work on challenging programs with professionally dedicated associates.

FOOTNOTE: Excellent salaries for qualified engineers in both our Systems and Components Groups.

Contact E. P. REARDON, NORTRONICS Precision Products Department, Norwood, Massachusetts

 **NORTRONICS**
A Division of NORTHROP CORPORATION



CONTRACT RESEARCH, DEVELOPMENT, FABRICATION

Specializing in the fields of

- Rocket and Satellite Instrumentation
- Payload Systems
- Solar and Stellar Pointing Systems
- Guidance and Control Systems

WRITE FOR BROCHURE

 Prime Contractors to the
NASA, Air Force, Navy

Employment Opportunities Available
for Scientists and Engineers with Above
Average Abilities

BALL BROTHERS RESEARCH CORP.
INDUSTRIAL PARK BOULDER, COLORADO
Hillcrest 2-2966

Scope of ARS JOURNAL

This Journal is devoted to the advancement of astronauts through the dissemination of original papers disclosing new scientific knowledge and basic applications of such knowledge. The sciences of astronautics are understood here to embrace selected aspects of jet and rocket propulsion, spaceflight mechanics, high speed aerodynamics, flight guidance, space communications, atmospheric and outer space physics, materials and structures, human engineering, overall system analysis, and possibly certain other scientific areas. The selection of papers to be printed will be governed by the pertinence of the topic to the field of astronautics, by the current or probable future significance of the research, and by the importance of distributing the information to the members of the Society and to the profession at large.

Information for Authors

Manuscripts must be as brief as the proper presentation of the ideas will allow. Exclusion of dispensable material and conciseness of expression will influence the Editors' acceptance of a manuscript. In terms of standard-size double-spaced typed pages, a typical maximum length is 22 pages of text (including equations), 1 page of references, 1 page of abstract and 12 illustrations. Fewer illustrations permit more text, and vice versa. Greater length will be acceptable only in exceptional cases.

Short manuscripts, not more than one quarter of the maximum length stated for full articles, may qualify for publication as Technical Notes or Technical Comments. They may be devoted to new developments requiring prompt disclosure or to comments on previously published papers. Such manuscripts are published within a few months of the date of receipt.

Sponsored manuscripts are published occasionally as an ARS service to the industry. A manuscript that does not qualify for publication, according to the above-stated requirements as to subject, scope or length, but which nevertheless deserves widespread distribution among jet propulsion engineers, may be printed as an extra part of the Journal or as a special supplement, if the author or his sponsor will reimburse the Society for actual publication costs. Estimates are available on request. Acknowledgment of such financial sponsorship appears as a footnote on the first page of the article. Publication is prompt since such papers are not in the ordinary backlog.

Manuscripts must be double spaced on one side of paper only with wide margins to allow for instructions to printer. Include a 100 to 200 word abstract. State the authors' positions and affiliations in a footnote on the first page. Equations and symbols may be handwritten or typewritten; clarity for the printer is essential. Greek letters and unusual symbols should be identified in the margin. If handwritten, distinguish between capital and lower case letters, and indicate subscripts and superscripts. References are to be grouped at the end of the manuscript and are to be given as follows. For journal articles: Authors first, then title, journal, volume, year, page numbers; for books: Authors first, then title, publisher, city, edition and page or chapter numbers. Line drawings must be clear and sharp to make clear engravings. Use black ink on white paper or tracing cloth. Lettering should be large enough to be legible after reduction. Photographs should be glossy prints, not matte or semi-matte. Each illustration must have a legend; legends should be listed in order on a separate sheet.

Manuscripts must be accompanied by written assurance as to security clearance in the event the subject matter lies in a classified area or if the paper originates under government sponsorship. Full responsibility rests with the author.

Preprints of papers presented at ARS meetings are automatically considered for publication.

Submit manuscripts in duplicate (original plus first carbon, with two sets of illustrations) to the Managing Editor, ARS JOURNAL, 500 Fifth Avenue, New York 36, N.Y.

ARS JOURNAL is published monthly by the American Rocket Society, Inc. and the American Interplanetary Society at 20th & Northampton Sts., Easton, Pa., U. S. A. Editorial offices: 500 Fifth Ave., New York 36, N.Y. Price: \$12.50 per year, \$2.00 per single copy. Second-class mail privileges authorized at Easton, Pa. This publication is authorized to be mailed at the special rates of postage prescribed by Section 132.122. Notice of change of address should be sent to the Secretary, ARS, at least 30 days prior to publication. Opinions expressed herein are the authors' and do not necessarily reflect the views of the Editors or of the Society. © Copyright 1960 by the American Rocket Society, Inc.

Recent Advances in Space Solar Observatory Instrumentation

WILLIAM A. RENSE

University of Colorado
Boulder, Colo.

THE GREAT advances which have been made in the design of space missiles in the past few years have emphasized the feasibility of establishing a space observatory for the measurement and study of radiations from the celestial bodies. Moreover, the problem of the design and construction of instruments that are functional and efficient in a space environment has already been largely solved. The development of dependable and accurate pointing controls for small and large instruments has proceeded to the point where minor, though difficult, details remain to be worked out. In addition, one cannot overlook the importance of obtaining scientific data from measurements at vantage points outside Earth's atmosphere. We have only to follow the accelerated progress of upper air physics and astrophysics since the time of rocket and satellite measurements, crude though some of them are, to realize the impact of the new dimension that has been added to man's means of studying the physical universe.

The motivations behind this movement into space are many and varied. Certainly one of them is based on the natural curiosity of man about the world around him. In this age of practicality and purposeful thinking it is probably more necessary than ever that we make concessions to the space scientists who wish to further our basic understanding by pursuing the accepted methods of scientific research in a direction which might seem at the moment to be unnecessary and even somewhat naive.

The purpose of this paper is to present a realistic picture of the instrumentation of a possible space solar observatory and to sketch some of the engineering and scientific problems behind the functioning of such an observatory. Emphasis will be placed on optical devices for the study of solar electromagnetic radiation from the x-ray region of the solar spectrum through the ultraviolet, visible and infrared.* We are not concerned with the missile techniques needed for the successful launching of such an observatory or for its stabilization. Problems (1, 2)¹ of pointing the instruments and their temperature control are not discussed. Some time will be spent indicating how the data will contribute to the advancement of astrophysics. Mention will be made of some current results about solar radiation as obtained from rocket and satellite flights. In conclusion specific instrumentation of an imaginary space solar observatory will be briefly considered.

This paper is a modified version of ARS Preprint no. 795-59, presented at the ARS Semi-Annual Meeting, June 8-11, 1959, San Diego, Calif.

* Numbers in parentheses indicate References at end of paper.

Photon Counters

A photon counter is (3) a modified Geiger-Mueller device adapted to the detection of ultraviolet and x-ray radiation over either a broad or a narrow band. It has been successfully employed as a rocket instrument for the measurement of solar radiation. The essential features are shown in Fig. 1. Its action is as follows: The window cuts off radiation below a certain wave length and permits the remaining photons to enter a chamber which is filled with an appropriate gas mixture at a suitable pressure. The photons may cause ionization in the gas, or they may strike the cathode material and produce photoelectrons. Either event may initiate a Townsend discharge and cause a count. The voltage across the anode and cathode, the gases used, their partial pressures, and the nature of the cathode material are important factors in determining the detailed response. Low energy photons which get through the window cannot ionize the gas, but can cause the emission of electrons from the surface of the cathode; for these longer wave lengths the quantum yield of the tube may be of the order of one count per 10^6 photons. As the energy of the photons increases, the internal photoelectric effect occurs at the cathode, and the yield rises rapidly unless the gas is a strong absorber in this wave length region. By the time photo-ionization of the gas sets in, the quantum yield may be as high as one count per 5×10^3 photons. A rise to about one count per 100 photons is achieved as soon as the energy of the photons is sufficient to ionize the gas. Experiments indicate that electrons emitted by the ionization process are much more effective in inducing discharges, and hence counts, than those released by photoelectric emission at the cathode.

Other factors besides the value of the ionization potential are important in determining the kind of gas with which the tube is filled. For example, if a trace of a halogen gas is present along with the bulk gas (usually a rare gas such as neon or helium) the quantum yield is known to be greatly reduced in certain wave length regions, usually at the very short (gamma ray) and the relatively long (1250 Å) wave length regions. The partial pressure of the halogen gas has a great deal to do with this quenching effect; in general this effect increases with increase in partial pressure. HCl, NO and other gases which can acquire electrons easily have effects similar to those of the halogens. It is believed that the molecules of gases which exhibit the forementioned type of quenching effect combine with some of the electrons created

William A. Rense studied engineering physics at Case Technology in Cleveland, where he received the B.S. degree in 1935. His M.S. and Ph.D. degrees in physics were received at Ohio State University in 1937 and 1939, respectively. In the following years he taught at several universities, including Louisiana State University, Rutgers University and the University of Colorado, where he is, at present, Professor of Physics and Director of the Upper Air Laboratory of the Physics Department. For the past 10 years he has been active in research in the fields of solar ultraviolet spectroscopy and upper air physics.

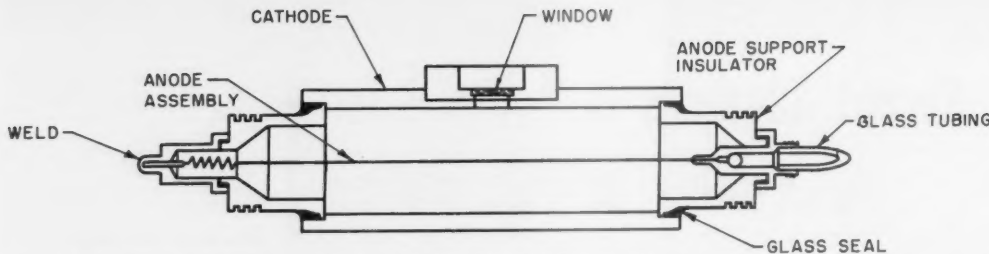


Fig. 1 A diagram of a typical photon counter after Chubb and Friedman (3). Radiation enters the window, passes through the gas in the tube, and finally strikes the cathode surface. The action is similar to that of a Geiger counter

by the incident photons and carry them to the anode without inducing a discharge. In the case of the halogen molecules the electron capture is accompanied by dissociation, and the atoms carry the electrons.

A knowledge of these principles and the parameters of the available cathode materials, windows and gases enables one to design a photon counter which will detect a desired spectral band, narrow or broad.

Normal and Grazing Incidence Grating Spectrographs

For dispersion and image formation involving radiation of wave lengths less than 1100 Å, prisms and lenses cannot be used because of the absence of known bulk materials that transmit in that spectral region. Recourse must be made to reflection optics; reflection gratings replace prisms, and mirrors replace lenses. For rocket and satellite measurements, grating spectrographs have been designed which are basically the same as those previously used in laboratory research in vacuum ultraviolet spectroscopy.

There are two main obstacles which one faces when dealing with reflection optics: First, the reflectivity of most coatings is very low in the far ultraviolet except when angles of incidence are large, and second, the elimination of aberrations, especially when grazing incidence is involved, is a difficult task. Both of these problems have been tackled since the advent of space solar ultraviolet spectroscopy, and have been partially solved. Some of the recent interesting information concerning the solar spectrum has been obtained as a result of the new design of reflection-type spectrographs.

The concave reflection grating, because of its self-focusing powers (thus eliminating the need for additional mirrors or lenses), is especially suitable for ultraviolet spectrography. In addition to the concave grating, all that is required is a slit and a detector. Fig. 2 shows diagrammatically the Rowland circle-type mounting. The slit, the center of the grating and the spectrum receiving surface are all on a circle called the Rowland circle whose diameter is equal to the radius of curvature of the grating. Light from the source passes through the slit, strikes the grating and is brought to a focus on the Rowland circle. Actually, because of astigmatism, there are two focal points involved, one on the Rowland circle and the other beyond the circle. The first corresponds to horizontal focus for an image of the slit, and the second to vertical focus for the source. Referring to Fig. 2 for the meaning of the symbols, one can write the equations which locate the two astigmatic images

$$r = R \cos \alpha \quad r' = R \cos \beta$$

$$\frac{1}{r} - \frac{\cos \alpha}{R_e} + \frac{1}{r_e'} - \frac{\cos \beta}{R} = 0$$

[1]

One notes that for very small angles of incidence and diffraction the two images are close to coincidence when the source is at the slit. Likewise for angle of incidence of about 45 deg, with a source at infinity, a stigmatic image can be found (4). Insofar as photographic detection is concerned, this fact helps decrease the length of the lines of a spectrum, and hence increases the density of the image. A spectrograph utilizing this feature is the normal-incidence type (5); for such solar

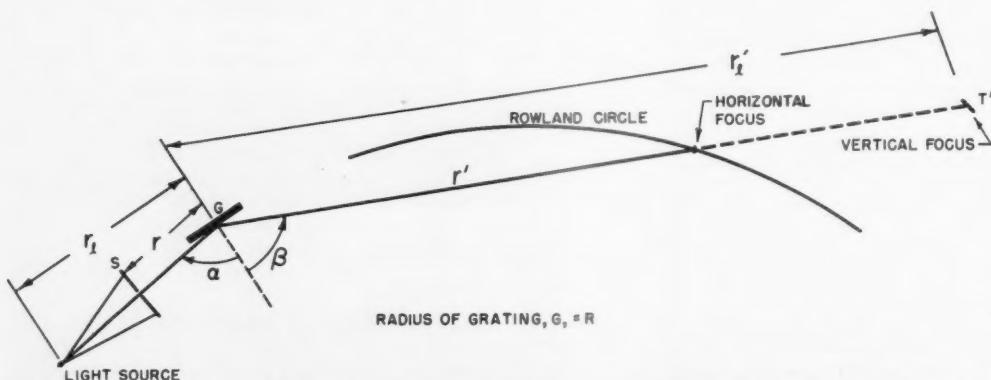


Fig. 2 A diagram of the essential optical parts of a concave grating ultraviolet spectrograph. Some of the light from the source passes through the slit S onto the grating G . The spectrum (horizontal focus) is formed along the so-called Rowland circle whose diameter is equal to the radius of the grating. Vertical focus of a line would occur at T' beyond the Rowland circle

spectrographs the sun's image must be focused on the slit by an auxiliary mirror to insure stigmatic quality. On the other hand, it is a well-known fact that radiation in the extreme ultraviolet is not reflected with high efficiency at small angles of incidence. One would therefore like to set a grating for large angles of incidence, in particular at angles 80 deg or greater (grazing incidence) because under these conditions reflectivity is high in the far ultraviolet. For grazing incidence astigmatism is very great, and the spectral lines are so long that considerable loss in overall speed is experienced when photographic detection is required. Thus the dilemma is, for normal incidence, small aberration but low reflectivity in the far ultraviolet; for grazing incidence, high reflectivity in the far ultraviolet, but large aberration.

The problem of low reflectivity in the far ultraviolet has been tackled by several groups (6-8) with encouraging results. Films have been found which increase the reflectivity near normal incidence. Zinc sulfide films and magnesium fluoride coatings on aluminum are examples. Unlike the case of aluminum, whose reflectivity in the ultraviolet falls off rapidly with age, these films retain their high reflectivities for long periods. Thus at 1000 Å reflectivity for aluminum at near normal incidence is 9 per cent, whereas for a zinc sulfide coating the reflectivity is 18 per cent. The reflectivity for the magnesium fluoride coating is even higher, rising to about 50 per cent.

A method has been worked out for reducing the astigmatism in a grazing-incidence spectrograph (9). Referring to Equations [1], one finds that for r_e equal to infinity (sun) the condition that the horizontal and vertical focus both fall on the Rowland circle is impossible for grazing incidence angles when gratings with reasonable curvature are employed. In fact, light must be converging on the grating in order to eliminate astigmatism. Thus, substituting $r_e' = r'$ in Equations [1] one finds that

$$r_e = R/(\cos \alpha - \sin \beta \tan \beta) \quad [2]$$

For a typical case where $R = 50$ cm, $\alpha = 85$ deg, $\beta = 78$ deg (corresponding to 300 Å radiation when the grating constant is 6000 lines/cm) one finds that the source distance for vertical focus on the Rowland circle is about -11 cm, and therefore that a virtual source must be used. For obtaining a virtual image of the sun at the proper distance behind the grating from the slit, a toroidal mirror of suitable radii of curvature may be positioned in front of the slit. To insure high reflectivity in the far ultraviolet, the mirror, like the grating, is set for grazing incidence. From the equations for the distances of the astigmatic foci of a spherical mirror it is possible to choose the radii of the toroidal mirror so that the horizontally focused image of the sun is at the slit and the vertically focused image is at the required point beyond the grating. Thus, for the case referred to above at 300 Å, the radii are 46 and 2.7 cm, respectively.

A rocket grazing incidence spectrograph is shown in Fig. 3. In this instrument the film (SWR Eastman Kodak) is fed through the Rowland circle onto the roll-up spindle in the steel cassette. The exposure times for the successive spectrograms during a rocket flight are determined by a timer which automatically opens a shutter after the film is moved between exposures. The grating is a replica on red glass, uncoated, made from a master of 6000 lines/cm and radius 100 cm by Bausch and Lomb Optical Co.

High Resolution Spectrographic Devices

High resolution spectra of celestial sources yield very valuable data for the astrophysicist whose equations often call for detailed information on line profiles, distribution of intensity of light in the source, exact wave lengths and related parameters. Attempts have been made to develop high resolution spectrographs for rocket spectroscopy,

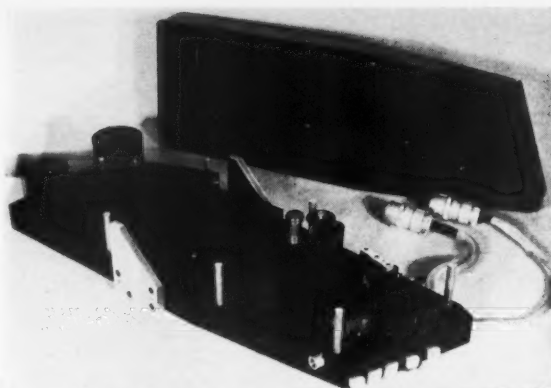


Fig. 3 A rocket ultraviolet spectrograph of the grazing-incidence type. The slit, grating, Rowland circle and film winding mechanism are visible. Film is automatically wound into a light-tight steel cassette. The photoeyes which were used in pointing the instrument at the sun are visible on the grating end of the spectrograph

though most of the research to date has centered around high speed, low resolution instruments.

The resolving power for a given wave length λ is defined as the ratio of λ to $\Delta\lambda$, where $\Delta\lambda$ is the difference in wave length between two spectral lines which can just be resolved by the detector. Many factors help control the resolving power for a given spectrograph. The slit width is one; others are the grating itself and the kind of detector used. For rocket instruments employed recently, the slit width is the real limiting element, along with the grating constants. When the grating determines the resolving power, one can calculate the approximate value of $\lambda/\Delta\lambda$ by multiplying the spectral order of the line by the number of rulings on the grating. A typical rocket spectrograph grating might have a constant of 12,000 lines/cm and a ruled area 3×3 cm. For the first order the resolving power might therefore be as high as 36,000. For solar hydrogen Lyman-alpha radiation (1216 Å) a spectral separation of 0.034 Å could be achieved. For higher orders a correspondingly smaller separation could be effected. The possibility of the use of high orders to increase the resolving power is limited by the ability of the manufacturer of the grating to blaze the grating, that is, to shape the reflection grooves so that they can concentrate the light in a given direction. Other limitations arise from overlapping orders (ultraviolet lines falling on the strong continuum in the visible) and scattered light. Some of these difficulties were overcome in a rocket instrument recently flown (10). The object was to obtain high resolution spectra of the solar hydrogen Lyman-alpha line at 1216 Å. Two gratings were used, both blazed, one for the first order and the other for the thirteenth order. A magnesium fluoride coating increased the reflectivity of the gratings which were set for nearly normal incidence. The first grating focused the line in the first order on the slit of the second grating which formed the final stigmatic image on specially sensitized film. In this way, overlapping orders and scattered light problems were reduced. The absorption center in the Lyman-alpha line was discovered on this flight (Fig. 4).

Perhaps the most interesting type of high resolution spectrograph suitable for satellite and rocket observations is one which employs a special kind of grating known as a reflection echelle.² The use of the latter enables the designer to con-

² Now made available by Bausch and Lomb Optical Co. as a result of a technique of ruling developed by G. R. Harrison at MIT.

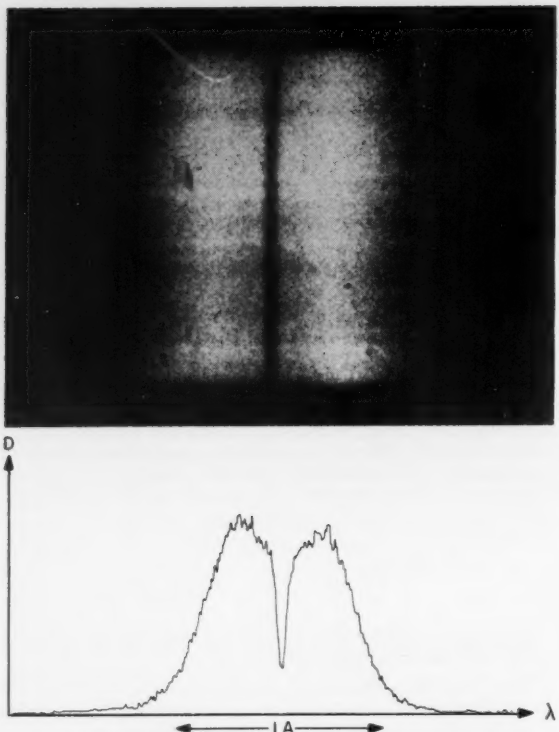


Fig. 4 A high dispersion photograph of the hydrogen Lyman-alpha line at 1216 Å taken by a Naval Research Laboratory group (10). The instrument was a spectrograph employing a grating set for the thirteenth order at Lyman-alpha. A photometric tracing of the line is shown below the photograph

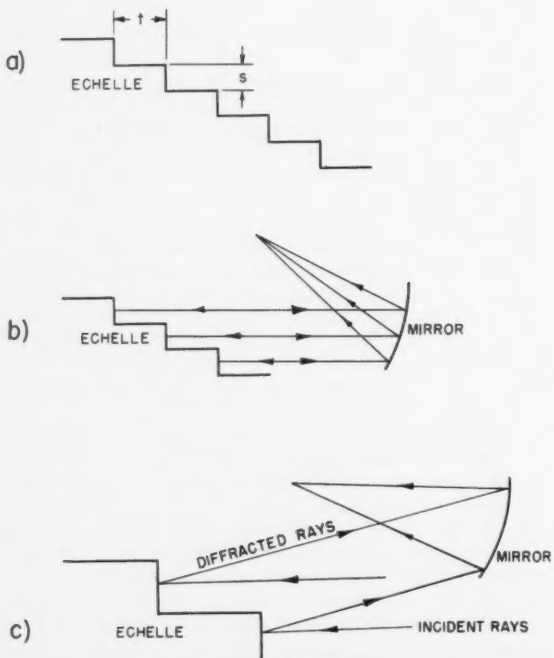


Fig. 5 Illustration of the principle of the echelle grating

ceive of a small compact instrument that can attain resolving powers of the order of several hundred thousand or even a million in the visible and ultraviolet. Optically there are two ways of regarding the echelle; one may consider it to be a coarse ruled grating with a strong blaze in one direction corresponding to a high order, or one may regard it as a multiple reflection interference device. With the aid of Fig. 5 we will describe it from the latter point of view. In Fig. 5a the echelle is represented as a steplike structure having $s = 0.6105 \times 10^{-3}$ cm, $t = 2s$ for a typical case. There may be as many as 10^4 reflection strips for the whole echelle. Assuming that a plane wave strikes the strips normal to the s surface, the diffracted light from each strip is strongly concentrated along the normal to the latter. A mirror, as in Fig. 5b, concentrates the light from all strips to a common focus. If $\lambda = 2t$, the phase difference between adjacent rays is 360 deg and the order m is one. However, t may be about 1.221×10^{-3} cm, so that for the ultraviolet (1216 Å) the order is about 201. At normal incidence, then, the resolving power at 1216 Å for a typical echelle having 10^4 steps would be $(10^4)(201)$ or 2×10^6 . Two lines having a separation of less than 0.001 Å could be resolved in this ultraviolet region. For angles of diffraction not zero, as shown in Fig. 5c, the same order calls for smaller wave lengths, so that the spectrum of the source will be spread along a direction perpendicular to the lines of the steps. Also, at normal incidence one can find a wave length for which reinforcement occurs by shifting to a different order: $2t = (m \pm n)\lambda$, where n is 1, 2, 3, etc. To prevent overlapping of orders a regular grating is "crossed" with the echelle so as to separate the various orders at right angles to the echelle dispersion. A working arrangement is shown in Fig. 6. Here the light from the sun is focused on the slit and strikes a concave grating set for the Wadsworth-type mounting.³ The grating disperses the radiation and collimates it. The echelle then introduces dispersion at right angles to that produced by the concave grating and redirects the light to the latter. A focus is effected near the entrance slit. To reduce scattered light the collecting mirror can be another concave grating which throws its spectrum in a selective manner on the slit. With a resolving power of 2×10^6 it would be possible to detect a Doppler shift corresponding to a relative motion of the source of about 0.15 km/sec.

Echelle spectrographs suitable for solar ultraviolet detection from rockets or satellites are now under construction. One employing a calcium fluoride prism for the near solar ultraviolet has already been successfully flown (11).

³ For such a mounting a distant monochromatic source is stigmatically imaged on the normal to the grating for the appropriate angle of incidence.

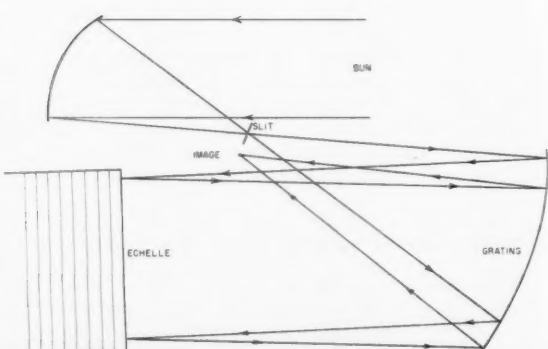


Fig. 6 The optical arrangement of the essential parts of a space observatory high resolution echelle spectrograph

When the echelle is to be regarded as a grating (12), the regular grating equation applies

$$m\lambda = d(\sin i + \sin j) \quad [3]$$

where $d = (s^2 + t^2)^{1/2}$. When the incident ray comes in at right angles to the s surface, then $i = \kappa$ where $\kappa = \tan^{-1} t/s$; then for a diffracted ray also at right angles to the latter surface the equation above becomes $m\lambda = 2d \sin \kappa$, which reduces to $2t$ in accordance with the previous results. It might also be mentioned that, when the incident rays strike the s surface at a grazing angle θ in the horizontal plane, the usual formulas hold, except that s must be replaced by an effective value s' equal to $s \cos \theta$, and that the slit must be rotated by an angle T given by $\tan T = 2t/s \sin \theta$. The fact that θ need not be zero deg without deleterious optical effects means that the echelle may be utilized in a variety of mountings. For example, by setting θ large (grazing incidence) good reflectivity in the ultraviolet is possible and high resolution of the solar 303.8 Å HeII line may be achieved.

Detection of Infrared

Infrared radiation is emitted by all bodies whose temperatures are not absolute zero. For this reason its measurement poses special problems because a detector receives the radiation from many sources besides the one being studied. Consequently, except for such cases as strong, narrow band, infrared sources which filters can help isolate, one goes about detecting infrared radiation from a given source by first measuring the total radiation from the source and its surroundings and then the radiation with the source "cut off" as effectively as possible. It is just as though one were to attempt to measure a visible light source with an optical instrument whose inner walls and baffles were coated with luminous paint.

By infrared is usually meant that part of the electromagnetic spectrum which extends from the visible at 7000 Å to the microwave region where wave lengths are of the order of 1 mm or greater. The customary unit for measurement of wave length in the infrared is the micron ($1 \mu = 10^4 \text{ Å}$). Black bodies emit infrared radiation in increasing amounts as the temperature is raised; although only for relatively low temperatures does the wave length corresponding to the peak of the radiation continuum fall in the infrared.

An infrared detector is characterized by two quantities, the responsivity and the detectivity. The former is the voltage per watt per square centimeter on the detector; the latter is basically the signal to noise ratio of the device. Most infrared detectors (13-15) are solids of the photoconducting type. The electric conductivity changes when infrared radiation strikes the sensitive surface. In many cases the radiation is chopped before striking the receiver so that a-e amplification techniques can be utilized for detection. When cooled, these detectors have increased sensitivity.

A very sensitive detector with unusually rapid response is the germanium "gold-doped" photoconductor developed at Westinghouse. One part of gold is added to about one hundred million parts of germanium. The detectivity is high between 1 and 9μ .

Between 1.8 and 4μ the class of infrared photoconductors which includes lead sulfide, lead telluride and lead arsenide is effective, especially when cooled. In fact, miniature cooling systems have been designed for them.

Only bolometer-type infrared detectors are effective in the far infrared, and these have been employed in rocket instruments (14) to measure radiation of wave lengths between 9 and 30μ . The response time for bolometers is not fast unless the elements are very small; on the other hand bolometers are not good black bodies in the infrared unless they are relatively thick. In most instances the desired response of the bolometer to infrared radiation is that of a change of resistance with heating, or the generation of an emf (16).

A typical bolometer (14) is the flake thermistor bolometer with a 1-mm² receiving area and a 1.5-millisecond time constant. The unit consists of two flakes connected in series. Bias is supplied by a d-c potential, and the signal is drawn from the junction point. One flake acts as the compensating flake. This detector has a high output voltage for a given intensity of incident radiation and gives nearly constant spectral sensitivity over the infrared region. No cooling is required. However, compared to other infrared detectors, the time constant and detectivity are not always satisfactory.

Dispersion in the infrared region may be effected by reflection gratings or prisms made of suitable materials. Mirrors are satisfactory for collimating or focusing purposes, since mirror surface coatings may be made with high reflectivity in the infrared. Lenses are also available for infrared optics. For compact, fast instruments the spectral range to be studied is best isolated by means of filters. Both band pass and low pass infrared filters (17-20) have been designed and made. They consist of alternate layers of materials of high and low index of refraction vacuum-deposited on a supporting substrate. Ordinary electromagnetic interference theory such as that applicable to the Fabry-Perot interferometer explains the action of the filter. Analog computer methods (19) have been developed for carrying out the calculations involved in the design of a multilayer filter.

X-Ray Spectrographs

Solar x-rays and ultraviolet radiation have been detected in the range 100 to 1 Å by photon counters (3, 21) and by grazing incidence grating spectrographs (22). The latter are not effective below about 10 Å. Rocket and satellite x-ray spectrographs employing crystals have been designed by several groups including Ball Brothers Research Corp. (Rosendahl) and Air Force Cambridge Research Center (Miczaika). The general principle of such spectrographs is similar to that of the grating spectrograph with a bent crystal acting as the diffracting element. Bragg's law gives the diffraction angle. For mica in the first order the crystal plane spacing is 9.845 Å. Mica is suitable to about 18 Å beyond which wave length its dispersion becomes unmanageable. For the range extending from this point up to about 100 Å no known inorganic crystals have sufficiently high values of d to overcome the difficulty. However, organic crystals such as that of melissic acid used by Dauvillier are suitable if they do not have too low a melting point.

Image Formation

In order to transmit images of the sun or parts of the sun from the space observatory to Earth one must solve the problems of (a) image formation by optical devices, (b) amplification of the image if it is intrinsically faint, and (c) transmission of the image by electromagnetic waves to Earth. We will be concerned here only with (a) and (b).

Of interest is the formation of an image of the sun's disk in monochromatic ultraviolet radiation. Both lithium fluoride (23) and grating cameras (24) have been used for this purpose. In the former (25), a prism separates the radiation corresponding to the various solar ultraviolet emission lines by dispersion; a second prism then neutralizes the dispersion before a lens forms the final image. In a form of the grating camera (24) a stigmatic image of the sun is formed in radiation corresponding to a given solar ultraviolet line (such as the intense hydrogen Lyman-alpha line at 1216 Å) by a concave grating mounted in the Wadsworth-type arrangement. A small aperture encompassing this image prevents scattered light from entering the final image region. The final image is formed by a second grating ruled on a suitable toroidal surface. (The toroidal surface may be produced from a concave grating by mechanical stress of the mount.) Aberrations are present which prevent the achievement of high

resolving power. Other forms of grating cameras have been designed (26).

In the visible and infrared region where filters can be found, the problem of good image quality is much more easily solved. In the extreme ultraviolet a camera must employ gratings set at grazing incidence in order to get high reflectance. Here the reduction of aberrations is even more serious, but some success can be realized by proper choice of grating constants, spacing and radii.

A faint image formed by the optical elements cannot be transmitted to Earth unless an image amplifier of some kind is used. Of course, if the faint image were photographed and automatically developed, the image could be transmitted by an electronics scanning device. A better procedure would be to utilize an image amplifier first, and then to transmit the picture by television techniques or some modification thereof.

Several manufacturers are experimenting with image amplifiers. One of the latter made by Radio Corporation of America and based on Lollemand's method will be briefly described in order to display the principles and kinds of problems involved (27). A multi-alkali photocathode receives the faint image from the optical component part of the camera. The ejected electrons are focused by an electrostatic lens on a phosphor screen separated from another photocathode by a thin film of glass. The electrons ejected from the second photocathode are then focused by another electrostatic lens on a second phosphor screen to form the final image. The arrangement is called a cascaded image converter. The glass sandwich in the center is the intensifying membrane. At present, the main disadvantage of such tubes lies in the low resolving power introduced by graininess and nonuniformity of the phosphor screens. The gain is not high (practically, of the order of about five), and the useful field size is small. These tubes have been used, however, to photograph the planet Mars at Lowell Observatory in times of the order of $\frac{1}{300}$ sec, in order to avoid atmospheric smearing.

Recently progress has been made in the transmitting of infrared images. One of the ideas that appears to be leading to successful results centers around the use of an infrared sensitive material for conversion of the infrared image into a temperature matrix which can be scanned like a television

camera tube. Lateral heat conduction is reduced in such a converter by the use of extremely thin films such as aluminum oxide films about 40 molecules thick developed at Westinghouse Research Laboratories. Another sensitive material that can be used as a target in an infrared television camera is gold-doped silicon (28).

Solar Rocket Spectroscopy

The astrophysicist is interested in devising a model of the solar atmosphere in order to account for the observations which astronomers have made. Another of his problems has to do with the interior of the sun; theories of the latter are tied in with the atmosphere of the sun in the sense that the atmosphere represents a kind of boundary condition for the interior, and that the nature of the exchange of energy between the interior and the atmosphere is a critical factor in reviewing both problems.

Until the time of rocket observations the sun's spectrum was limited to about 2800 Å on the short wave length side by oxygen and ozone absorption and to about 2.5 μ on the long wave length side by water vapor absorption. The ultraviolet region has been extended considerably since rocket instruments were first flown in 1946.

The ultraviolet spectrum of the sun may be divided into three regions: The normal extension of the visible continuum with its characteristic Fraunhofer lines to about 1500 Å, the line emission region which begins around 1900 Å and extends well into the extreme ultraviolet region at 84 Å, and finally the soft x-ray region from 100 to 1 Å or less. Sections of the solar spectrum photographed from rockets are shown in Fig. 7.

The use of the expression "x-ray emission" from the sun has often led to a misunderstanding; one cannot speak of radiation in a given wave length range as being x-ray radiation unless the origin of this radiation is typical of that for x-rays, namely inner shell transitions or electron decelerations. If the radiation originates as a result of optical transitions in a highly ionized atom, that is, as a result of outer electron jumps, then the radiation might be correctly referred to as extreme ultraviolet radiation, even though it may have identical wave length values with x-rays, and even

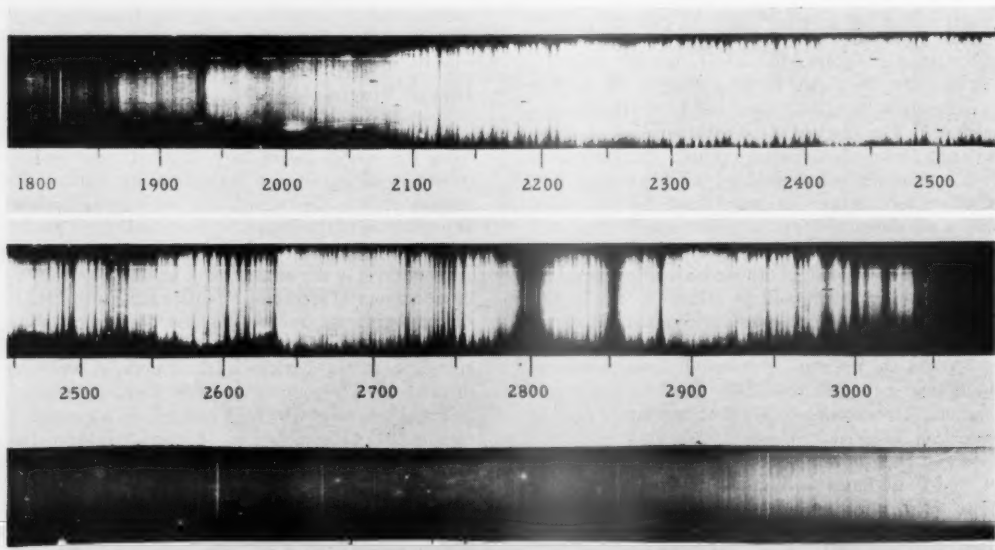


Fig. 7 Photos of the solar spectrum taken with rocket instruments designed at the Upper Air Laboratory, University of Colorado. The top two regions include the near ultraviolet. The emission cores of the MgII absorption lines near 2800 Å are easily seen. The third section covers the range from about 2000 to 1000 Å; its most prominent feature is the hydrogen Lyman-alpha line at 1216 Å on the left and numerous other emission lines

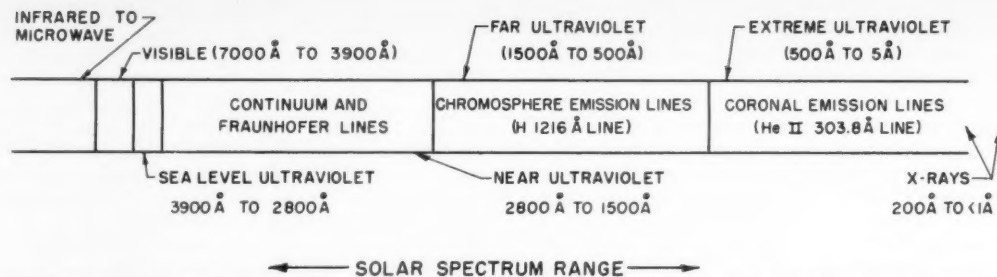


Fig. 8 A diagram of the solar spectrum with emphasis on the ultraviolet region. The divisions indicated are arbitrarily made for convenience. The scale is not linear

though no distinction exists between the two radiations, once created, insofar as their proton behavior is concerned. Fig. 8 is a diagrammatical representation of the solar spectrum with some of the more prominent ultraviolet regions indicated.

In the past 15 years, astrophysicists have changed some of their views regarding the origin of solar radiation in the various spectral regions. One may still speak of the photosphere, chromosphere and corona, but the detailed concepts have changed. The photosphere is the visible surface boundary of the sun and is actually several scores of miles deep. Its kinetic temperature is about 6000 K, and the radiation emitted corresponds roughly to black body radiation for this temperature, being of the nature of a continuum from the near infrared to the near ultraviolet. It has been fairly well established that most of the solar continuum is caused by transitions involving the ion H⁻. However, the part below 1800 Å may originate (29) as a consequence of the presence of appreciable amounts of molecular hydrogen just above the photosphere where temperatures drop to 4500 K. Collisions of hydrogen molecules with electrons can excite the former to levels where transitions to a virtual level involving dissociation is possible. The energies of these transitions are continuous, and a continuum results.

The photosphere is also the region of sunspots and the small granules, or pocklike structures. The latter have only recently been photographed (30), under high resolution, from a balloon. The granules are as small in some cases as 180 miles across. They might represent the appearance of vertical columns of gas flowing upward from beneath the photosphere at speeds of a mile or two per second, and persisting for only a few minutes.

The temperature of a shallow strip of the chromosphere immediately above the photosphere is less than the temperature of the latter by about 1500 K. Some of the lines in the Fraunhofer absorption spectrum are formed when light from the photosphere passes through this region (sometimes called the reversing layer). Higher in the chromosphere the temperature rises irregularly again to the order of 30,000 K before it blends into the corona or outer atmosphere of the sun. Many of the emission lines of the solar spectrum in the ultraviolet (Fig. 7) originate in the chromosphere.

Conditions are such that thermodynamic equilibrium cannot necessarily be assumed. The process of line emission is very complex; a knowledge of many parameters is necessary for the formulation of the problem. Ionized atoms are common, especially in the upper regions where temperatures are high. The problem is further complicated by the fact that in some areas, often of large extent, called active regions, the chromosphere is considerably disturbed. These areas (plages or flocculi) are frequently, though not always, associated with the sunspot groups, and they follow the sunspot cycle. Only when the sun is photographed in light of the wave length corresponding to a transition in a given atom are the plage areas distinctly visible. Photographs of

the sun's disk in the radiation of hydrogen Lyman-alpha (1216 Å) have been successfully obtained from rockets by the use of both lithium fluoride and grating optics (25, 26). In these photographs, the strong preference for 1216-Å emission in plage areas is revealed. Sometimes a very bright but relatively small chromospheric area called a flare develops near a sunspot region. The flare is especially bright in the light of the hydrogen Balmer-alpha line. It is invisible unless viewed in nearly monochromatic light. Flares may last from a few minutes to several hours. They are often accompanied by disturbances of various kinds in Earth's upper atmosphere. Photon counters have proved that there is considerable enhancement of solar x-ray radiation in a flare. Probably enhanced ultraviolet radiation occurs as well. Flares occur in the chromosphere of the sun; their nature is not yet well understood.

The solar continuum extends from the visible into the infrared. At sea level no observations have been made beyond about 2.5 μ because of strong absorption caused by water vapor in Earth's atmosphere beginning at this region (31). However, solar radiation is again found in the microwave region at wave lengths around 1 mm. It is interesting to note that the effective black body temperature of the infrared continuum of the sun reaches a minimum at about 2.5 μ; beyond this point the effective temperature rises.

Efforts to measure infrared radiation at higher altitudes from airplanes and balloons have been successful (32-34). In most cases the resolving power has been quite low, but results clearly show the diminishing effects of absorption by water vapor and carbon dioxide with increase in altitude. There is very little trace of water vapor above about 46,000 ft, but bands of carbon dioxide persist to much greater heights. In these instruments a grating is used to effect dispersion. Lead sulfide and lead telluride cells have been employed. No measurements have been made beyond about 8 μ to date. A large aperture high resolution infrared grating spectrometer is scheduled (by NRL and Nat. Bur. Standards) for a balloon flight in the near future for study of the solar infrared radiation between 18 and 38 μ.

In Fig. 9 is shown the infrared spectrum of the sun from the visible to beyond 13 μ (the deflection is not directly proportional to the energy). The large absorption due to water vapor, carbon dioxide, ozone and other constituents of Earth's atmosphere is clearly shown.

Origin of Coronal Lines

In the corona of the sun the atoms are highly ionized and are greatly outnumbered by the free electrons with which they make frequent collisions. The electron temperature is between 1 and 2 million deg. The radiation field in the corona is mainly determined by the relatively low energy photons from the cool photosphere and chromosphere below. Thermodynamic equilibrium does not prevail; i.e., collisional

processes and radiation processes do not balance within themselves. The equations which describe a given phenomenon in the corona are based on equilibrium of a statistical nature that is concerned with the balance of the various kinds of processes.

At any one time there is a certain number of atoms of a given species in a particular ionized state. Besides abundance, temperature is the main factor in determining this number. Computing $1/2kT$ for coronal temperatures, one concludes that there are few atomic ions with ionization potentials less than 200 ev. The coronal emission lines therefore probably are caused by ions that have ionization potentials greater than this value.

The mechanism for the emission of a given line in most cases is as follows (29). An atomic ion collides with an electron and is excited to a higher state. Since for ions the ground state is considerably below the first excited state, the chances are that the outer electron of the ion will be moved only to the first states; higher states are much less apt to be reached by the outer electron. The astrophysicist must compute a cross section for such a mechanism which he calls a collisional excitation cross section. This cross section will of course depend upon the energy of the colliding electron so that at this point a knowledge of the distribution of the electron velocities in the corona is important. When the electron reaches the first upper state it almost immediately returns to the ground state with the emission of a photon whose

frequency is given by the usual relationship $E = h\nu$, where E is the excitation energy for the state. If this transition of the electron to the lower state does not occur fast enough, the ion may suffer another collision before the electron has a chance to return, in which case the electron may be raised to still a higher state, or may return to the ground state without the emission of a photon, if the excess energy is carried off by the ion and the colliding particle (radiationless collision). However, when the probabilities of the several events are computed, the chances are overwhelmingly in favor of the electron's returning to the ground state before anything happens to the ion, so that the photon is emitted. Such photons produce the *resonance emission line* of the ion.

It may sometimes happen that the collision of an ion with another particle (electron) excites the outer electron of the ion to a so-called metastable level. Transitions of the electron to the ground level are said to be forbidden in such cases. Actually this means that the electron takes much more time than usual for returning to the ground level, so that an intervening collision similar to those described previously is more likely to occur. Even so, for the conditions which prevail in the corona, the transition from a metastable level is in most instances effected, giving rise to a photon corresponding to a so-called forbidden line in the spectrum. The coronal emission lines which have for some time been observed in the visible region of the spectrum are all forbidden lines in this sense, except that here the transitions are between upper levels lying close to each other, rather than between a higher state and the ground state.

This mechanism accounts nicely for most of the permitted and forbidden coronal emission lines. However, there is another way by which emission may be achieved that is very important in relation to certain ions (29). A case in point is the oxygen atom with five electrons removed, namely O VI. This ion has an ionization potential of 138 ev, hence should be almost completely ionized in the corona, so that very few of them would be available to cause emission. Nevertheless, when one examines the solar ultraviolet spectrum one finds that several lines due to O VI are present, and that these represent many more than just the resonance line (22). The explanation of these unexpected results centers around the high ionization potential of O VII (over 700 ev). Apparently most of the oxygen atoms in the corona should theoretically be in the ionized state O VII, because there is not enough energy in the free electrons to ionize them further; whereas, the ionization of O VI to O VII is so easily effected because of the relatively small energy required, that little oxygen should remain in ionized states lower than O VII. The O VI lines are emitted after an O VII ion captures a free electron (recombination) and when the electron cascades to the ground state. The O VI ion then makes a collision and loses an electron to become O VII again. Such a process can be theoretically analyzed only after recombination coefficients for the ion have been computed.

It can be shown that the coronal gases also emit a continuum in the soft x-ray region, although most of the emission occurs in the coronal lines. The continuum is expected to be that of a gray body at a temperature of between 1 and 2 million deg.

An Imaginary Space Solar Observatory

We will here describe the instrumentation which might be present in a stabilized space solar observatory equipped with suitable power and pointing devices, and with telemetering and television transmission equipment. The basic principles involved for each instrument have been discussed elsewhere in this paper.

Instrument No. 1 is a photon counter with windows so chosen that x-rays of wave lengths less than 20\AA are measured. The gas is neon with some ethyl formate, and the window and aluminum are of such thickness as to give good

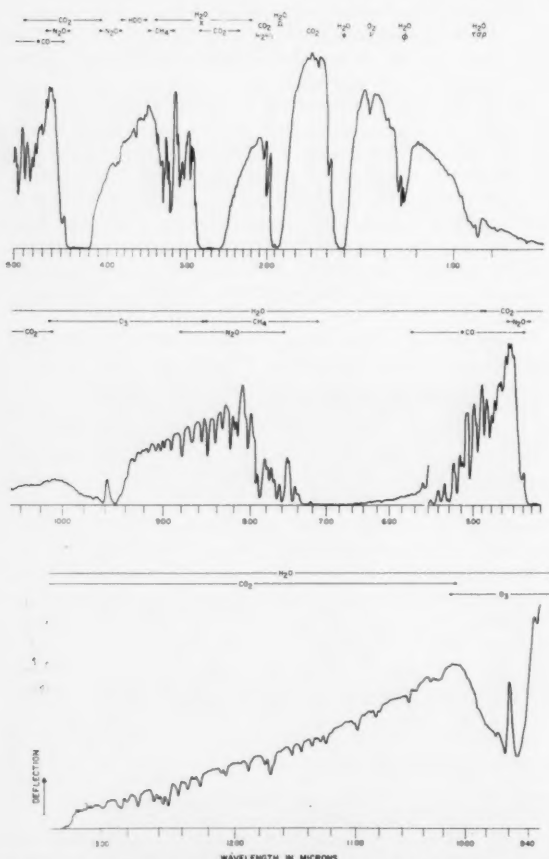


Fig. 9 The infrared spectrum of the sun from the visible to beyond 13μ . The diagram was constructed by Gates of the National Bureau of Standards. The deflection is not proportional to the intensity, and the scale changes at various places. The strong telluric absorption due to bands of H_2O , CO_2 and O_3 is evident

transmission in the 10-Å region (21). The upper wave length cutoff is at 25 Å. In this x-ray region solar radiation is usually small, variable or absent. However, at times of solar flares the intensity increases remarkably. This latter effect is what is expected to be observed by this space observatory instrument.

Instrument No. 2 is a grazing incidence spectrograph designed to cover the region of the solar spectrum between 20 and 900 Å. It is similar to the one of Fig. 3 except that in front of the slit a prefocusing grating is used at grazing incidence for selecting a wave length range to fall on the slit in order to reduce scattered visible light along the Rowland circle and to separate orders (35). The detector is not a film but a photomultiplier tube with its glass window coated with the phosphor ZnO:Zn which has a relatively high quantum efficiency for exciting the radiation in the far ultraviolet (36). The tube automatically sweeps the Rowland circle. Transmitted signals give the position of the tube (wave length) and the response when solar radiation of sufficient intensity is present. The prefocusing grating must be rotated and translated as the detector tube moves in order to focus the appropriate wave length region on the slit of the spectrograph. In this way the spectrum may be observed between 20 and 900 Å. Of interest would be changes in intensity of solar ultraviolet lines as a function of time and the correlation of this fact with solar activity. The measurement of the absolute intensity of solar ultraviolet radiation as a function of wave length is no less an important problem. Were the photomultiplier in the spectrograph calibrated, the latter measurement would also be possible (37).

Instrument No. 3 would be a spectrograph of the normal-incidence type with optics coated with magnesium fluoride on aluminum to insure high reflectivity in the ultraviolet. The spectral region of interest would be the hydrogen Lyman series and the continuum beyond the series limit. One can use a photoelectric-type detector, set behind a movable slit which sweeps along the Rowland circle. The device makes use of the internal photoelectric effect (38, 39) of tungsten, which serves as the cathode. There is negligible response to light of wave lengths longer than about 1300 Å so that scattered visible light in the instrument is no problem. The photoelectrons are directed by a magnetic field into a Bendix manufactured secondary emission photomultiplier, whose output is ultimately telemetered to Earth. Because hydrogen is by far the most abundant element in the solar atmosphere, and because its behavior there has been the subject of many an astrophysical theory, the data obtained by the instrument would be of great significance. For the lines and the continuum absolute intensities, relative intensities and variation of intensity with time are examples of important data that may readily be obtained.

Instrument No. 4 is a high resolution echelle spectrograph similar to the one shown in Fig. 6. Because angles of incidence are small, special optical coatings such as zinc sulfide or magnesium fluoride to increase reflectivity are needed. The observations to be made are the measurement of the intensity of hydrogen Lyman-alpha line at 1216 Å and of its profile under high resolution. The first grating forms a stigmatic image of the sun in 1216-Å radiation on the slit. The final high resolution line image, much dispersed, is formed near the entrance slit where it is scanned by a narrow slit located in front of a photomultiplier coated with a suitable phosphor such as sodium salicylate. The output of the tube is amplified and telemetered back to Earth along with the signals locating the sweep-slit so as to fix the wave length of the part of the line profile being examined. In this way the line profile, wave length vs. relative intensity, may be reconstructed. With care in calibration even absolute intensity can be measured. The results are significant in astrophysical problems. Continuous observations of the absorption center of the hydrogen Lyman-alpha line, Fig. 4, can yield, provided resolution is high enough, critical data on the physical condi-

tions which prevail in the chromosphere, or on the nature of hydrogen gas clouds in space between Earth and the sun. If the focusing grating were repeatedly made to move slightly so as to scan the sun by relocating the image on the entrance slit, the variation of the profile and intensity of the line over the disk of the sun may be studied.

Instrument No. 5 consists of two parts, one a camera for imaging the sun in the visible, the other a camera for imaging the sun in the radiation of the hydrogen Lyman-alpha line (1216 Å). In the first case, direct television techniques may be employed for sending the image to Earth; in the second, an image amplifier similar to one described previously must be used before transmission to Earth. The optical design of the 1216-Å monochromatic camera has already been discussed. It is one utilizing but two gratings. These cameras will enable an Earth observer to follow important changes of solar activity (such as development of flares or large spot regions) and, provided electronic communication between Earth and observatory is possible, to monitor instruments Nos. 2, 3 and 4 so that radiation from pertinent areas of the sun's disk enters the instruments. In any event these pictures may be useful in identifying the parts of the sun's disk being scanned by each of the instruments and in indicating which regions are active.

Instrument No. 6 is an infrared camera. A high speed, grating-type infrared monochromatic camera, similar to the ultraviolet one of instrument No. 5, forms an image of the sun in infrared radiation from the center of an absorption region of one of the bands of a solar compound. The image falls on a gold-doped silicon target and is televised to Earth. The picture will give information about the distribution of the molecular compound over the solar disk, and about the temperature of various regions of the solar atmosphere where the molecule can exist.

References

- 1 Spitzer, L., "Space Telescopes and Components," Astronomical Society Meeting, Cleveland, Dec. 1959.
- 2 Nidey, R. A., "Aspect Sensing, Astrostat Design and Orientation Control in Space Research," ARS preprint no. 1016-59, Nov. 1959.
- 3 Chubb, T. A. and Friedman, H., "Photo Counters for the Far Ultraviolet," *Rev. Sci. Inst.*, vol. 26, No. 5, 1955, pp. 493-498.
- 4 Miller, S. C., Mercurio, R. and Rense, W. A., "Lyman-Alpha Intensity and Solar Limb Darkening from Rocket Spectrograms," *Astrophys. J.*, vol. 124, no. 3, 1956, pp. 580-585.
- 5 Johnson, F. S., Malitson, H. H., Purcell, J. D. and Tousey, R., "Emission Lines in the Extreme Ultraviolet Spectrum of the Sun," *Astrophys. J.*, vol. 127, no. 1, 1958, pp. 80-92.
- 6 Cox, J. T., Waylonis, J. E. and Hunter, W. R., "Optical Properties of Zinc Sulfide in the Vacuum Ultraviolet," *J. Opt. Soc. Amer.*, vol. 49, no. 8, 1959, pp. 807-810.
- 7 Walker, W. C., Rustgi, O. P. and Weissler, G. L., "Optical and Photoelectric Properties of Thin Metallic Films in the Vacuum Ultraviolet," *J. Opt. Soc. Amer.*, No. 49, no. 5, 1959, pp. 471-475.
- 8 Hass, G. and Tousey, R., "Reflection Coatings for the Extreme Ultraviolet," *J. Opt. Soc. Amer.*, vol. 49, no. 6, 1959, pp. 593-602.
- 9 Rense, W. A. and Violett, T., "Method of Increasing the Speed of a Grazing-Incidence Spectrograph," *J. Opt. Soc. Amer.*, vol. 49, no. 2, 1959, pp. 139-141.
- 10 Tousey, R. and Purcell, J. D., "The Profile of Solar Hydrogen Lyman-Alpha," Research to be published.
- 11 Tousey, R. and Purcell, J. D., "Solar Ultraviolet Spectroscopy from Rockets," Optical Society of America Meeting, Ottawa, Canada, Oct. 1959.
- 12 Greig, J. J. and Ferguson, W. F. C., "New Mounting for an Echelle Diffraction Grating," *J. Opt. Soc. Amer.*, vol. 40, no. 8, 1950, pp. 504-506.
- 13 Aytion, M. W., Derby, T. J., Boteler, V. H. and Brown, C. R., "Infrared," a Library of Congress bibliography.
- 14 Stuart, F. E., "A Miniature Transistorized Radiometer for Measurement of Visible and Infrared Radiation from High Altitude Vehicles," Scientific Report no. 1, contract no. AF 19(604)-1899, 1958.
- 15 Smith, R. A., Jones, F. E. and Chasmar, R. P., "The Detection and Measurement of Infrared Radiation," Oxford Press, 1957.
- 16 Wormser, E. M., "Properties of Thermistor Infrared Detectors," *J. Opt. Soc. Amer.*, vol. 43, no. 1, 1953, pp. 15-21.
- 17 Greenler, R. G., "Interference Filters for Infrared," *J. Opt. Soc. Amer.*, vol. 47, no. 2, 1957, pp. 130-131.
- 18 Heavens, O. S., Ring, J. and Smith, S. D., "Infrared Filters," *Spectrochimica Acta*, vol. 10, 1957, p. 179.
- 19 Smiley, V. N., "Multilayer Interference Filter for the Infrared," doctorate dissertation, Univ. of Colorado, 1959.
- 20 Smith, S. D., "Design of Multilayer Filters by Considering Two Effective Interfaces," *J. Opt. Soc. Amer.*, vol. 48, no. 1, 1958, pp. 43-46.
- 21 Byram, E. R., Chubb, T. A. and Friedman, H., "The Solar X-Ray

- Spectrum and the Density of the Upper Atmosphere." *J. Geophys. Res.*, vol. 61, no. 2, 1956, pp. 251-263.
- 22 Violett, T. and Rense, W. A., "Solar Emission Lines in the Extreme Ultraviolet," *Astrophys. J.*, vol. 130, no. 3, 1959, pp. 954-960.
- 23 Miller, S. C. and Rense, W. A., "A Monochromatic Camera for Photographing the Sun's Disk in Hydrogen Lyman-Alpha," Colorado-Wyoming Academy of Science Pub., 1955.
- 24 Behring, W. E., Jackson, J. M., Miller, S. C. and Rense, W. A., "Monochromatic Camera for Photography in the Far Ultraviolet," *J. Opt. Soc. Amer.*, vol. 44, no. 3, 1954, pp. 229-231.
- 25 Mercure, R., Miller, S. C., Rense, W. A. and Stuart, F., "The Sun's Disk in Lyman-Alpha Radiation," *J. Geophys. Res.*, vol. 61, 1956, pp. 571-573.
- 26 Purcell, J. D., Packer, D. M. and Tousey, R., "Lyman-Alpha Photographs of the Sun," *Nature*, London, vol. 184, 1959, pp. 8-10.
- 27 Tuve, M. A., Ford, W. K., Hall, J. S. and Baum, W. A., "Results of Preliminary Tests of Cascaded Image Converters," *Pub. of Ast. Soc. of the Pac.* vol. 70, 1958, pp. 592-594.
- 28 Redington, R. W. and van Heerden, P. I., "Doped Silicon and Germanium Photoconductors as Targets for Infrared Television Camera Tubes," *J. Opt. Soc. Amer.*, vol. 49, no. 10, 1959, pp. 997-1001.
- 29 Varsavsky, C., "Some Atomic Parameters for Ultraviolet Lines." Research to be published.
- 30 Schwarzschild, M., "Photographs of the Solar Granulation taken from the Stratosphere," *Astrophys. J.*, vol. 130, no. 2, 1959, pp. 345-363.
- 31 Mohler, O. C., Pierce, A. K., McMath, R. R. and Goldberg, L., "Photometric Atlas of the Near Infrared Solar Spectrum, 8465 to 25,242 Å," Univ. of Michigan Press, 1950.
- 32 Murcray, D. G., Brooks, J., Murcray, F. and Shaw, C. C., "High Altitude Infrared Studies of the Atmosphere," *J. Geophys. Res.*, vol. 63, no. 2, 1958, pp. 289-299.
- 33 Gates, D. M., Murcray, D. G., Shaw, C. C. and Herbold, R. J., "Near Infrared Solar Radiation Measurements by Balloon to an Altitude of 100,000 Feet," *J. Opt. Soc. Amer.*, vol. 48, no. 12, 1958, 1010-1016.
- 34 Houghton, J. R., Moss, T. S. and Chamberlain, J. P., "An Airborne Infrared Solar Spectrometer," *J. Sci. Instrum.* vol. 35, 1958, pp. 329-333.
- 35 Douglas, A. E. and Herzberg, G., "Separation of Overlapping Orders of a Concave Grating Spectrograph in the Vacuum Ultraviolet Region," *J. Opt. Soc. Amer.*, vol. 47, no. 7, 1957, pp. 669-672.
- 36 Conklin, R. L., "Behavior of Several Phosphors upon Irradiation in the Vacuum Ultraviolet," *J. Opt. Soc. Amer.*, vol. 49, no. 7, 1959, pp. 669-672.
- 37 Aboud, A., Behring, W. E. and Rense, W. A., "Emission-Line Intensities in the Solar Ultraviolet," *Ap. J.*, vol. 130, no. 2, 1959, pp. 381-383.
- 38 Hinteregger, H. E., "Photoelectric Emission in the Extreme Ultraviolet," *Phys. Rev.* vol. 96, no. 2, 1954, p. 538.
- 39 Hinteregger, H. E., "Telemetering Spectrophotometer of Solar Extreme Ultraviolet and Soft-X-rays." Research to be published.

Experiments on the Departure From Chemical Equilibrium in a Supersonic Flow¹

PETER P. WEGENER²

Jet Propulsion Laboratory,
California Institute of Technology
Pasadena, Calif.

Stationary supersonic nozzle flow of a reacting gas mixture, in thermodynamic equilibrium or in states between equilibrium and frozen flow, was investigated experimentally and analytically. With this fully determined flow system, it was possible to check various criteria to predict departures from equilibrium. A method proposed by Bray for Lighthill's ideal dissociating gas was extended to our real gas system, and the results showed agreement with the experiments.

HIGH speed flows with large changes of temperature provide interesting problems in thermodynamics, since the usual notion of treating the medium as a thermally and calorically perfect gas becomes invalid. However, so long as it is permissible to assume that thermodynamic equilibrium prevails everywhere, certain flow fields are amenable to calculation. The problem becomes more difficult if it is found that departures from thermodynamic equilibrium occur in the flow, and rate processes must also be taken into account to compute parameters of practical interest, such as the heat transfer to a blunt body in hypersonic flow, the temperature

of a flame front, the thrust of a rocket nozzle or the electromagnetic properties of a shock wave region. Such calculations depend on the knowledge of the relaxation times of all transformation processes involved, and they are usually difficult or impossible to perform. It is at this point that one wishes to resort to a "criterion" with which to predict departures from equilibrium in a given flow situation. Such a criterion may require an estimate of the dynamics of the process and some understanding of its mechanism, in addition to an estimate of the flow parameters of the limiting conditions for frozen or equilibrium flows. Also, numerical answers should be rapidly available. The latter requirement is important, since, with the information outlined above, the equations of motion would, in principle, be approximately solved, and we expect the application of equilibrium criteria to effect a simpler computation. Finally, the simplification of involved rate processes inherent in a workable criterion may lead to a deeper physical understanding of flow situations.

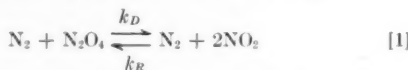
Presented at the ARS Semi-Annual Meeting, June 8-12, 1959, San Diego, Calif.

¹ This paper presents the results of one phase of research carried out at the Jet Propulsion Laboratory, CIT, under joint sponsorship of the Dept. of the Army, Ordnance Corps, under Contract no. DA-04-495-Ord 18, and the Dept. of the Air Force.

² Chief, Gas Dynamics Research Section.

We wish to discuss the rapid expansion of a gas or gas mixture from a reservoir with the medium undergoing simultaneous dissociation and recombination reactions. It will be assumed that the flow is in thermodynamic equilibrium in the reservoir, and that, furthermore, all external and internal degrees of freedom of the participating species remain in equilibrium during the expansion. Practical applications of this process are the flow in a rocket nozzle, the flow around a blunt body moving at hypersonic speeds, and the expansion of a gas mixture in a hypersonic wind tunnel from a reservoir of high stagnation enthalpy such as that found in plasma jets or are heated hypersonic wind tunnels.

Many of the chemically important features of such flows may be modeled by studying experimentally and analytically the stationary flow of a reacting gas mixture of nitrogen dioxide NO_2 and tetroxide N_2O_4 carried at low concentration in inert nitrogen N_2 . This reaction may be written



where k_D and k_R are the rate constants for dissociation and recombination, respectively. With a suitable experimental environment it is possible to produce expansions of this mixture through a supersonic nozzle, anywhere from near frozen flows to flows in chemical equilibrium. Such a system, including the dynamics of the reactions, is fully determined, permitting the use of this flow as a testing ground for the validity of some of the criteria for thermodynamic equilibrium found in the literature. The procedure will be to compute the terms in the criteria without resorting to approximations and to compare the predictions with the experimental observations.

These are the criteria for near equilibrium (or near frozen) flow initially proposed by Penner and co-workers (1,2,3)³ in conjunction with performance calculations for rocket nozzles.⁴ The near equilibrium criterion embodies the calculation of a small temperature difference representative of a small difference between the actual concentration of the reactants and that concentration predicted for chemical equilibrium. The method was used by Logan (4) who applied it to hypersonic flow around blunt bodies and in a nozzle. A different approach to the prediction of departures from chemical equilibrium is based on a comparison of the numerical value of the rate of change of degree of dissociation with distance in a nozzle with the magnitude of the dissociation rate term in the equation for the reaction mechanism, with both terms evaluated for chemical equilibrium. This method was proposed by Bray (5,6) who applied Lighthill's theory of the "ideal dissociating" gas (7), with Freeman's extension to nonequilibrium conditions (8), to the flow in a hypersonic nozzle. Bray's suggestion can easily be extended to real gases, and it will be shown that this method provides remarkable insight into the flow in expansions.⁵

Analytical Methods and Experiments

Equations of Motion for Frozen and Equilibrium Flow

The equations of motion for the stationary, one-dimensional flow of the mixture of Equation [1], neglecting friction, heat conduction and diffusion, have been derived elsewhere (10). The equations will be merely listed here. We define the degree of dissociation of the reactants by

$$\alpha = \omega_{\text{NO}_2}/(\omega_{\text{NO}_2} + \omega_{\text{N}_2\text{O}_4}) \quad [2]$$

where the mass flow fraction of the i th species is given by $\omega_i =$

³ Numbers in parentheses indicate References at end of paper.

⁴ The references given are those most readily available rather than those that trace the historical development.

⁵ Another scheme proposed, but not tested with our system, was recently given by Rudin (9).

m_i/m , and symbols without subscripts refer to the gas mixture. Throughout this work we will discuss only flows where dissociation in the nozzle supply (subscript 0) is complete and $(\omega_{\text{N}_2\text{O}_4})_0 = 0$. From Equation [2]

$$\alpha = \frac{\omega_{\text{NO}_2}}{(\omega_{\text{NO}_2})_0} = \frac{(\text{NO}_2)}{(\text{NO}_2)_F} \quad [3]$$

where

$(\) = \text{concentration (mole/cm}^3)$

$F = \text{frozen flow without composition change}$

We now write the continuity and momentum equations in the customary forms

$$A\rho u = m \quad [4]$$

$$-\rho u du = dp \quad [5]$$

where

$u = \text{velocity}$

$\rho = \text{density}$

$p = \text{pressure}$

$A = \text{cross-sectional area of the nozzle}$

With $\alpha_0 = 1$, the integrated energy equation is given by

$$\omega_{\text{N}_2} h_{\text{N}_2} + (\omega_{\text{NO}_2})_0 h_{\text{NO}_2} - \omega_{\text{N}_2\text{O}_4} \Delta h_{\text{N}_2\text{O}_4} + \frac{u^2}{2} = (\omega_{\text{N}_2} h_{\text{N}_2})_0 + (\omega_{\text{NO}_2} h_{\text{NO}_2})_0 \quad [6]$$

where

$h_i = \text{enthalpy per unit mass of the } i\text{th species}$

$\Delta h_{\text{N}_2\text{O}_4} = \text{the heat of dissociation of } \text{N}_2\text{O}_4 \text{ per unit mass of } \text{N}_2\text{O}_4$

Generally, h_{NO_2} is greater than $h_{\text{N}_2\text{O}_4}$; and we deal with an exothermic reaction if NO_2 recombines to N_2O_4 during the nozzle expansion. Finally, if we assume all participating species to be thermally (not calorically) perfect gases, the equation of state assumes the form

$$p = \rho TR \left[\frac{1 - (\omega_{\text{NO}_2})_0}{\mu_{\text{N}_2}} + \frac{(\omega_{\text{NO}_2})_0 - \omega_{\text{N}_2\text{O}_4}}{\mu_{\text{NO}_2}} + \frac{\omega_{\text{N}_2\text{O}_4}}{\mu_{\text{N}_2\text{O}_4}} \right] \quad [7]$$

where

$T = \text{temperature}$

$R = \text{the universal gas constant}$

$\mu_i = \text{molecular weight of the } i\text{th species}$

For given $A(x)$ we may now compute from Equations [4-7] all flow parameters for the frozen flow for which $(\omega_{\text{N}_2\text{O}_4})_0 = \omega_{\text{N}_2\text{O}_4} = 0$ in Equations [6 and 7]. The needed thermodynamic properties of the reactants are well known from the sources critically reviewed by Gray and Yoffe (11).

The opposite limiting expansion process of flow in chemical equilibrium exhibits the greatest possible change of composition during the expansion. Its properties for known $A(x)$ may be computed by adding to Equations [4-7] the law of mass action

$$K_p = 2 \frac{\mu}{\mu_{\text{NO}_2}} p \left[\frac{(\omega_{\text{NO}_2})_0^2}{\omega_{\text{N}_2\text{O}_4}} - 2(\omega_{\text{NO}_2})_0 + \omega_{\text{N}_2\text{O}_4} \right]_e \quad [8]$$

where

$K_p = \text{equilibrium constant in units of pressure}$

$\mu = \text{the molecular weight of the mixture}$

$e = \text{chemical equilibrium}$

In all succeeding examples, values for the two limiting flows will be shown with concentrations computed from $(i) = \omega_i p / \mu_i$.

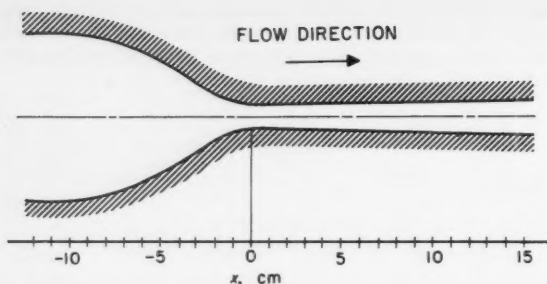


Fig. 1 Nozzle contour for exit Mach number of 1.8 in nitrogen

Calculation of Relaxation Time

Frozen and equilibrium flow may also be viewed kinetically as exhibiting zero or infinite reaction rates, respectively. In addition to the equilibrium thermodynamic properties of the species of the gas mixture of Equation [1], the rate constants are known (10,12,13); the reaction mechanism of Equation [1] may be expressed by

$$\left[\frac{\partial(\text{NO}_2)}{\partial t} \right]_T = 2k_D(\text{N}_2\text{O}_4)(\text{N}_2) - 2k_R(\text{NO}_2)^2(\text{N}_2) \quad [9]$$

Equation [9] describes a second-order dissociation reaction opposed by a third-order recombination process. In the small temperature interval of interest, the recombination rate constant is independent of temperature whereas the dissociation rate constant follows an Arrhenius temperature dependence given by $k_D \sim \exp(-B/T)$. It can be shown (10) by integration of Equation [9] that the reaction time τ elapsing for a change of reactant concentration from $(\text{NO}_2)_1$ to $(\text{NO}_2)_2$ at constant temperature is given by

$$\tau = \frac{1}{2(\text{N}_2)k_R C} \times \ln \frac{[-(K_c/2) - 2(\text{NO}_2) - C] [-(K_c/2) - 2(\text{NO}_2)_1 + C]}{[-(K_c/2) - 2(\text{NO}_2) + C] [-(K_c/2) - 2(\text{NO}_2)_1 - C]} \quad [10]$$

where

$$C = [(K_c^2/4) + 4K_c(\text{N}_2\text{O}_4)_1 + 2K_c(\text{NO}_2)_1]^{1/2} \quad [11]$$

and K_c is the equilibrium constant in units of concentration given by $K_c = k_D/k_R = K_p/RT$. As long as the NO_2 concentration at the end of a chosen time interval is not too close to that prevailing in chemical equilibrium, either of the terms on the right-hand side of Equation [9] may be neglected, depending on whether dissociation or recombination predominates. In the latter case Equation [9] becomes

$$(\partial\text{NO}_2/\partial t)_T = -2k_R(\text{NO}_2)^2(\text{N}_2) = k'(\text{NO}_2)^2 \quad [12]$$

with k' constant at constant temperature. The integration of Equation [12] leads to

$$\tau = \frac{1}{2(\text{N}_2)(\text{NO}_2)_1 k_R} \left[\frac{(\text{NO}_2)_1}{(\text{NO}_2)} - 1 \right] \quad [13]$$

which is a simpler formula for computing the reaction time.

Apparatus

The experimental equipment described elsewhere (10) consists primarily of a continuously operating supersonic wind tunnel of $2 \times 3.2\text{-cm}$ exit cross section. The reactants are fed at a known rate into a dry nitrogen flow with supply pressure p_0 of about 2 atm and supply temperature T_0 of about 400 K. The reactant concentration Φ in mole per cent in the supply is defined by

$$\Phi = 100(\text{NO}_2)_0 RT_0 / p_0 \quad [14]$$

with values up to 5 per cent employed practically. For these typical supply conditions, α_0 is equal to 1 as postulated in the previous analysis. The expansion takes place through a converging-diverging, water-cooled nozzle designed to give continuously varying flow parameters. The nozzle outline is shown to scale in Fig. 1 with the sonic throat located at $x = 0$ in reference to the succeeding figures. The flow in this nozzle is one-dimensional (14), and the function $A(x)$ entering the equations of motion is empirically determined from a nitrogen calibration giving the effective cross-sectional area. The Mach number at the nozzle exit is about 1.8 with the NO_2 largely recombined to N_2O_4 for chemical equilibrium. The local NO_2 concentration can be determined directly from an absorption measurement with light of about 4300 Å (10,14), since N_2O_4 and N_2 are transparent. The N_2O_4 concentration finally may be found from

$$(\text{N}_2\text{O}_4) = (1/2)[(\text{NO}_2)_F - (\text{NO}_2)] \quad [15]$$

At the higher initial reactant concentrations, static pressure measurements in the flow in conjunction with the known area and Equations [4-7] permit the determination of all other flow parameters (10). The conditions of selected experiments, identified alphabetically, are given in Table 1. Two contrasting examples are shown in Figs. 2 and 3, where the experimentally found dimensionless NO_2 concentration in the nozzle is plotted with the curves predicted from the previous analysis for frozen and equilibrium flow. In Fig. 2 it is seen that the flow of experiment C follows the curve for equilibrium up to $x \sim 3$ cm, beyond which the observed flow departs markedly from chemical equilibrium and exhibits reactant concentrations at the nozzle exit about halfway between the two limits. (These stations of departure from equilibrium are also noted in Table 1.) In contrast to this behavior, experiment F on Fig. 3 is a flow which is in chemical equilibrium throughout. Departure from chemical equilibrium is more clearly seen if degree of dissociation is plotted rather than concentration, as shown again for experiment C in Fig. 4.

Table 1 List of experimental conditions

Experiment	Φ , per cent	p_0 , atm	T_0 , K	Departure from chemical equilibrium x , cm	Number of experiments	A (see Eq. [27])	Remarks
A	0.50	2.00	400	4.5-5	5	1	least reliable owing to low Φ
B	0.65	1.98	371	2-2.5	1	1.25	note the low T_0
C	1.00	2.00	400	~3	2	0.42	
D	2.50	2.16	402	7-8	1	0.48	
E	4.54	2.21	408	>15	1	...	chemical
F	5.00	2.16	402	>15	1	...	equilibrium throughout

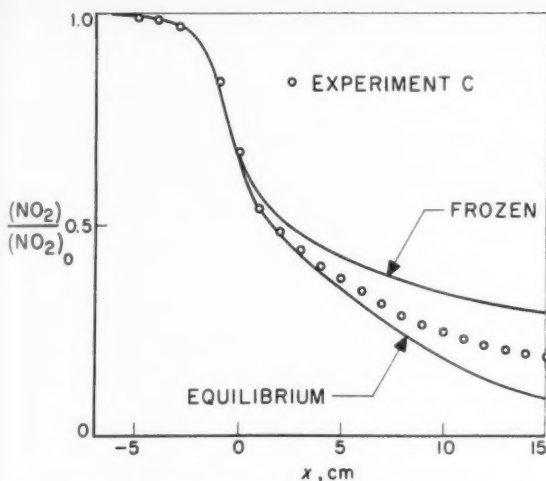


Fig. 2 Dimensionless NO_2 concentration in the nozzle with the flow observed to depart from chemical equilibrium

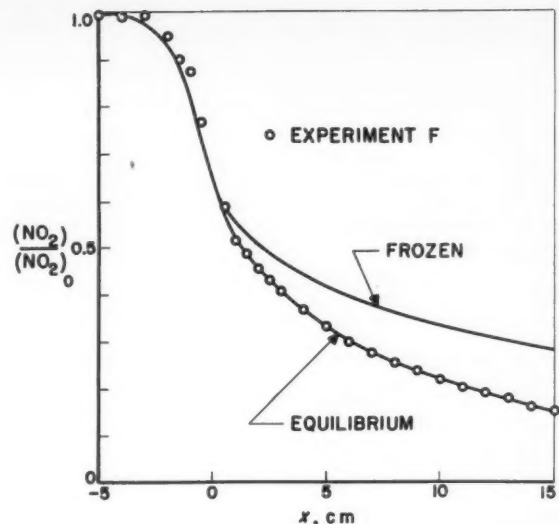


Fig. 3 Dimensionless NO_2 concentration in the nozzle with the flow in chemical equilibrium

Prediction of Departure From Chemical Equilibrium

Temperature Lag or Characteristic Time Criterion

Penner and co-workers (1,2) considered a residence time of the chemical species in a given temperature interval in the expanding flow of a rocket nozzle. Comparing composition computed for the end state of this residence time with that predicted for chemical equilibrium, it is then possible to determine if equilibrium was maintained or not. In principle this method may be applied to the entire expansion in one step, or one may subdivide the flow at will (1,4). The treatment may be applied to a reaction of the type of Equation [1], which is formally similar to the reassociation of atoms in the presence of an inert third molecule, and Altman and Carter's discussions of the method (3) as extended to our own reaction will be followed. We obtain for chemical equilibrium, from Equation [9], by setting the left-hand side equal to zero

$$K_c = \frac{k_D (\text{NO}_2)_e^2}{k_R (\text{N}_2\text{O}_4)_e} \quad [16]$$

Equilibrium in a flow will be maintained as long as the reactant concentration follows

$$\frac{d \ln K_c}{dt} = \frac{d \ln(\text{NO}_2)_e^2}{dt} - \frac{d \ln(\text{N}_2\text{O}_4)_e}{dt} \quad [17]$$

where the quantities $d \ln ()/dt$ refer to the total change of concentration of the reacting species with time. In a nozzle expansion the concentration change results from two separate processes: The flow itself and the chemical reaction. Each term on the right-hand side of Equation [17] may then be split according to these two processes, and the total rate of change of concentrations may be expressed directly. In this expression one can replace the concentration ratio at equilibrium of Equation [16], corresponding to $K_c(T)$, by an assumed equilibrium constant $K_c'(T')$. In chemical equilibrium $T' = T$, whereas for flows whose composition is near equilibrium $|T' - T|$, called the temperature lag, is a small positive number for expansions. Near equilibrium K_c' is about equal to K_c ; and expanding the equilibrium constant in a Taylor series about T , retaining the first two terms and

making a number of substitutions and approximations from thermodynamic relations, the temperature lag for our reaction may finally be estimated (3) by

$$(T' - T) = \frac{(1 - C_e T / \Delta h_{\text{N}_2\text{O}_4}) (-dT/dt)}{k_R(\text{N}_2) [2(\text{NO}_2) + K_c']} = \tau \left(-\frac{dT}{dT} \right) \quad [18]$$

If the temperature lag computed for a given expansion is small, equilibrium is expected. If $(T' - T)$ is large, the flow has departed from equilibrium; however, since Equation [18] is valid only near equilibrium, no quantitative statement on the extent of the departure may be made. The expression given by τ has the dimension of time, and $(-dT/dt)$, the inverse residence time per unit temperature interval, may also be viewed as the cooling rate in the nozzle. This cooling rate

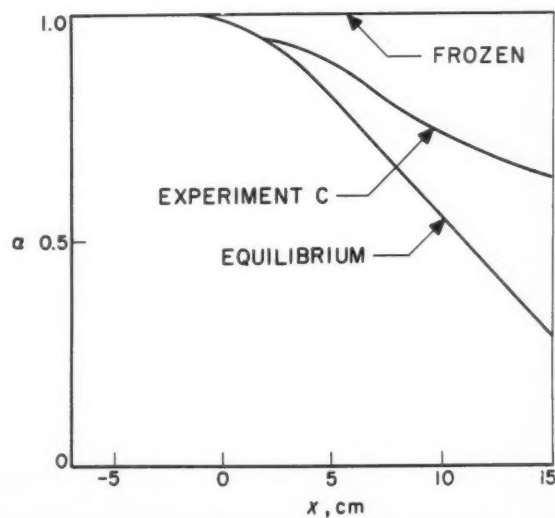


Fig. 4 Degree of dissociation in the nozzle with the flow observed to depart from chemical equilibrium

in our experiments varies from 10^5 to 10^6 K per sec; in smaller rocket nozzles it may go above 10^7 K per sec. It is even higher in hypersonic nozzles, and in each instance the maximum value occurs near the sonic throat.

The criterion of Equation [18] may be viewed as the product of a reciprocal characteristic flow time and a maximum reaction time τ_{\max} . Logan (4), following a further suggestion by Penner (2), assumes the flow to be in equilibrium as long as the temperature lag is much smaller than the local temperature. Equation [18] may, then, be written as a condition for equilibrium

$$\frac{T' - T}{T} = \frac{1}{T} \left| \frac{dT}{dt} \right| \tau_{\max} \leq 10^{-3} \quad [19]$$

where the choice of the value 10^{-3} is admittedly arbitrary.

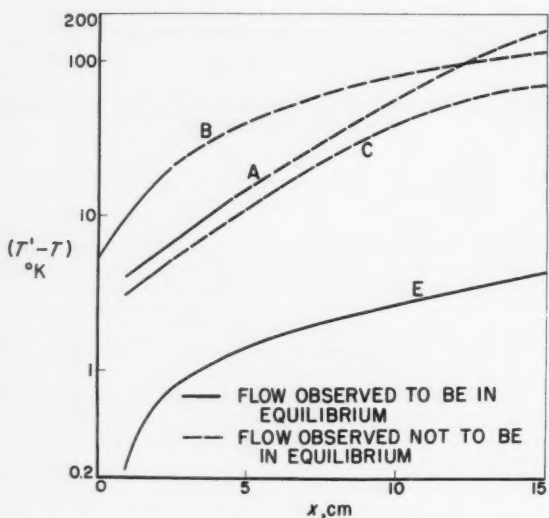


Fig. 5 Temperature lag criterion computed for several experiments

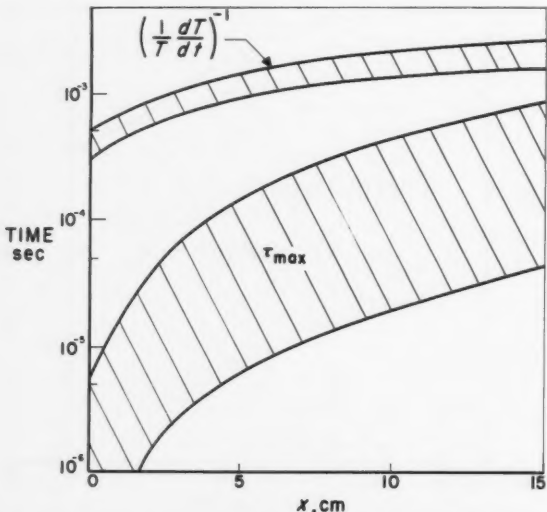


Fig. 6 Characteristic flow time and relaxation time in the range of all experiments

For τ_{\max} Logan computes a relaxation time; the reaction time implied in Equation [18] or that given by Equations [10] or [13] may be used. The initial reactant concentration in all instances ought to be chosen consistently to maximize the reaction time.

In our examples, we find at each nozzle station $(NO_2)_F \geq (NO_2) \geq (NO_2)_e$. At a given position, therefore, we decide to calculate the maximum possible reaction time from Equation [10], choosing $(NO_2)_1 = (NO_2)_F$. Using the integral of the complete equation, we must determine a final reactant concentration $(NO_2) = (NO_2)_F > (NO_2)_e$, to be reached at constant temperature, by

$$(NO_2)_r = (NO_2)_e + (1/e)[(NO_2)_F - (NO_2)_e] \quad [20]$$

in keeping with the usual definition of relaxation times. In other words, we define the maximum reaction time in the nozzle as the time it would take the reaction at $T = \text{constant}$ to proceed from $(NO_2)_F$, the maximum possible reactant concentration, to $(NO_2)_r$ defined by Equation [20]. The actual choice of τ_{\max} does not appear to affect the criterion of Equation [19] significantly; the choice may merely shift the arbitrary value of 10^{-3} as a limit for equilibrium.⁶

The temperature lag computed in this manner from Equations [19, 10, 11 and 20] is shown in Fig. 5. The departure from equilibrium (Table 1) is indicated by the change from solid to broken curves. This break is not seen at a consistent $(T' - T)$ value. Fig. 6 shows the ranges of the characteristic flow times and the maximum reaction times for all experiments with the minimum values occurring near the throat. Finally, in Fig. 7 we see values for the criterion Equation [19] plotted directly. The departures from equilibrium indicated are all appreciably above the value 10^{-3} ; however they are, in addition, not consistent with any particular value. It is believed that another interpretation of initial reactant concentration in Equation [18], or any other consistent choice of τ_{\max} , would only lead to a shift of the

⁶ This point is borne out by a numerical example for experiment B at $x = 5$ cm. The following are the values of the concentrations in units of 10^{-7} mole/cm³: $(NO_2)_F = 1.78$, $(NO_2)_e$ experiment = 1.38, $(NO_2) = 1.32$, and $(NO_2)_r = 1.05$. The time of reaction, in microsec, from $(NO_2)_F$ to $(NO_2)_r$ is 150 (Eq. [10]), 120 (Eq. [13]), 120 (Eq. [18]). The half life (Eq. [13]) is 340 starting at $(NO_2)_F$. To go from $(NO_2)_e$ to $(NO_2)_r$ (Eq. [13]) gives 140, and all these numbers are of about the same magnitude.

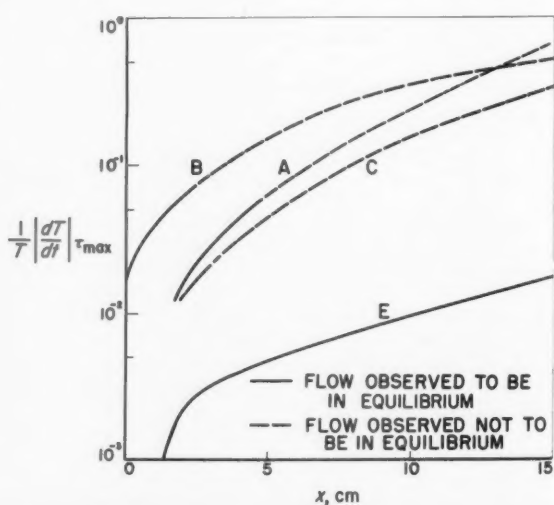


Fig. 7 Characteristic time criterion for several experiments

curves in Figs. 5-7 without appreciably affecting their basic trends. The same finding is given by Bray (6), who states that the approximate solution of Equation [18] leads to appreciable errors if compared with this exact calculations on hypersonic nozzle flow. It is in this context that Logan's predictions (4) are to be viewed with care. Penner himself implies (1) that such detailed results as hoped for by Logan, and in our calculations ought not to be expected. He suggests⁷ that higher order terms in the Taylor series must be retained to obtain more realistic results. However, some important correct qualitative facts emerge from Figs. 5-7. All experiments show minimum temperature lag values initially in the expansion. This finding agrees with the trend of the curves for N recombination, O recombination, etc., in hypersonic nozzles given by Logan (4). Therefore, qualitatively, we find in the regions of the largest temperature gradients (or shortest characteristic flow times) near the nozzle throat, that the flow is closer to equilibrium than at the exit. This behavior can also be seen in the complete calculations on hydrogen recombination in a rocket nozzle by Krieger (15). Another complete calculation by Heims (16), who determined the recombination of atomic oxygen in hypersonic stagnation point flow (or nozzle flow), shows the same result. It is therefore clear that, in recombination reactions in expansions, the initial regions of near sonic flows are those in which thermodynamic equilibrium is likely to prevail, as shown experimentally or theoretically in many instances (5,6,10,14, 15,16). Unfortunately, the opposite statement is occasionally found in the literature.

Criterion Based on Terms in the Rate Equation

Bray (5,6) calculates the flow of initially dissociated nitrogen and oxygen through a hypersonic nozzle using the model of Lighthill's ideal dissociating gas (7) with Freeman's rate parameter (8) chosen to adapt numerical results to the current range of uncertainty of the actual rate constants. Bray finds that the hypersonic nozzle flow may be qualitatively described by observing three flow regions. Initially the flow is in equilibrium and follows the prediction of the law of mass action. Next, there is a short transitional regime in which the flow departs markedly from equilibrium, and finally the flow is essentially frozen. The choice of a range of rate constants affects only the axial location of the departure from equilibrium, not the described three stages of the expansion. Based on the finding of the apparent "sudden freezing" of the flow, computed with the full equations, Bray proposes a simpler approximate solution in which the flow is initially in equilibrium; the point of "sudden freezing" in the nozzle is determined by a criterion based on the rate equation, and from then on we have frozen flow. This behavior is remarkably similar to that observed in our system, as shown on Fig. 4. Bray (6) suggests that it may be possible to apply his criterion to a real gas, and we will do this with our system. The rate Equation [9] with Equation [3] gives

$$\left(-\frac{d\alpha}{dt} \right)_A = 2 \frac{(N_2)}{(NO_2)_F} [k_R(NO_2)^2 - k_D(N_2O_4)] \quad [21]$$

where the subscript *A* signifies that at a given nozzle station for which the equation is evaluated numerically, the area is to be held constant so $(NO_2)_F = \text{constant}$ and $d(NO_2)_F/dt = 0$. In this manner conditions at various stations may be compared directly. With this restriction in mind, Equation [21] may be shortened by

$$-\frac{d\alpha}{dt} = R - D \quad [22]$$

where *R* and *D* are the recombination and dissociation rate functions implied in Equation [21]. The left-hand side of

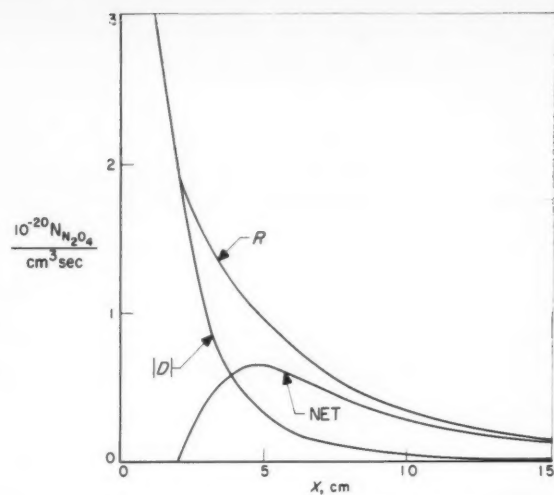


Fig. 8 Dissociation and recombination terms for experiment B

Equation [22] is positive in expansions, since α decreases with time (or distance), and the rate approaches zero if the nozzle flow becomes frozen. Initially, in the nozzle we have equilibrium; the net recombination rate is small; *R* and *D* are large terms, and they are about equal. These statements applied to Equation [22] lead to the inequality

$$-\frac{d\alpha}{dt} \ll D \quad [23]$$

as a requirement for the flow to be near equilibrium. Farther down the nozzle, with concentrations and temperature decreasing, both *R* and *D* fall rapidly. Beginning in the transition region or region of departure from equilibrium, *D* approaches zero faster than *R*, owing to the strong temperature dependence of the dissociation rate constant. Finally, beyond the departure from equilibrium, the flow may be viewed as nearly frozen with the left-hand side of Equation [22] approaching zero. In almost frozen flow, *D* will be negligibly small; the net rate of the reaction is about equal to the recombination term *R*, and we obtain from Equation [22] the inequality

$$-\frac{d\alpha}{dt} \gg D \quad [24]$$

as a condition for near frozen flow. To verify this view of the expansion, we may compute the terms *D* and *R* from the complete equations, and they are plotted in Fig. 8 for experiment B. Here we see the number of N_2O_4 molecules produced by the recombination term or destroyed by the dissociation term per unit volume and unit time. Initially in chemical equilibrium on the scale shown, *R* is about equal to *D*, and both are large, and the net production $R - D$ is small. After departure from equilibrium, *D* drops rapidly to negligible values. In fact, at the nozzle exit the net production of N_2O_4 is practically equal to *R*, which, however, is also a small value, a result which leads to practically frozen flow. With the inequalities of Equations [23 and 24] borne out by the experiment, it is logical to ask for the approximate condition of departure from equilibrium or sudden freezing. Since the net production term is much smaller than *D* in near equilibrium, and much larger than *D* for near frozen flow, Bray assumes that somewhere in the region of departure the two terms may be of the same order of magnitude, setting

$$-\frac{d\alpha}{dt} = AD \quad [25]$$

where it is hoped that *A* is a constant of order unity. The

⁷ Private communication from Dr. S. Penner.

great practical advantage of this criterion for predicting departure from equilibrium is that both sides of Equation [25] may be evaluated at equilibrium since the flow is in this condition up to the departure point. From Equation [22] we may then write

$$-(d\alpha/dt)_e = A D_e \approx AR_e \quad [26]$$

since $D \approx R$ near equilibrium; and R_e is simpler to compute since k_R is constant for our reaction. With $d\alpha/dt = u d\alpha/dx$,

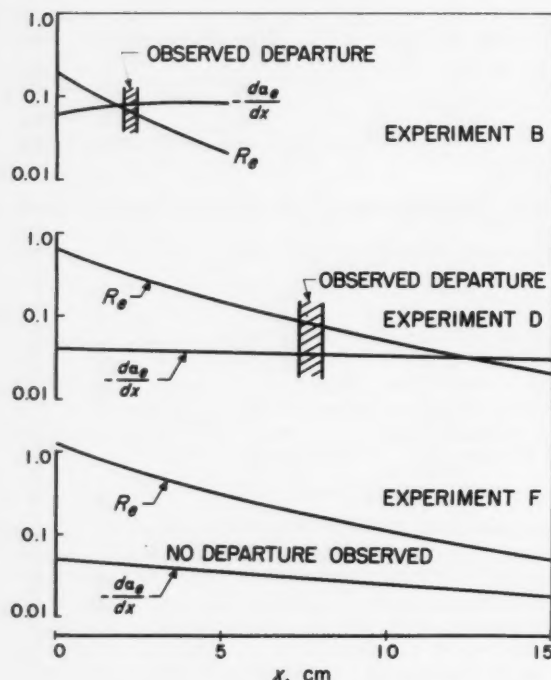


Fig. 9 Criterion based on comparison of dissociation rate term with rate of change of degree of dissociation for three experiments

and with Equations [21 and 26], the criterion for sudden freezing for our reaction finally becomes

$$-\frac{d\alpha_e}{dx} = Ak_R \frac{2(N_2)(NO_2)_e^2}{u(NO_2)_F} \quad [27]$$

The results of three calculations with this criterion are shown in Fig. 9. They were obtained by inserting in Equation [27] values from a complete calculation for chemical equilibrium with Equations [4-8], which include the variation of $(NO_2)_F$ with x . Also shown in Fig. 9 are the experimentally observed departure points from chemical equilibrium (Table 1). The agreement of prediction and observation for experiment B is remarkable (i.e., $A \approx 1$), and for experiment F departure is neither observed nor predicted. From Equation [27], A may be expressed by choosing the value of the other terms at the observed departure point. The results are $0.42 < A < 1.25$; i.e., the departure ordinarily occurs upstream of the point of prediction with $A < 1$.

Of particular interest to hypersonic tunnel design is the fact that once the flow departs from equilibrium, it will not readily return to this state in the region of the test section. In particular, it is fallacious to assume that mere tunnel size will materially affect this behavior. The additional length of test section, in units of nozzle length L , needed at constant flow conditions to return the flow to near equilibrium is shown in Fig. 10. Calculations with Equations [10 and 13] are given, and the limits of the simplified calculation are clearly seen. More than 10 nozzle lengths must be added to the nozzle to return to near equilibrium; because of the very low rate of recombination, this is not a surprising result.

Conclusions

The fully determined nozzle flow system with two reacting species lends itself, indeed, to a check of approximate methods to determine departures from thermodynamic equilibrium. The important point is that these checks can be made without resorting to approximations. It was found that methods based on characteristic flow and relaxation times, as developed for rocket nozzles and also applied to hypersonic flow problems, do not furnish sufficient detail for predictions of points of departure from equilibrium. They are valuable, at most, to generally indicate in which regions of the flow such departures are likely. A method recently proposed by Bray using Lighthill's ideal dissociating gas is based on an estimate of the magnitude of the dissociation rate term computed for chemical equilibrium with the change of degree of dissociation, and it was shown to give satisfactory results when extended to a real gas flow. Aside from a reasonable prediction of points of departure from thermodynamic equilibrium, the method also sheds light on the physical understanding of flows in expansions with reactions that are primarily those of three-body recombinations. Contrary to statements occasionally found in the literature, it can be shown that chemical equilibrium in expansions is most likely to prevail in the regions of high temperature gradients initially in the expansion. It appears that this fact is independent of the area ratio of the nozzle or the substance used, within wide ranges covering rocket nozzles, as well as hypersonic wind tunnel nozzles. It is further found that once departure from equilibrium takes place, no practical test section length of a hypersonic nozzle will bring about the return to equilibrium, and that the mere invocation of large-scale equipment occasionally proposed is not a guarantee of sustained chemical equilibrium.

Acknowledgment

The continuous assistance of Jack E. Marte during the experimental phase of this program is gratefully acknowledged.

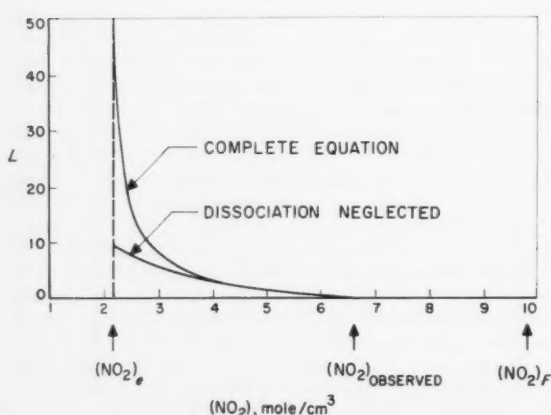


Fig. 10 Test section length needed in terms of nozzle length L to return to chemical equilibrium from nozzle exit conditions for experiment B

Nomenclature

A	= cross-sectional area of nozzle
A, B	= constants
C	= defined by Equation [11]
h	= enthalpy per unit mass
Δh	= heat of dissociation per unit mass
k_D	= dissociation rate constant
k_R	= recombination rate constant
K_c, K_p	= equilibrium constants
L	= nozzle length
m	= mass flow
p	= pressure
R	= universal gas constant
T	= temperature
u	= velocity
x	= distance on nozzle center line
α	= degree of dissociation
μ	= molecular weight
ρ	= density
τ	= time interval
Φ	= reactant concentration in the nozzle supply
ω	= mass fraction, i.e., $\omega_1 = m_1/m$
(\cdot)	= concentration

Subscripts

0	= supply conditions
c	= chemical equilibrium
F	= frozen flow

Symbols without subscripts refer to the mixture

References

- 1 Penner, S. S., "Introduction to the Study of Chemical Reactions in Flow Systems," Butterworth's Scientific Pub., London, 1955.
- 2 Penner, S. S., "Chemistry Problems in Jet Propulsion," Pergamon Press, London, 1957.
- 3 Altman, D. and Carter, J. M., "Nonequilibrium Effects," in "High Speed Aerodynamics and Jet Propulsion," Princeton University Press, N. J., 1956, vol. II, part 1-B-4.
- 4 Logan, J. G., "Relaxation Phenomena in Hypersonic Aerodynamics," IAS Preprint no. 728, Jan. 1957.
- 5 Bray, K. N. C., "Departure from Dissociation Equilibrium in a Hypersonic Nozzle," Aeron. Research Council, London, rep. no. 19,983, March 1958.
- 6 Bray, K. N. C., "Atomic Recombination in a Hypersonic Wind-Tunnel Nozzle," *J. Fluid Mech.*, July 1959, vol. 6, pp. 1-32.
- 7 Lighthill, M. J., "Dynamics of a Dissociating Gas, Part 1: Equilibrium Flow," *J. Fluid Mech.*, Jan. 1957, vol. 2, pp. 1-32.
- 8 Freeman, N. C., "Nonequilibrium Flow of an Ideal Dissociating Gas," *J. Fluid Mech.*, Aug. 1958, vol. 4, pp. 407-425.
- 9 Rudin, M., "Criteria for Thermodynamic Equilibrium in Gas Flow," *Phys. Fluids*, Sept.-Oct. 1958, vol. 1, pp. 384-392.
- 10 Wegener, P. P., "Supersonic Nozzle Flow with a Reacting Gas Mixture," *Phys. Fluids*, May-June 1959, vol. 2, pp. 264-275.
- 11 Gray, P. and Yoffe, A. S., "The Reactivity and Structure of Nitrogen Dioxide," *Chem. Rev.*, Dec. 1955, vol. 55, pp. 1069-1154.
- 12 Carrington, T. and Davidson, N., "Shock Waves in Chemical Kinetics: The Rate of Dissociation of N_2O_4 ," *J. Phys. Chem.*, April 1953, vol. 57, pp. 418-427.
- 13 Wegener, P. P., "Measurement of Rate Constants of Fast Reactions in a Supersonic Nozzle," *J. Chem. Phys.*, April 1958, vol. 28, pp. 724-725.
- 14 Wegener, P. P., Marte, J. E. and Thiele, C., "Experiments on Chemical Kinetics in a Supersonic Nozzle," *J. Aeron. Sci.*, March 1958, vol. 25, pp. 205-206.
- 15 Krieger, F. J., "Chemical Kinetics and Rocket Nozzle Design," *JOURNAL OF THE AMERICAN ROCKET SOCIETY*, Nov. 1951, vol. 21, pp. 179-185.
- 16 Heims, S. P., "Effect of Oxygen Recombination on One-Dimensional Flow at High Mach Numbers," NACA TN 4144, Washington, D.C., Jan. 1958.

Transport and Thermodynamic Properties in a Hypersonic Laminar Boundary Layer Part 2 Applications¹

SINCLAIRE M. SCALA² and
CHARLES W. BAULKNIGHT³

General Electric Co.
Philadelphia, Pa.

An analysis is presented in which the transport and thermodynamic properties of dissociated air, which were presented in Part 1 of this paper, and the Curtiss, Hirschfelder and Bird method of predicting the thermal conductivity of a chemically reacting gas, are utilized in the determination of stagnation point heat transfer to a hypersonic vehicle. New theoretical results are obtained for stagnation point heat transfer, and these are compared with earlier theoretical results, and with available experimental data. It is found that at both high and low altitudes the authors' results are larger than the theoretical values predicted by Sibulkin and Lees, but smaller than those of Romig, and Fay and Riddell. It is also found that the authors' results are consistently lower than the mean value of the shock tube data of Rose and Stark, and Vitale et al. However, it is noted that the scatter in the experimental data on heat transfer is of the same order as the variation in the different theoretical predictions.

THE PROBLEM of accurately predicting the stagnation point heat transfer rate for hypersonic flow is treated in two parts. The first is the determination of the transport and thermodynamic properties of high temperature dissociated

air. [See Part 1 (1).⁴] The second part consists of the solution of the boundary layer equations utilizing these properties. Considered in this manner, a given solution of the boundary layer equations is as "exact" as the particular set

⁴ Numbers in parentheses indicate References at end of paper.

⁵ Regarding Part 1 of this paper, note the following corrections: Equation [3]

$$[\mathcal{D}_{12}]_b = 1.171 \times 10^{-6} T^{3/2} \left[\frac{m_1 + m_2}{2m_1 m_2} \right]^{1/2} \sigma_{12}^{-2} \frac{\text{ft}^2}{\text{sec}}$$

Table 1: Species $\text{N}_2, \epsilon/k = 79.8 \text{ K}$.

Received Feb. 18, 1959, and revised Feb. 10, 1960.

¹ This paper is a revised version of General Electric Co., MSVD, TIS no. R59SD306, Feb. 1959.

² Manager, High Altitude Aerodynamics, Space Sciences Laboratory. Member ARS.

³ Physical Chemist, Space Sciences Laboratory. Member ARS.

of gas properties utilized in the analysis is "accurate."

Earlier studies of stagnation point heat transfer by Sibulkin (2), Lees (3), Romig (4) and Fay and Riddell (5) have incorporated assumptions such as those given in Equations [12]. In this paper all of the transport and thermodynamic properties of dissociated air were evaluated during the solution of the differential equations, as a function of the local gas composition and temperature within the boundary layer.

Since there is no simple way of distinguishing between the separate effects of variable Prandtl number, Lewis number, viscosity, thermal conductivity, etc., our results are compared with earlier work on the basis of the gross stagnation point heat transfer to the surface, for given environmental conditions.

Boundary Layer Calculations

The gas in a hypersonic boundary layer is actually a multi-component mixture of the products of dissociated air; it is convenient in first approximation to treat the gas as a binary mixture of "air atoms" and "air molecules" (3), whose thermodynamic and transport properties are then averaged in some appropriate manner.

Consider the laminar flow around a blunt axially symmetric body; the boundary layer equations which represent the conservation laws for a binary gaseous mixture may be written (6) as follows:

Global conservation of mass

$$\frac{\partial}{\partial x} (\rho u r_0) + \frac{\partial}{\partial y} (\rho v r_0) = 0 \quad [1]$$

Conservation of species i

$$\rho \left(u \frac{\partial c_i}{\partial x} + v \frac{\partial c_i}{\partial y} \right) = \frac{\partial}{\partial y} \left(\rho \mathfrak{D}_{ij} \frac{\partial c_i}{\partial y} + \frac{D_{i^T}}{T} \frac{\partial T}{\partial y} \right) + \dot{w}_i \quad [2]$$

Conservation of momentum neglecting centrifugal effects

$$\rho \left(u \frac{\partial u}{\partial x} + v \frac{\partial u}{\partial y} \right) = - \frac{\partial p}{\partial x} + \frac{\partial}{\partial y} \left(\mu \frac{\partial u}{\partial y} \right) \quad [3]$$

Conservation of energy neglecting the Dufour effect

$$\begin{aligned} \rho \left(u \frac{\partial T}{\partial x} + v \frac{\partial T}{\partial y} \right) &= u \frac{\partial p}{\partial x} + \mu \left(\frac{\partial u}{\partial y} \right)^2 + \frac{\partial}{\partial y} \left(K \frac{\partial T}{\partial y} \right) + \\ &\sum_i \left[c_{pi} \left(\rho \mathfrak{D}_{ij} \frac{\partial c_i}{\partial y} + \frac{D_{i^T}}{T} \frac{\partial T}{\partial y} \right) \right] \frac{\partial T}{\partial y} - \sum_i \dot{w}_i h_i \end{aligned} \quad [4]$$

It is noted that the diffusion coefficients have been defined so that the binary diffusion coefficient \mathfrak{D}_{ij} and the thermal diffusion coefficient D_{i^T} satisfy the following equation for the diffusion flux of the i th species

$$\rho \vec{V}_i = - \rho \mathfrak{D}_{ij} \nabla c_i - D_{i^T} \nabla \ln T \quad [5]$$

Although the effects of thermal diffusion have been largely ignored, a hypersonic boundary layer exhibits steep thermal gradients and large differences in the molecular masses of the gaseous species present, which tend to promote the occurrence of this phenomenon. Consequently, one of the authors has usually included thermal diffusion in his analyses (7). It is also noted that a special case exists when the Lewis number is unity and thermal diffusion is neglected.

Upon multiplying Equation [2] by h_i and taking the summation over i , the heat release term due to chemical reactions can be eliminated from Equation [4] to yield

$$\begin{aligned} \rho \left(u \frac{\partial h}{\partial x} + v \frac{\partial h}{\partial y} \right) &= u \frac{\partial p}{\partial x} + \mu \left(\frac{\partial u}{\partial y} \right)^2 + \frac{\partial}{\partial y} \left(K \frac{\partial T}{\partial y} \right) + \\ &\frac{\partial}{\partial y} \left[\sum_i h_i \left(\rho \mathfrak{D}_{ij} \frac{\partial c_i}{\partial y} + D_{i^T} \frac{\partial T}{\partial y} \right) \right] \end{aligned} \quad [6]$$

This form does not contain the chemical source term. However, nothing has yet been gained since the composition gradient $\partial c_i / \partial y$ still appears in the last term on the right-hand side. Thus, the diffusion equation is still required. However, noting that $h = \sum_i c_i h_i$, the $(\partial / \partial y)(K \partial T / \partial y)$ term

may be eliminated from Equation [6]

$$\begin{aligned} \rho \left(u \frac{\partial h}{\partial x} + v \frac{\partial h}{\partial y} \right) &= u \frac{\partial p}{\partial x} + \mu \left(\frac{\partial u}{\partial y} \right)^2 + \frac{\partial}{\partial y} \left(\frac{K}{\epsilon_p} \frac{\partial h}{\partial y} \right) + \\ &\frac{\partial}{\partial y} \left[\sum_i h_i \left\{ \left(\rho \mathfrak{D}_{ij} - \frac{K}{\epsilon_p} \right) \frac{\partial c_i}{\partial y} + \frac{D_{i^T}}{T} \frac{\partial T}{\partial y} \right\} \right] \end{aligned} \quad [7]$$

Introducing the Prandtl and Lewis numbers, the latter becomes

$$\begin{aligned} \rho \left(u \frac{\partial h}{\partial x} + v \frac{\partial h}{\partial y} \right) &= u \frac{\partial p}{\partial x} + \mu \left(\frac{\partial u}{\partial y} \right)^2 + \frac{\partial}{\partial y} \left(\frac{\mu}{Pr} \frac{\partial h}{\partial y} \right) + \\ &\frac{\partial}{\partial y} \left[\sum_i h_i \left\{ \frac{\mu}{Pr} (Le - 1) \frac{\partial c_i}{\partial y} + \frac{D_{i^T}}{T} \frac{\partial T}{\partial y} \right\} \right] \end{aligned} \quad [8]$$

If the Lewis number is unity and thermal diffusion can be neglected, the energy equation becomes

$$\rho \left(u \frac{\partial h}{\partial x} + v \frac{\partial h}{\partial y} \right) = u \frac{\partial p}{\partial x} + \mu \left(\frac{\partial u}{\partial y} \right)^2 + \frac{\partial}{\partial y} \left(\frac{\mu}{Pr} \frac{\partial h}{\partial y} \right) \quad [9]$$

This form constitutes an enormous simplification over Equations [4 or 6], since now the diffusion equation is completely uncoupled, and the effects of the chemical heat release term $\sum_i \dot{w}_i h_i$ are included implicitly without recourse to a chemical rate equation.

Note that a very similar type of equation can also be written in terms of the stagnation enthalpy $H = h + u^2/2$

$$\begin{aligned} \rho \left(u \frac{\partial H}{\partial x} + v \frac{\partial H}{\partial y} \right) &= \frac{\partial}{\partial y} \left[\mu \left(1 - \frac{1}{Pr} \right) \frac{\partial (u^2/2)}{\partial y} \right] + \\ &\frac{\partial}{\partial y} \left[\frac{K}{\epsilon_p} \frac{\partial H}{\partial y} \right] + \frac{\partial}{\partial y} \left[\sum_i h_i \left\{ \frac{\mu}{Pr} (Le - 1) \frac{\partial c_i}{\partial y} + \frac{D_{i^T}}{T} \frac{\partial T}{\partial y} \right\} \right] \end{aligned} \quad [10]$$

so that, upon assuming the Lewis number to be unity and neglecting thermal diffusion, the latter becomes

$$\begin{aligned} \rho \left(u \frac{\partial H}{\partial x} + v \frac{\partial H}{\partial y} \right) &= \frac{\partial}{\partial y} \left[\mu \left(1 - \frac{1}{Pr} \right) \frac{\partial (u^2/2)}{\partial y} \right] + \\ &\frac{\partial}{\partial y} \left[\frac{\mu}{Pr} \frac{\partial H}{\partial y} \right] \end{aligned} \quad [11]$$

Therefore, the utilization of Equations [9 or 11] uncouples the diffusion equation even for the case of a nonequilibrium flow without resorting to any specific constraint on the chemical source term. That is, the $\sum_i \dot{w}_i h_i$ term is accounted for implicitly; i.e., it adjusts itself.

The difficulty is that now the fluid properties cannot be properly evaluated, since there is no direct step from the enthalpy to the properties which depend on both the temperature and the composition. Of course, in first approximation, one could use the properties of a gas which is in thermodynamic equilibrium between the same limits of free stream and wall enthalpy, but this approach may not prove to be satisfactory. It appears that for a precise treatment of boundary layers containing chemically reacting components, even if the $\sum_i \dot{w}_i h_i$ term is eliminated from the energy equation, the diffusion equation which contains the \dot{w}_i term is still required. The diffusion equation must, in fact, be utilized

simultaneously with the other equations in order to evaluate the composition and temperature, so that the transport and thermodynamic properties can be properly calculated. It is noted that in an approximate solution, the use of assumptions such as

$$\begin{aligned} \rho\mu &= \text{constant} \\ \bar{m} &= \text{constant} \\ Pr &= \text{constant} \\ Le &= \text{unity} \\ \bar{c}_p &= \text{constant} \\ \dots &\dots \end{aligned} \quad [12]$$

eliminates the need for evaluation of the transport and thermodynamic properties, but conclusions must be drawn with consideration of these assumptions.

In the analysis, in which dissociated air was treated as a binary mixture of air atoms and air molecules, the properties of the gaseous mixture were determined during the course of the solution of the boundary layer equations in terms of the local gas composition and temperature.

For the binary mixture approximation, the following arbitrary assumptions were utilized

$$\begin{aligned} m_A &= 15 & m_M &= 30 \\ \mathfrak{D}_{AM} &\cong \mathfrak{D}_{ON_2} \\ \mu_A &\cong (1/2)(\mu_O + \mu_N) \\ \mu_M &\cong \mu_{NO} \\ c_{pA} &= c_{\text{pair atom}} \\ c_{pM} &= c_{\text{pair molecule}} \\ \dots &\dots \end{aligned} \quad [13]$$

and a mass weighted heat of formation was taken as

$$\Delta h_{fA^0} = \Delta h_{fN^0} - \left(\frac{c_O}{c_O + c_N} \right)_s [\Delta h_{fN^0} - \Delta h_{fO^0}] \quad [14]$$

In order to include the effects of thermal diffusion, which may be important in the nonequilibrium boundary layer, the thermal diffusion ratio defined by (8)

$$k_T = \frac{\rho}{n_1^2 m_1 m_2} \frac{D_1 T}{[\mathfrak{D}_{12}]_1} \quad [15]$$

was introduced, where, if $k_T > 0$, component 1 diffuses from the hot to the cold region and vice versa. It is also noted that $D_1 T = -D_2 T$, where the first approximation to the thermal diffusion ratio is given by (8)

$$k_T = \frac{X_1 X_2}{6[K_{12}]_1} \frac{S^{(1)} X_1 - S^{(2)} X_2}{\bar{X}_K + \bar{Y}_K} (6C_{12}^* - 5) \quad [16]$$

The quantities \bar{X}_K , \bar{Y}_K and $[K_{12}]_1$ have been previously introduced in Part 1, and $S^{(1)}$ and $S^{(2)}$ are unique functions of m_1 , m_2 , K_1 , K_{12} , K_2 and A_{12}^* , where A_{12}^* and C_{12}^* are functions of the reduced temperature T^* (8).

Upon applying the Mangler and Dorodnitsyn transformations (3)

$$\eta = \frac{\rho_e u_e}{\sqrt{2\xi}} \int_0^\eta \frac{\rho}{\rho_e} r dy \quad [17]$$

$$\xi = \int_0^x \rho_w \mu_w u_e r_0^2 dx \quad [18]$$

to Equations [1-4], one obtains the following set of ordinary differential equations:

Conservation of atoms

$$\begin{aligned} \left[\frac{l}{Pr} \left(Le c_{A\theta} Z_{A\eta} + \frac{Le^T}{\theta} \theta_\eta \right) \right]_\eta + f c_{A\theta} Z_{A\eta} + \\ \frac{\dot{w}_A}{2\rho (du_e/dx)_s} = 0 \quad [19] \end{aligned}$$

Momentum

$$(lf_{\eta\eta})_\eta + ff_{\eta\eta} + \frac{1}{2} \left(\frac{\rho_e}{\rho} - f_\eta^2 \right) = 0 \quad [20]$$

Energy

$$\begin{aligned} \left(\frac{c_p l}{Pr} \theta_\eta \right)_\eta + \bar{c}_p f \theta_\eta + \frac{l}{Pr} \theta_\eta (c_{pA} - c_{pM}) \times \\ \left(Le c_{A\theta} Z_{A\eta} + \frac{Le^T}{\theta} \theta_\eta \right) - \frac{\dot{w}_A}{2\rho T_e (du_e/dx)_s} = 0 \quad [21] \end{aligned}$$

These have been utilized recently in a study of catalytic effects in the nonequilibrium hypersonic laminar boundary layer (10).

These equations must satisfy the following boundary conditions. At the surface

$$f_\eta(0) = f_{\eta w} = u_w/u_e = 0 \quad [22]$$

$$f(0) = f_w = -v_w \left[2 \frac{\mu_w}{\rho_w} \left(\frac{du_e}{dx} \right)_s \right]^{-1/2} = 0 \quad [23]$$

$$\theta(0) = \theta_w = T_w/T_e \quad [24]$$

$$Z_A(0) = Z_{Aw} = c_{Aw}/c_{Ae} \quad [25]$$

(assuming no slip or mass transfer at the surface). At the outer edge of the boundary layer

$$\lim_{\eta \rightarrow \infty} f_\eta = \lim_{\eta \rightarrow \infty} \theta = \lim_{\eta \rightarrow \infty} Z_A = 1.0 \quad [26]$$

Once these equations are solved, the resulting heat transfer to the surface which is given by

$$Q_w = \left(-K \frac{\partial T}{\partial y} + \sum_i \rho_i V_i h_i \right)_w \quad [27]$$

becomes

$$\frac{Q_w}{\sqrt{2\rho_w \mu_w (du_e/dx)_s}} = - \left[\frac{\bar{c}_p T_e}{Pr} \theta_\eta + \left(\frac{Le}{Pr} c_{A\theta} Z_{A\eta} + \frac{Le^T}{\theta} \theta_\eta \right) (h_A - h_M) \right]_w \quad [28]$$

in terms of the transformed variables. The minus sign indicates that the heat is transferred to the surface, and the right-hand side of Equation [28] includes the contributions of conduction, ordinary diffusion and thermal diffusion. In these calculations, the authors have assumed that the stagnation point velocity gradient is Newtonian, i.e.

$$\left(\frac{du_e}{dx} \right)_s = \frac{1}{R_B} \sqrt{\frac{2(p_e - p_\infty)}{\rho_e}} \quad [29]$$

Hence the effect of body size appears as the square root of the nose radius $\sqrt{R_B}$.

It is also noted that the results which are obtained in the transformed plane may be transformed back into the physical plane by means of the inverse Mangler-Dorodnitsyn transformation

$$y = \frac{\rho_w}{\rho_e} \left[\frac{2\rho_w}{\mu_w} \left(\frac{du_e}{dx} \right)_s \right]^{-1/2} \int_0^\eta \frac{\rho_e}{\rho} d\eta \quad [30]$$

Discussion of Results

Before discussing the general results which were obtained on an IBM 704 digital computer, attention will be given to a typical boundary layer solution obtained during hypersonic flight. At a Mach number of 20 and an altitude of 120,000 ft, the stagnation point conditions of pressure, temperature and atom concentration at the outer edge of the boundary layer

are estimated as $p_\infty = 2.4$ atm, $T_\infty = 12,400$ R, $c_{Ae} = 0.482$, based on free stream conditions predicted by the 1956 ARDC atmospheric model (11).

A surface temperature of 800 R was selected, and since the atom recombination rates are still not known within several hundred per cent, calculations were performed for a wide range of atom recombination processes. Thus, in Fig. 1 are shown

the nondimensional boundary layer profiles obtained at the stagnation point when it is assumed that the boundary layer is either in "local thermodynamic equilibrium," or when atom recombination is "frozen" in the gas phase and allowed to occur on four surfaces having differing finite catalytic efficiencies (7).

Other results of the computations are shown in Figs. 2-5 where the gas properties are plotted as a function of the local temperature in the boundary layer. It is seen that when it is assumed that the boundary layer is in thermodynamic equilibrium, the contribution of the atomic species to the behavior of the properties of the gaseous mixture is a minimum. Since the wall has a finite catalytic efficiency, when the reactions are frozen the atom concentration builds up on the surface, and the atomic species contribute in larger measure to the properties of the mixture within the boundary layer.

Some of the more interesting results indicate that for low wall temperatures, ϵ_p is not constant (Fig. 2), and, as Fay and Riddell have shown (5), the product of density and viscosity is not constant (Fig. 3). The Prandtl and Lewis numbers were not assumed constant as in previous analyses, but were found to be variable and, furthermore, exhibited gradients which affect the temperature and concentration gradients at the wall. (See Fig. 4 in which the ratio of Prandtl to Lewis number, i.e., the Schmidt number, is shown.) Further, the effects of thermal diffusion were included; the thermal diffusion coefficient is shown in Fig. 5. Note that since the thermal diffusion coefficient is negative, the atoms, which are the lighter particles, diffuse thermally from a low temperature region to a high temperature region. Thus, thermal diffusion tends to oppose concentration diffusion and reduces the diffusion flux of atoms toward the wall.

If one defines the nominal boundary layer thickness in terms of the point at which the velocity in the boundary layer achieves 99.9 per cent of its free stream value, then one obtains the results given in Fig. 6. Since the boundary layer thickness is directly related to the density of the gas in the boundary layer, it is seen that the nominal thickness of the boundary layer increases with decreasing free stream density. Thus, the prime effects are due to changing the altitude. There are slight Mach number and surface temperature effects as well. Higher flight speeds V_∞ tend to compress the gas and decrease the boundary layer thickness. On the other hand, higher surface temperatures T_w act to decrease the mean density of the gas in the boundary layer and hence increase the thickness of the boundary layer.

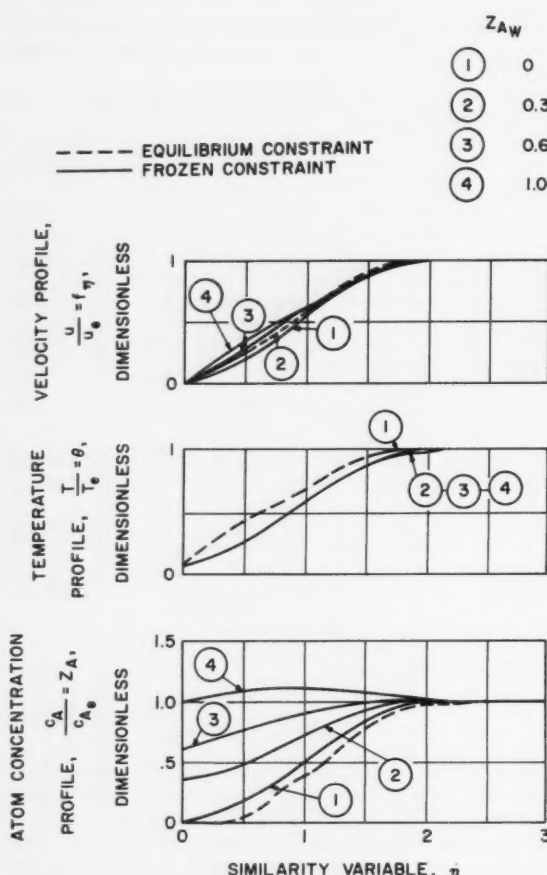


Fig. 1 Boundary layer profiles at Mach 20, altitude 100,000 ft, and a surface temperature of 800 R

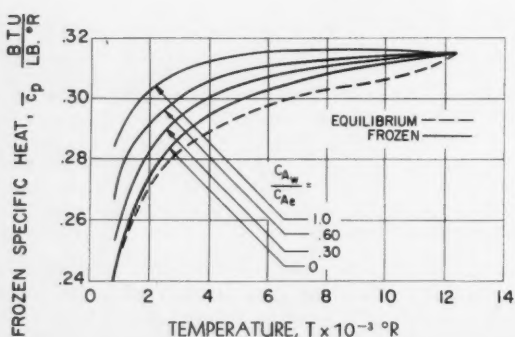


Fig. 2 Frozen specific heat of binary mixture air in boundary layer

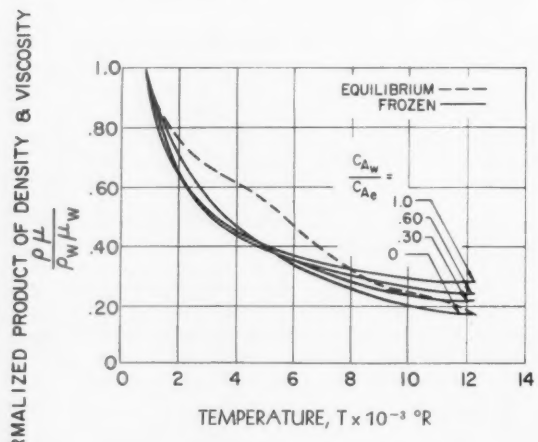


Fig. 3 Normalized product of density and viscosity of binary mixture air in boundary layer

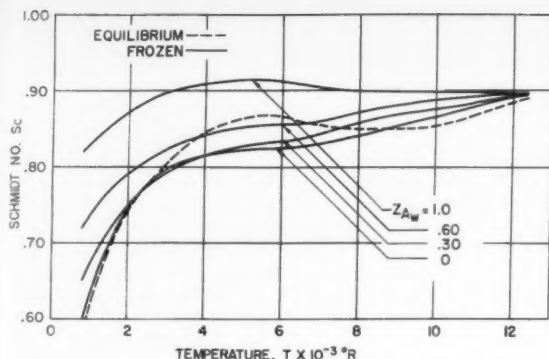


Fig. 4 Variation of Schmidt number of binary mixture air in boundary layer

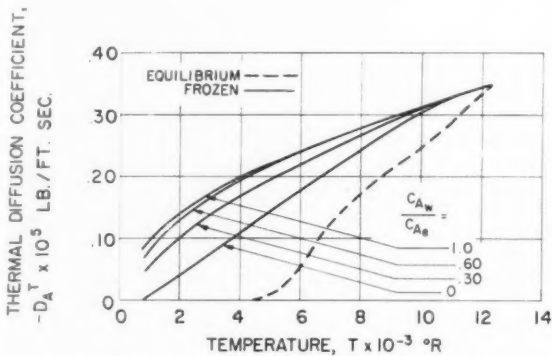


Fig. 5 Thermal diffusion coefficient of binary mixture air in boundary layer

Of greater interest are the results given in Figs. 7 and 8. These curves show the dependence of hypersonic stagnation point heat transfer Q_e (in the absence of mass transfer) upon environmental conditions. The two surface temperatures selected are typical of heat sink vehicles and ablating vehicles. As is readily seen, the heat transfer increases with flight speed and free stream density and decreases with surface temperature. The calculations for heat transfer were performed assuming that the gas was in dissociation equilibrium at the wall. It is noted that when one makes this assumption, the results are virtually independent of the rates of homogeneous atom recombination (3,5,10).

As stated earlier, these results were obtained for variable Prandtl, Lewis and thermal Lewis numbers. Thus, one cannot readily compare our results with analyses in which arbitrary and constant values were selected, except on an absolute basis. This is done in the next section.

At this point it must be noted that the heat transfer results presented in Figs. 7 and 8 are based on the use of the frozen thermal conductivity recently derived by Curtiss, Hirschfelder and Bird (9) and mentioned by the authors in Part 1 (1). For purposes of comparison, the simpler relationship between the thermal conductivity of a binary mixture and the thermal conductivity of the pure species given in Part 1 was also employed. It was found that use of the latter resulted in heat transfer rates which were of the order of 10 per cent lower than those based on the more rigorous Curtiss, Hirschfelder and Bird expression. This may be attributed to the fact that the relation, as derived in (8) for the thermal con-

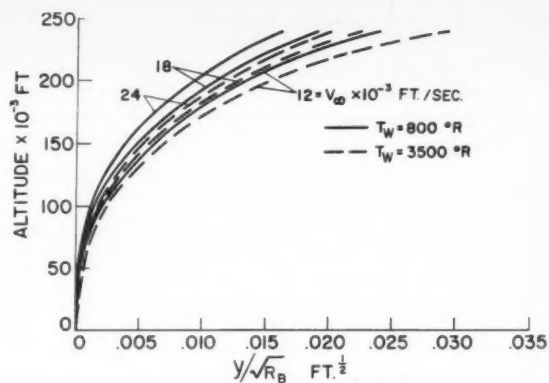


Fig. 6 Nominal thickness of the boundary layer at the stagnation point

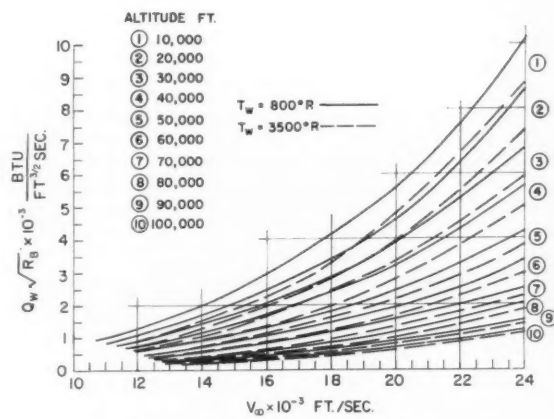


Fig. 7 Heat transfer vs. flight speed—low altitude

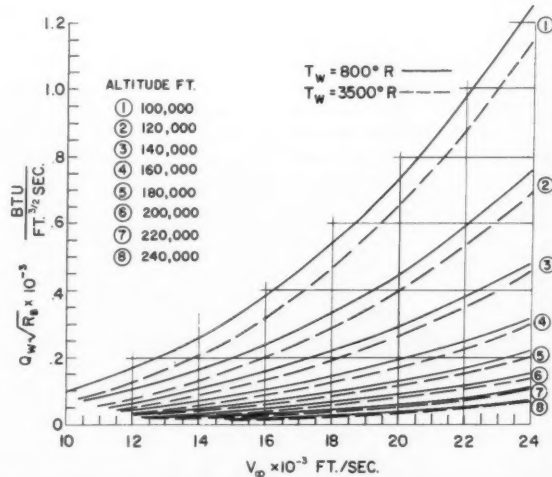


Fig. 8 Heat transfer vs. flight speed—high altitude

ductivity of "binary mixture" dissociated air, yields values which are of the order of 10 to 20 per cent larger than those obtained using the approximate expression presented in Part 1. Hence, although the simpler method may be considered adequate, the more rigorous equation should be used wherever possible.

Comparison With Earlier Work

In some of the earlier theoretical studies (2-5) approximate solutions, exact numerical solutions and empirical correlation formulas have been offered which represent relationships between the stagnation point heat transfer rate, the environmental conditions and the gas properties. Thus, the heat transfer rate can be calculated at a given flight speed and altitude if one has available properties of the standard atmosphere (11), normal shock tables (12,13,14) and transport and thermodynamic property data (1,15).

Sibulkin (2) suggested a heat transfer rate equation based on an extrapolation of a low speed boundary layer solution in the form

$$Q = 0.763(Pr)^{-0.6}(h_e - h_w)[\rho_e \mu_e (du_e/dx)_e]^{1/2} \quad [31]$$

Lees (3) published a formula which is similar to Sibulkin's result, in which the Lewis number was taken equal to unity and $h_w < h_e$

$$Q = 0.71(Pr)^{-2/3}h_e[\rho_e \mu_e (du_e/dx)_e]^{1/2} \quad [32]$$

Romig (4) derived a "reference enthalpy" method for finding the heat transfer rate. Beginning with a form of Sibulkin's equation, she obtained an expression for the heat transfer rate in terms of flight Mach number, nose radius and ambient pressure, but wall temperature effects were not included

$$Q = 0.0145M^{3.1}(p_\infty/R_B)^{1/2} \quad [33]$$

Fay and Riddell (5) have published a complex correlation formula based on extensive numerical solutions for which constant values were assumed for the Prandtl and Lewis numbers

$$Q = 0.763(Pr)^{-0.6}(h_e - h_w) \left(\frac{\rho_w \mu_w}{\rho_e \mu_e} \right)^{0.1} \left[\rho_e \mu_e \left(\frac{du_e}{dx} \right)_e \right]^{1/2} \times \\ \left[1 + (Le^{0.82} - 1) \frac{h_D}{h_e} \right] \quad [34]$$

The magnitude of the heat transfer rate given by each of these four equations clearly depends on the gas properties which are utilized in the correlation formulas. For a fixed

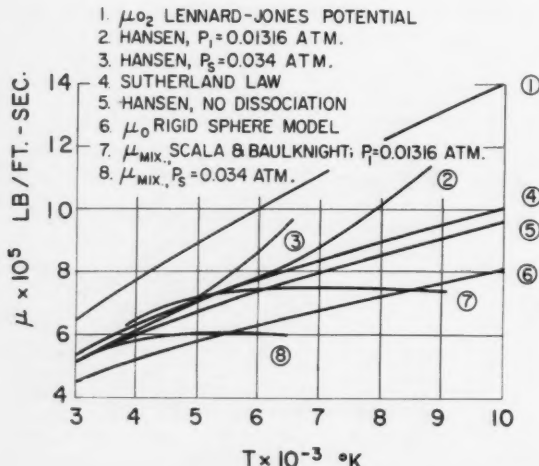


Fig. 9 Comparison of viscosity theories

value of the Prandtl number, the form of these four equations is such that the viscosity of the gas at the outer edge of the boundary layer enters the final result explicitly to the 0.5 power in Equations [31 and 32], implicitly to the 0.5 power in Equation [33] [see (4)], and explicitly to the 0.4 power in Equation [34]. Thus, the uncertainty in the heat transfer rate is 50 per cent of the uncertainty in the value of μ_e appearing in the correlation equations given by Sibulkin, Lees and Romig, and only 40 per cent of the uncertainty in the value of μ_e appearing in Fay and Riddell's equation.

It is therefore interesting to compare the values of the viscosity of dissociated air predicted by a number of different theories. In Fig. 9, we have shown the value of viscosity predicted by the Sutherland law (curve 4), the value of μ_{mix} (curves 7 and 8) predicted by the Buddenberg and Wilke relation (Part 1, Eq. [5]), and the value of the viscosity (curves 2, 3 and 5) predicted by the recent work of Hansen (15). For reference purposes, the viscosity of pure atomic oxygen (curve 6) and pure molecular oxygen (curve 1) given in Part 1 are also shown. It is noted that curves 2 and 7 were calculated for the environmental conditions simulated by Rose and Stark (16), who kept the shock tube initial pressure p_1 constant. Curves 3 and 8 were calculated for the environmental conditions simulated by Vitale et al. (17) who kept the stagnation pressure p_s constant.

It is seen that for the particular choice of the rigid sphere model for the atomic species and the Lennard-Jones model for the molecular species, the predictions of the Buddenberg and Wilke expression utilized by the authors diverge significantly from Hansen's predictions with increasing temperature. (Compare curve 8 with curve 3, and 7 with 2.) Also note that the values of μ_{mix} fall below the Sutherland law values, whereas Hansen's results lie above.

The effects of dissociation upon the viscosity coefficient are particularly pronounced where the stagnation pressure is low and the concentration of atomic species is high, for a given range of hypersonic flight speeds. Therefore, the deviation of the viscosity coefficient from the Sutherland law (which neglects dissociation) appears more strongly in high altitude shock tube simulation, e.g., $p_s = 0.034$ atm, than in low altitude simulation, e.g., $p_s = 0.01316$ atm (see Fig. 9). Thus, the use of different viscosity laws should lead to larger differences in the theoretical heat transfer rates at high altitude than at low altitude.

In the new theoretical calculations presented here, the transport data given in Part 1 were employed. However, for purposes of comparison, the authors' transport data were not used in the empirical correlation formulas [31-34]. Instead, the Prandtl and Lewis numbers were taken as constants, and the Sutherland viscosity law was utilized. Thus, although the Prandtl number is actually a variable, it was taken as a constant ($Pr = 0.71$) in the correlation equations. Although Buddenberg and Wilke's equation is probably more representative of the behavior of a gaseous mixture at high temperatures than is Sutherland's law, the latter was employed by Fay and Riddell. Hence, for consistency with their numerical calculations, it was also employed here explicitly in Equations [31, 32 and 34], and implicitly in Equation [33], since Romig utilized Sutherland's law in the derivation of Equation [33].

The Lewis number, which is actually a variable, was taken as unity by Lees in the derivation of Equation [32] and as a constant by Fay and Riddell. Therefore, for comparison, the Lewis number was taken as $Le = 1.0$ and $Le = 1.4$ in Equation [34].

Shock tube data on stagnation point heat transfer are available only for a limited number of altitude conditions, e.g., Rose and Stark, and Vitale et al. Consequently, representative high and low altitude conditions were investigated, and the theoretical predictions were evaluated for the environmental conditions which were simulated in the shock tube experiments.

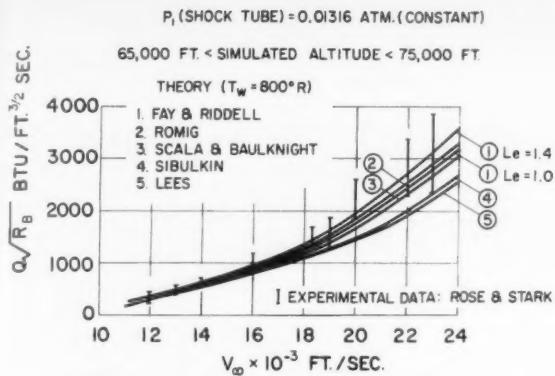


Fig. 10 Comparison of theoretical and experimental heat transfer—low altitude

Fig. 10 shows a comparison between theory and experiment at simulated altitudes in the range 65,000 to 75,000 ft. It is seen that the predictions of Fay and Riddell, Romig, and Scala and Baulknight fall within the scattered experimental data points of Rose and Stark, whereas the values predicted by Sibulkin and Lees fall below.

Fig. 11 shows a comparison between theoretical and experimental results at simulated altitudes in the range 200,000 to 240,000 ft. Here again it is seen that the differences in the theoretical predictions are of the same order as the scatter in the experimental data. It is noted, however, that at the higher altitudes, as anticipated, there is a somewhat more pronounced spread in the different theoretical predictions than at lower altitudes.

It is to be noted that one could, of course, by judicious selection of the transport properties to be inserted in the various correlation equations, appreciably change the magnitude of the individual theoretical predictions of heat transfer, *a posteriori*, until "agreement" with available experimental data is obtained. By way of illustration, Hansen's viscosity data could be used to increase the magnitude of the theoretical heat transfer rates given by Lees' and by Sibulkin's formulas, which would then bring their predictions closer to the available experimental data. Since the same technique can be employed with any correlation formula to obtain a better empirical fit, it is doubtful whether this type of approach can be used to rationalize the superiority of a particular theoretical treatment upon which the correlation formula is based. One still requires independent knowledge of the transport properties of the gaseous system.

Conclusions

The use of the approximate expression for the thermal conductivity of a chemically reacting binary mixture gas discussed in Part 1 [i.e., Eq. [6] of (1)] may be considered adequate for heat transfer calculations, since comparison with the more rigorous expression derived in (8) shows that the error in heat transfer introduced by this relation is only of the order of 10 per cent. However, the Curtiss, Hirschfelder and Bird expression should be used, wherever possible.

When our estimates of the viscosity of dissociated air are compared with those predicted by Sutherland's law and by Hansen (15), it is found that the results diverge significantly with increasing temperature. At low temperatures where dissociation is negligible, one finds, as anticipated, that the three methods yield practically identical results. However, as the level of dissociation rises, Hansen's predictions yield values which are of the order of 25 per cent larger than Sutherland's law and 50 per cent larger than our results for the cases treated here (see Fig. 9).

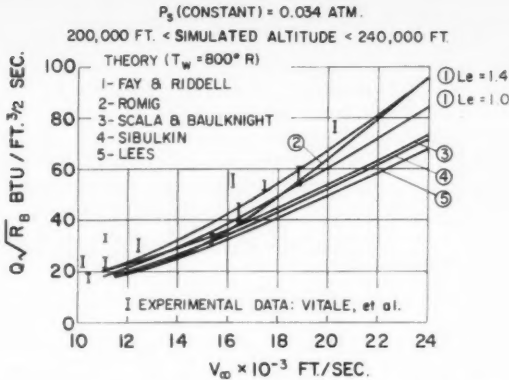


Fig. 11 Comparison of theoretical and experimental heat transfer—high altitude

Since the uncertainty in the theoretical prediction of heat transfer is of the order of 50 per cent of the uncertainty in the coefficient of viscosity, the marked disagreement between the different theoretical predictions of viscosity at high temperature is in itself sufficient justification for an experimental program leading to the determination of high temperature transport properties.

If one accepts the premise that the binary mixture approximation adequately represents the behavior of dissociated air, then the accuracy of the new theoretical heat transfer calculations is not limited by the mathematical model utilized here.

A comparison between the various theoretical predictions of stagnation point heat transfer indicates a maximum deviation of approximately ± 20 per cent from a mean value. The experimental heat transfer data indicates that the scatter obtained at high gas enthalpy levels ($V_\infty > 20,000$ fps) is a maximum of approximately ± 25 per cent from a mean value. On the basis of the relationship between heat transfer and transport properties discussed earlier, it may therefore be concluded that the uncertainty in the experimental data is actually at least equal to, if not greater than, the uncertainty in the high temperature transport properties. This situation at present precludes the possibility of inferring the intermolecular potential function from gross heat transfer data taken at high gas enthalpy levels.

Thus, although the rigid sphere and the Lennard-Jones 6:12 models are undoubtedly only zeroth order approximations for the high temperature behavior of the atomic and molecular species, little evidence exists that any other arbitrary choice of high temperature intermolecular potential function can be exclusively recommended at present.

Finally, a comment should be made with regard to the internal consistency of the calculations of the transport properties of the gaseous mixture. Of the four transport properties utilized in boundary layer calculations, three appear exclusively in the Prandtl, Lewis and thermal Lewis numbers. These are the thermal conductivity coefficient K , the ordinary diffusion coefficient D_{12} and the thermal diffusion coefficient $D_1 T$. Thus, the assumption of specific values for the Prandtl and Lewis numbers appears to preclude the necessity for independently computing these transport coefficients. However, since the coefficient of viscosity appears not only in the Prandtl number but also in the shear stress term in the momentum Equation [3], and in the viscous dissipation term in the energy Equation [4], one must decide on a specific model for the viscosity law.

Since any viscosity law is in fact related to a potential energy function for the intermolecular interactions, the assumption of a particular model implies that all other transport coefficients have also been implicitly specified. Thus, calculations which are based on constant values of the Prandtl

and Lewis numbers may be subject to internal inconsistency, unless it can be shown that the assumption of constant dimensionless groups very nearly represents the actual behavior of the gas. Since the assumption of constant Prandtl and Lewis numbers considerably simplifies the numerical calculations, it is recommended that these dimensionless groups be evaluated at the wall conditions and then held constant across the boundary layer. This would constitute a better approximation than the assumption of arbitrary constants.

Acknowledgments

The authors wish to express their gratitude to Professors J. Hirschfelder and C. Curtiss for their helpful suggestions, and to Leon Gilbert, Barbara Eiseman and Kathleen Burke for their able assistance in the computations. The equations were programmed for digital computation on an IBM 704 by Paul Gordon. This investigation is based on work performed under the auspices of the United States Air Force, Ballistic Missiles Division, Contract no. AF04(645)-24.

Nomenclature

A_{12}^* , C_{12}^*	= functions of $T/(\epsilon_{12}/k)$
c_i	= ρ_i/ρ , mass fraction of species i
c_{p_i}	= $(\partial h_i / \partial T)_p$, specific heat at constant pressure of species i
c_p	= $\sum_i c_i c_{p_i}$, "frozen" specific heat of mixture
D_{12}	= binary diffusion coefficient
D_i^T	= thermal diffusion coefficient
h	= $\sum_i c_i h_i$, enthalpy of mixture
h_i	= static enthalpy of species i , including heat of formation
Δh_f^0	= heat of formation of species i
J	= mechanical equivalent of heat
K_i	= thermal conductivity
k_T	= thermal diffusion ratio
Le	= $\rho c \bar{D}_{12} / K$, "frozen" Lewis number
l	= $\rho \mu_p \rho_w \mu_w$, dimensionless
Le^T	= $\bar{c}_p D_i^T / K$, "frozen" thermal Lewis number
m_i	= molecular weight of species i
M	= Mach number
\overline{m}	= $\sum_i X_i m_i$, molecular weight of mixture
n_i	= moles of species i per unit volume
p	= static pressure
Pr	= $\bar{c} \mu / K$, "frozen" Prandtl number
Sc	= $\mu / \rho \bar{D}_{12}$, Schmidt number
T	= temperature
T^*	= $T/(\epsilon/k)$, reduced temperature
u	= x -component of velocity, parallel to surface
V_i	= diffusion velocity of species i
\vec{v}	= y -component of velocity, normal to surface
\dot{w}_i	= net mass rate of production of species i per unit volume per unit time by chemical reaction

x, y, r_0	= coordinate system
X_i	= mole fraction of species i
Z_i	= c_i/c_{ie} , referred mass fraction of species i
μ	= viscosity
ρ	= density
τ	= $\mu \partial u / \partial y$, shear stress
η, ξ	= similarity variables
θ	= T/T_e , temperature ratio

Subscripts

A	= atomic species
AM	= interaction function for an atom-molecule mixture
D	= dissociation
e	= outer edge of the boundary layer
i	= i th chemical species
M	= molecular species
t	= total
w	= wall
12	= interaction function for a binary mixture of species 1 and species 2
[]	= first approximation

References

- 1 Scala, S. M. and Baulknight, C. W., "Transport and Thermodynamic Properties in a Hypersonic Laminar Boundary Layer, Part I Properties of the Pure Species," *ARS Journal*, vol. 29, no. 1, Jan. 1959, pp. 39-45.
- 2 Sibulkin, M., "Heat Transfer Near the Forward Stagnation Point of a Body of Revolution," *J. Aeron. Sci.*, vol. 19, no. 8, Aug. 1952, pp. 570-571.
- 3 Lees, L., "Laminar Heat Transfer Over Blunt-Nosed Bodies of Revolution at Hypersonic Flight Speeds," *JET PROPULSION*, vol. 26, no. 4, April 1956, pp. 259-269.
- 4 Romig, M. F., "Stagnation Point Heat Transfer for Hypersonic Flow," *JET PROPULSION*, vol. 26, no. 12, Dec. 1956, pp. 1098-1101; Addendum, vol. 27, no. 12, Dec. 1957, p. 1255.
- 5 Fay, J. A. and Riddell, F. R., "Theory of Stagnation Point Heat Transfer in Dissociated Air," *J. Aeron. Sci.*, vol. 25, no. 2, Feb. 1958, pp. 73-85.
- 6 Scala, S. M., "The Equations of Motion in a Multicomponent Chemically Reacting Gas," General Electric Co., M.S.V.D., R.M. no. 5, T.I.S. document no. R58SD205, Dec. 1957.
- 7 Scala, S. M., "Hypersonic Heat Transfer to Catalytic Surfaces," *J. Aeron. Sci.*, vol. 25, no. 4, April 1958, pp. 273-274.
- 8 Hirschfelder, J. O., Curtiss, C. F. and Bird, R. B., "Molecular Theory of Gases and Liquids," John Wiley and Sons, N. Y., 1954.
- 9 Curtiss, C. F., Hirschfelder, J. O. and Bird, R. B., "Theories of Gas Transport Properties," in "Transport Properties in Gases," Northwestern Univ. Press, Jan. 1958, pp. 3-11.
- 10 Scala, S. M., "Hypersonic Stagnation Point Heat Transfer to Surfaces Having Finite Catalytic Efficiency," Proc. Third U. S. Nat. Congress Applied Mechanics, June 1958, pp. 799-806.
- 11 Air Force Cambridge Research Center, "ARDC Model Atmosphere 1956," General Electric Co., M.S.V.D. document no. 56SD233.
- 12 Logan, J. G., Jr., "Normal Shock Calculations in Air," Cornell Aeronautical Lab., Jan. 1957, General Electric Co., Subcontract SDP-1001.
- 13 Feldman, S., "Hypersonic Gas Dynamic Charts for Equilibrium Air," Aeo Research Lab., Jan. 1957.
- 14 Huber, P. W., "Tables and Graphs of Normal Shock Parameters at Hypersonic Mach Numbers," NACA, T.N. 4352, Sept. 1958.
- 15 Hansen, C. F., "Approximations for the Thermodynamic and Transport Properties of High-Temperature Air," NACA, T.N. 4150, March 1958.
- 16 Rose, P. H. and Stark, W. I., "Stagnation Point Heat Transfer Measurements in Dissociated Air," *J. Aeron. Sci.*, vol. 25, no. 2, Feb. 1958, pp. 80-97.
- 17 Vitale, A. E., Kaegi, E. M., Diaconis, N. S. and Warren, W. R., "Results from Aerodynamic Studies of Blunt Bodies in Hypersonic Flows of Partially Dissociated Air," Heat Transfer and Fluid Mechanics Institute, June 1958, pp. 204-215.

Combustion of Highly Reactive Fuels in Supersonic Airstreams¹

EDWARD A. FLETCHER²

ROBERT G. DORSCH³

HARRISON ALLEN Jr.⁴

Lewis Research Center, NASA
Cleveland, Ohio

The feasibility of adding heat to supersonic airstreams by combustion was studied in a small wind tunnel. Aluminum borohydride, pentaborane, hydrocarbon-aluminum borohydride mixtures, trimethylaluminum, diethylaluminum hydride, alkylboranes, alkylboron hydrides and vinylsilane were tested. The first three ignited easily and burned well. The others either failed to ignite or burned only in the diffuser. Trimethylaluminum and diethylaluminum hydride produced light and other evidence of heat evolution when water was simultaneously injected into the tunnel. Gross effects on flow were studied by observation of shock patterns and water sprays injected from the tunnel walls. Examples are given which illustrate the use of these techniques in aerodynamic studies in larger wind tunnels.

ADDITION of heat to a supersonic airstream produces aerodynamic effects which may have application in aircraft propulsion or control. Theoretical studies of heat addition to supersonic flow are reported by a number of authors (1-4).⁵ Practical applications are considered in papers exemplified by (2). A study (2,5,6) was begun several years ago at the NASA Lewis Research Center, of the feasibility of adding heat to a supersonic airstream in the vicinity of airfoil by combustion, in the absence of any disturbances except those caused by the airfoil and by the combustion itself. More recently, a number of other interesting closely related studies have been reported (7,8). It therefore seems appropriate to summarize some of the NASA work at this time.

Aluminum borohydride was originally chosen as the fuel because it ignites readily in air even under extremely severe conditions. However, it presents many problems which detract from its practicality as an aircraft fuel. It decomposes slowly during storage, liberating large volumes of hydrogen. Its extreme reactivity requires that all parts of the fuel system be scrupulously cleaned and purged of air to prevent formation of materials which will plug orifices. It therefore appeared desirable to search for other materials which could be burned in available test facilities, so that further aerodynamic and combustion studies might be carried out with greater ease of fuel handling.

The work was extended to include a study of the possibility of burning other fuels in a small Mach 2 wind tunnel: Pentaborane, trimethylaluminum, diethylaluminum hydride, trimethylborane, triethylborane, alkylboron hydrides, vinylsilane and mixtures of aluminum borohydride with JP-4 (9).

The fuels were injected from the top wall of the wind tunnel. Combustion phenomena were observed by means of high speed Schlieren and direct motion pictures. In addition, the gross nature of the flow field associated with the combus-

tion of aluminum borohydride was studied by observation of the behavior of water streams injected into the stream.

The techniques developed in the combustion work have been applied in a series of aerodynamic studies. They include studies of the effect of the combustion of aluminum borohydride on the pressure distributions around flat plates (10), a body of revolution (11), a supersonic wing in a small (1×1-ft) wind tunnel (12), and various flat plates in a very large (10×10-ft) wind tunnel (12).

This paper describes the techniques used to achieve combustion in supersonic airstreams with several fuels and some of the combustion and flow phenomena which were observed in a small wind tunnel with aluminum borohydride. It also describes the behavior of some of the fuels which could not be ignited under the conditions of the experiment. Finally, examples are given of the aerodynamic studies which have been made in larger wind tunnels; and some of the more important details of the experimental technique used to achieve combustion are presented.

Combustion and Gross Airflow Studies in a Small Wind Tunnel

Apparatus and Procedure

The experimental setup consisted of the wind tunnel, photographic equipment, fuel injection system and ignition system arranged as shown schematically in Fig. 1a.

Wind tunnel

Combustion was studied in a 3.84 × 10-in. supersonic wind tunnel having plate glass sides. The windows ran the entire length of the tunnel down to the subsonic diffuser (Fig. 1b), permitting convenient visual observation and high speed (1000-4000 frames/sec) motion picture photography. The tunnel was operated over a range of Mach numbers with aluminum borohydride. However, most of the work was done at Mach 2. Tunnel stagnation pressures ranged from 37 to 50 in. of mercury. The tunnel air had a nominal dew-point of -20°F and was preheated to 80-110°F. Typical test section conditions are listed in Table 1.

Received Oct. 5, 1959.

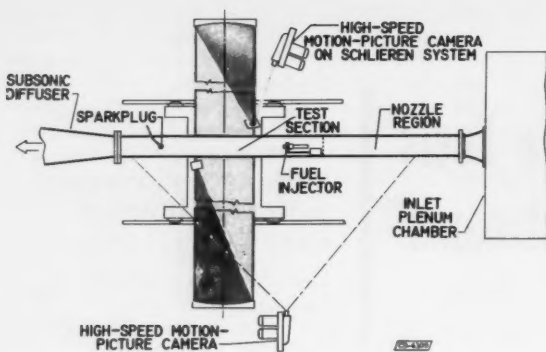
¹ Presented at the Symposium on High Energy Fuels, meeting of the American Chemical Society, Spring, 1959.

² Head, Propellant Chemistry Section. Member ARS.

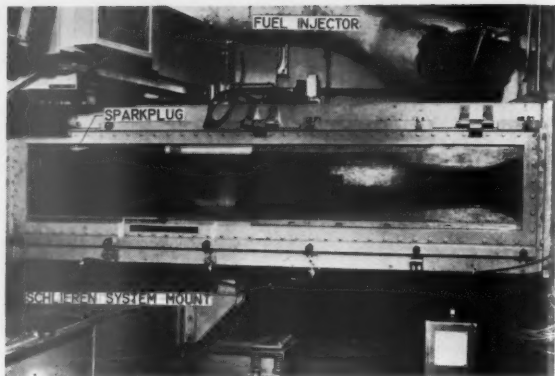
³ Head, Section B, Flow Physics Branch.

⁴ Research Engineer. Member ARS.

⁵ Numbers in parentheses indicate References at end of paper.



(a) Viewed from top of tunnel, showing approximate camera positions



(b) Fuel injector mounted on top wall of tunnel

Fig. 1 3.84 × 10-in. supersonic tunnel

Pressure measurements

Strain gage differential pressure transducers and NASA standard base six capsule differential pressure manometers were used to measure static pressure changes along the centerline of the top wall of the test section. A detailed description of this pressure instrumentation is presented in (10).

A boundary layer study made in this tunnel at Mach 2 (5) indicates that the boundary layer flow at the point of fuel injection is as shown in Fig. 2a. Several stagnation pressure surveys made during the present investigation agreed with these data. Fig. 2b shows the thickness of the boundary layer as a function of the distance downstream of the throat. At the point of fuel injection, the boundary layer is about 0.6-in. thick; however, the subsonic portion of the boundary layer is only about 0.01-in. thick.

Fuel injection

Aluminum borohydride was injected into the airstream by two different techniques. Flow rates of the order of 100 cc per sec (55 gm/sec) were injected for short intervals (3 to 8 millisec) from capsules which were mounted in the wall of the tunnel. The end was merely broken off a pressurized capsule to permit a $\frac{1}{2}$ to 1 cc slug of material to be injected into the stream.

This mode of fuel injection was unsuitable for aerodynamic study and was eventually abandoned in favor of the fuel injector illustrated in Fig. 3. This injector was charged with 5 to 15 cc of fuel through the upper valve either by distillation to the filling arm from a conventional high vacuum system or by direct fuel transfer to the injector in the inert atmosphere of a dry box. The method used depended on the properties of the fuel. The injector was mounted near the upstream end of the test section on the centerline, flush with the top wall of the tunnel. After steady supersonic flow had been established in the tunnel the injector was pressurized with helium through the top valve, the lower valve was opened remotely, and the liquid fuel was sprayed into the tunnel. A considerable variation in the flow rate could be achieved by varying the helium pressure and the injector orifice size. The interchangeable orifice caps are shown in Fig. 3. The duration of the fuel injections varied from 1 to 3 sec.

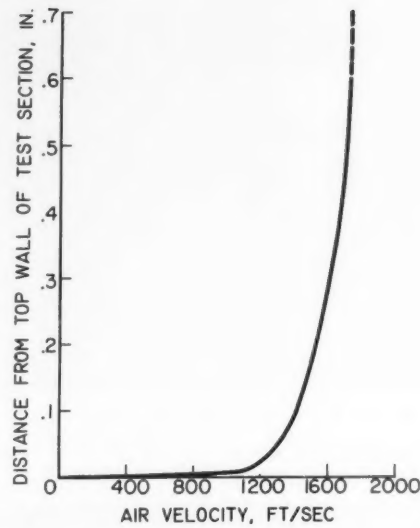
Water or a hydrocarbon fuel (JP-4) was injected during some aluminum borohydride runs through 0.028-in. diameter holes in the top wall of the tunnel. JP-4 was used in order to see if a hydrocarbon flame could be piloted with aluminum borohydride. Water streams were used to study the gross nature of the flow field in the heated region. The difference between the tunnel static pressure and atmospheric pressure forced the liquid into the tunnel.

Ignition system

Aluminum borohydride ejected from capsules usually ignited spontaneously. It was found desirable to introduce a spark plug to insure prompt ignition in the runs where the injector was used because of the lower fuel flow rates (5). The spark plug was mounted 25.25 in. downstream of the fuel injector, as shown in Fig. 1, and produced a 1-joule, five-spark-per-sec repeating capacitance spark. After ignition, the flame, accompanied by a shock wave, quickly traveled upstream to the point of injection and remained there until the fuel was expended.

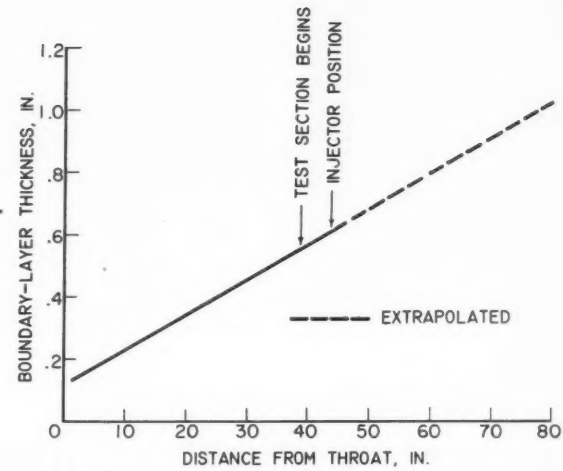
Table 1 Typical test section conditions associated with various Mach numbers in the 3.84 × 10-in. supersonic wind tunnel

Mach number	Static pressure, in. Hg	Static temperature, F	Linear flow velocity, fps	Quality of flow
1.5	12	-74	1443	Fair; static pressure profile irregular, large number of shock waves present
2	5.6	-148	1727	Good; static pressure profile less irregular, fewer shocks present
3	1.3	-260	2082	Excellent; fairly flat static pressure profile, few disturbances
4	0.3	-327	2270	Poor; flow slightly unstable, pressure profile irregular



(a) Velocity profile through boundary layer at point of fuel injection

Fig. 2 Boundary layer flow in 3.84 × 10-in. supersonic wind tunnel at Mach 2



(b) Boundary layer thickness as function of downstream distance from throat of tunnel

Results

Aluminum borohydride

A summary of observations made at Mach 1.5, 2, 3 and 4 with slugs of aluminum borohydride from glass capsules has been presented in (5). Aluminum borohydride almost always ignited and burned vigorously. Flame usually appeared as a momentary, very intense, bright green flash, and was frequently accompanied by a loud bang that could be clearly heard above the very high noise level of the tunnel. The greater part of the combustion took place within a period of about 3 to 8 millisees. Occasionally there were less vigorous runs, where it appeared that the main body of the fuel had not

ignited. In these runs the flame was weak and pale blue. Many of the burnings, however, took place with explosive violence, frequently completely choking the tunnel and driving the flame at very high speed a considerable distance upstream of the point of injection, sometimes almost back to the tunnel throat. An example of such a run is shown in Fig. 4.

No clearly defined structural details, such as a distinctive flame front could be discerned either in the direct or Schlieren photographs. In such runs, burning usually started about 1 millisecond after the start of the fuel injection and continued quite vigorously for about 8 millisees. By this time the main body of the fuel had been used up, but driblets from the

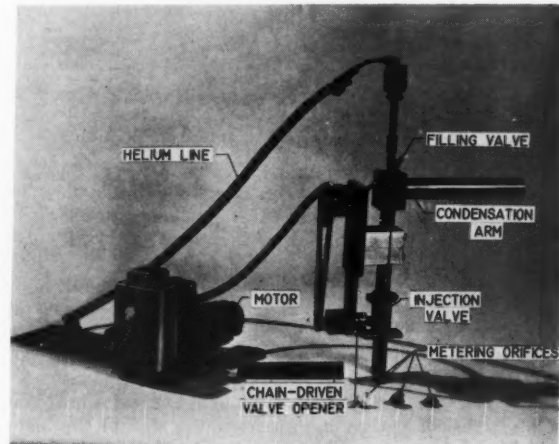
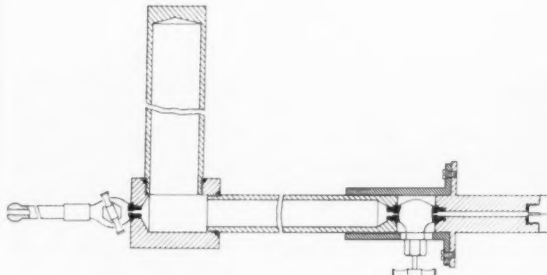


Fig. 3 Fuel injector showing auxiliary remote control opening equipment and helium line



Fig. 4 Open shutter photograph of combustion of $\frac{1}{2}$ -cc slug of aluminum borohydride of Mach 4. Note that flame extends almost back to throat of tunnel

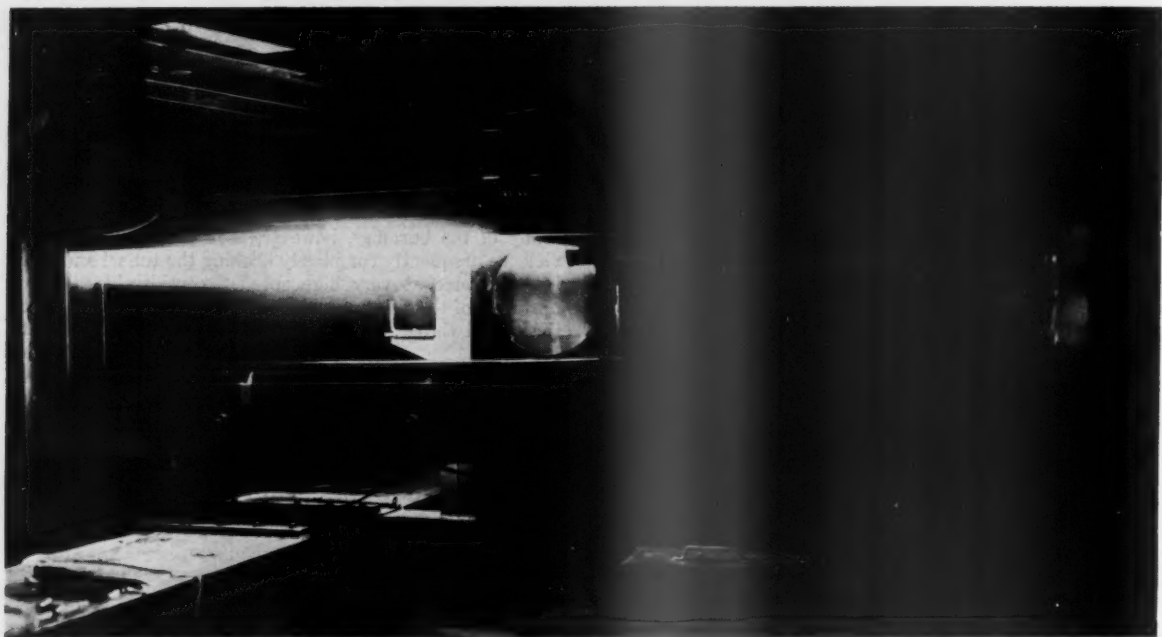


Fig. 5 Open shutter photograph of the combustion of aluminum borohydride in Mach 2 wind tunnel

capsule continued to burn for about 30 millsec more. The shock wave initially off the end of the capsule started moving upstream when combustion started, moving rapidly at first and then more slowly. Choking of the tunnel was virtually complete in about 8 millsec. Restoration of normal flow in the tunnel was quite slow. The normal shock did not return to the injector position until about 20 millsec after completion of the vigorous burning, and normal flow was not established in this section of the tunnel for an additional 20 millsec, at about the same time that the last driblets of fuel from the capsule had stopped burning. The violence and highly transient nature of these runs was due to the high momentary fuel concentration and precluded any sort of precise observation or measurement.

With the metal injector shown in Fig. 3, lower (of the order of 3 gm per sec) fuel flow rates were used than for the glass capsules. Successful steady-state burning of aluminum borohydride was achieved in the small tunnel at Mach numbers of 1.5, 2 and 3. Combustion at Mach 4 was not studied with this injector. A typical time exposure of the combustion is shown in Fig. 5. The fuel ignited at the spark plug, and the flame flashed back to the point of injection. Occasionally, the fuel ignited spontaneously at the point of injection. Fig. 6 shows single frames taken from high speed direct and Schlieren motion pictures of a typical aluminum borohydride flame. From the motion pictures, the flashback velocities with respect to the tunnel can be estimated. With aluminum borohydride, they were

usually in the range from several hundred to 3200 fps. If the stream through which the flame was propagating was flowing against the flame, the spatial flame velocities in the gas were, of course, much higher. Flame velocities of this magnitude are usually associated with detonation waves. The combustion region is, indeed, associated with a shock wave which can be seen in the Schlieren photograph of Fig. 6.

The static pressure rises associated with combustion along the top wall of the test section are presented in Fig. 7. The experimental points are average values taken from 16 runs. The curve goes through a maximum just behind the point of injection, falls off and goes through a minimum, and then rises again to a steady value. The forward pressure rise (shaded in Fig. 7) is unambiguously the result of combustion. However, the downstream rise undoubtedly is due both to some combustion in this region and to wind tunnel effects. These effects arise from the interaction of a shock wave with the subsonic portion of the boundary layer. The high pressure behind the shock wave compresses the boundary layer and is fed upstream through the subsonic portion of the boundary layer. The result is that the pressures exerted on the wall are higher than they would be in the absence of the shock wave interaction. In addition, the pressure gradient, which is now adverse, could be expected to induce the formation of a recirculation zone.

The shock wave does, indeed, interact with the hot zone. This is shown in Fig. 8 which is a composite artist's sketch and photograph of the test section. Because of these wind tunnel effects the pressure profile on the top wall (except for a small region near the fuel orifice) is more indicative of the internal pressures to be expected during combustion in a supersonic stream in a duct than it is of the pressure profile below a wing in free flight.

Aluminum borohydride-JP-4 fuel mixtures

Mixtures of aluminum borohydride containing 22, 41 and 59 per cent JP-4 fuel by weight were also studied. The 22- and 41-per cent JP-4 fuel mixtures were easily ignited, and burned well. With 59 per cent JP-4 fuel, two attempts to achieve ignition were not successful. Both attempts resulted in weak burning downstream of the spark plug.

Tandem injections of JP-4 and aluminum borohydride

Attempts at piloting a JP-4 flame with aluminum borohydride injected either upstream or downstream of the JP-4 were successful. The motion pictures and the behavior of the pressure instrumentation as well as visual observations showed that the JP-4 burned only within the aluminum borohydride flame zone and only as long as the borohydride flame was present. The JP-4 fuel was unable to sustain combustion by itself. When the JP-4 was injected upstream of the borohydride fuel, flame would not propagate upstream to the JP-4 fuel injection point.

Pentaborane

After some difficulty, pentaborane was also successfully burned at Mach 2. The lowest volumetric fuel flow rate with which pentaborane could be made to burn was about 1.4 times that for aluminum borohydride. The combustion was somewhat different (Fig. 9) from that for aluminum borohydride. The flame was much larger and penetrated more deeply down into the test section. The increased fuel flow coupled with the high heat of combustion of pentaborane gave a heat release rate for this fuel that was about twice that achieved with aluminum borohydride.

Other fuels

The following fuels were not suitable for burning at these Mach 2 tunnel conditions: Trimethylaluminum, diethyl-

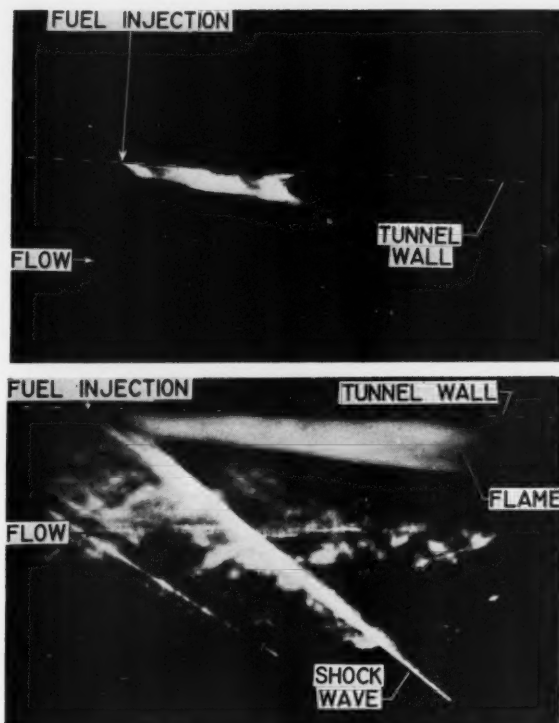


Fig. 6 Direct and Schlieren photographs of aluminum borohydride combustion using single fuel injection

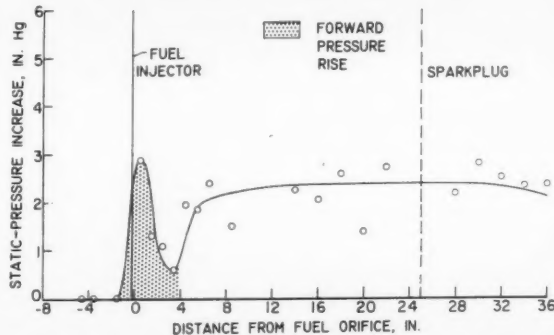


Fig. 7 Static pressure increase on top tunnel wall due to combustion of aluminum borohydride. Fuel orifice diameter, 0.0156 in.; pressure, 50 psig

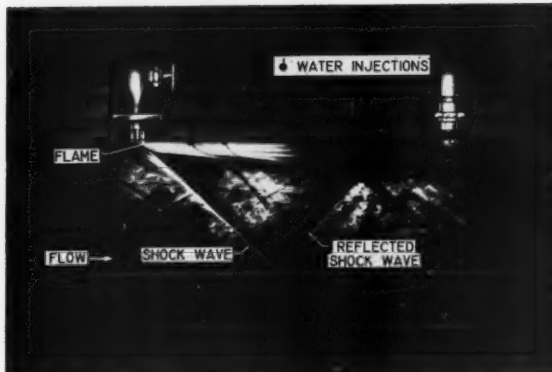


Fig. 8 Composite sketch-photograph of entire test section of wind tunnel showing combustion of aluminum borohydride and water streams injected in heated region of flow

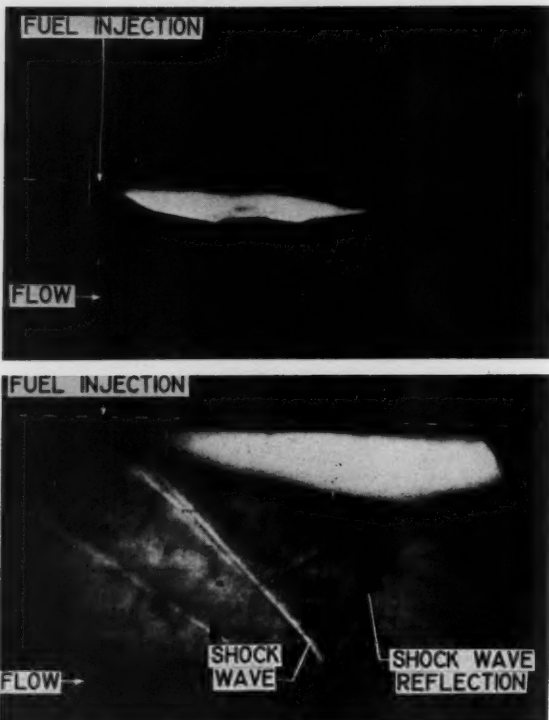


Fig. 9 Direct and Schlieren photographs of pentaborane combustion

aluminum hydride, trimethylborane, triethylborane, alkylboron hydrides and vinylsilane. Although the fuel flow rates were varied considerably, none of these fuels was capable of maintaining steady stable combustion. Occasionally unsteady combustion occurred behind the spark plug with a few of the alkylboron and alkylaluminum compounds. This consisted of intermittent flashes of flame associated with the sparking of the plug. These flashes were all in the vicinity of the spark plug or in the tunnel diffuser. It should be noted that in flowing from the test section to the diffuser, the fuel-air mixture would go through strong shock waves in the diffuser; the higher static temperature and pressure in this region is more conducive to ignition and combustion of the fuel.

Alkylaluminum compounds with water injection

Trimethylaluminum and diethylaluminum hydride exhibited some evidence of combustion at these Mach 2 tunnel conditions when water was injected upstream or downstream of the fuel injection point. Light was emitted, and a slight rise of static pressure was observed. Alkylaluminum compounds react explosively with water. Hence the observed chemical reaction was probably the hydrolysis of the fuel and possible oxidation of the by-products. The reaction flame occurred at the point of intermixing of the water and fuel sprays. The reaction was mild in comparison to that of aluminum borohydride burning in air.

Flow in the heated region

Water streams injected into the heated region permitted study of the gross nature of the flow field during combustion. Fig. 8, constructed from Schlieren pictures taken at various stations along the entire length of the wind tunnel shows these streams. The sketches emphasize the observations taken from the Schlieren motion pictures. The streams are more

or less vertical lines originating at the top wall of the tunnel. When water was injected through the small holes prior to combustion of the fuel, the streams of water adhered very closely to the tunnel wall and were atomized very near the orifices. When combustion began, the water streams flowed vertically down into the heated region; they extended to the boundary between this region and the main airstream before they were deflected into the airstream and atomized. This distance is approximately 4 in. from the top tunnel wall in the downstream nonluminous portion of the heated region. In the upstream luminous region the penetration of the water streams was not very deep. The streams near the point of fuel injection followed a parabolic path which suggested merely a thickening of the boundary layer. Examination of the motion pictures from which Fig. 8 was constructed reveals that the downstream water streams moved back and forth from the true vertical position, but their preferred orientation was in an upstream direction. This indicates that the flow in this region was continually reversing direction, and suggests the existence of large recirculation zones in the region of shock interaction with the heated flow. The absence of shock or Mach waves off the water streams, the deep penetration of the water columns and their upstream orientation also suggest that much of the flow in the heated zone downstream of the flame front is subsonic.

Application of Aluminum Borohydride Combustion to Aerodynamic Studies

Of all the fuels tested, aluminum borohydride was the most dependable and easiest to use in existing low temperature facilities. With it, the effect of combustion on the aerodynamic properties of the airstreams around several models was studied. In a 1×1 -ft supersonic wind tunnel, flat plates having chord (distance from leading to trailing edge) lengths of 13 and 25 in. were studied at a Mach number of 2.5. In the same tunnel, blunt based supersonic wings having 13- and 22-in. chords were studied at Mach numbers of 2.5 and 3.0. In addition several flat plates were studied in a large 10×10 -ft supersonic wind tunnel at Mach 2.4. In all of these investigations, the stagnation temperatures were of the order of 100 F, and the stagnation pressures were realistic only for relatively low Mach numbers at moderately high altitudes. In high speed flight, temperatures and pressures would be higher, and other fuels could be easily burned.

Typical Apparatus and Procedure

An example of the kind of research installation used in the aerodynamic studies is given in Fig. 10. This figure shows the installation of the 25-in. chord flat plate in the 1×1 -ft wind tunnel. This particular model was mounted at zero angle of attack, with the reference surface, adjacent to which combustion took place, near the centerline of the tunnel.

Fuel injection system

The fuel injector used in the small tunnel studies was coupled to a $\frac{1}{8}$ -in. copper tube connected to a fuel manifold inside the model. From the fuel manifold, three $\frac{1}{16}$ -in. tubes of approximately equal flow resistance were connected to three fuel orifices drilled in the reference surface. The fuel orifices were 0.016 in. in diameter and were located as shown in Fig. 10.

The injector was pressurized with dry helium through the upper valve to about 50 psig. Then the fuel lines below the lower valve of the injector were flushed by a continuous stream of low pressure helium (20 psig) which flowed out the three fuel orifices. The helium was turned off by a solenoid operated valve just before the lower valve of the fuel injector was opened by the drive motor. The fuel was injected through the three orifices for a 1- to 5-sec period until it was all

expelled from the injector. Following fuel injection, the injector and the lines were flushed with helium to remove the residual fuel.

Ignition system

The ignitor was a $\frac{1}{4}$ -in. rod which extended from the tunnel wall to within spark gap distance (of the order of $\frac{3}{16}$ in.) of the plate surface. The tip of the rod was placed so that it was in line with the fuel stream from the lower fuel orifice and was about $\frac{3}{8}$ to $\frac{1}{2}$ in. upstream of the blunt trailing edge of the model. The ignitor was connected to a 1-joule, repeating, capacitance-type power supply which provided a spark from the rod to the model surface five times per sec. With some of the models where the ignitor could interfere with combustion or flow, it was retracted immediately after ignition.

Results and Discussion

The detailed results of such aerodynamic studies are reported in a series of NACA research memoranda (2,10,11,12). Some pertinent observations made during the course of these studies may be of interest.

Ignition and propagation

Either flush mounted spark plugs, which caused no disturbance to the stream, or spark electrodes, which sparked through the model to ground, could be used with equal success. The mixture usually ignited at the spark, quickly flashed back to the point of fuel injection, and burned steadily. However, two interesting points should be made concerning the location of the spark.

The flame would not propagate upstream unless the mixture through which it was propagating was part of a boundary layer in contact with a solid surface. For example, in the early flat plate studies, the spark plug was placed 16 in. downstream of the trailing edge of the flat plate in the stream tube into which fuel was being added. Ignition was achieved, but the flame would not propagate back to the point of injection on the model. Instead, it burned downstream, being held by the spark plug itself or by instrument rakes in the downstream portion of the tunnel.

The flame sometimes would not propagate back to the point of fuel injection over curved surfaces. Thus, with the wing models, positioning of the spark electrode near the trailing edge of the model sometimes resulted in flames which stabilized themselves 2 or 3 in. upstream of the trailing edge or occasionally in the wake just downstream of the base. This problem was easily alleviated by simply placing a retractable spark plug at the midpoint of the chord. With the spark thus located, achieving flashback to the point of fuel injection presented no problems.

Examples of pressure profiles obtained

Examples of the kinds of pressure profiles which are obtained in such studies are shown in Fig. 11. In this figure is plotted the change in pressure coefficient resulting from combustion, as a function of the distance downstream from the point of fuel injection, for the various models tested in the 1×1 -ft tunnel. These are compared with a similar plot of the data for a 25-in. chord flat plate model in a very large 10×10 -ft wind tunnel. The change in pressure coefficient is the local static pressure change due to combustion divided by the dynamic pressure of the undisturbed stream. The ordinate is therefore a measure of the pressure rise on the airfoil caused by combustion in the adjacent stream.

The profiles are qualitatively quite similar in their upstream regions. There is a rather sharp pressure rise in the vicinity of the fuel injection region, which reaches a maximum a few inches downstream of the point of injection; the pressure

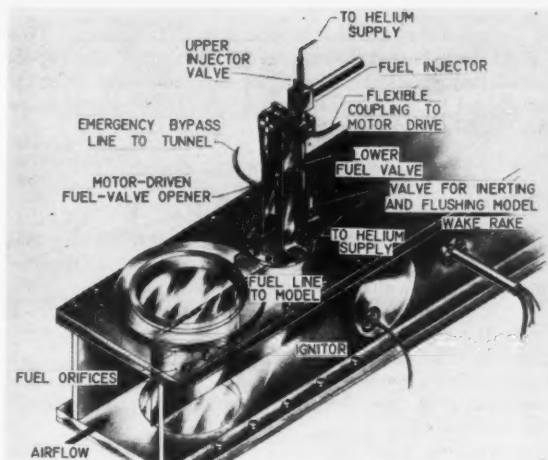


Fig. 10 Flat plate model installation in 1×1 -ft test section

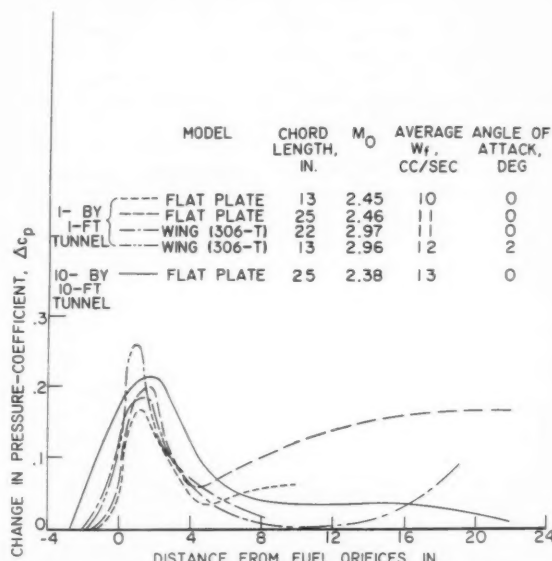


Fig. 11 Comparison of centerline chordwise profiles of change in local pressure coefficient along lower surface due to combustion of aluminum borohydride in airstream below various models

rise gradually decreases in the downstream direction. This is the main characteristic of the pressure rise profile. The 13-in. wing, at Mach 2.96, clearly shows this characteristic profile. The second pressure rise on the longer chord models is caused by reflection of the flame and leading edge shock waves from the tunnel walls back into the downstream portions of the flame zone where they interact with the heated flow, causing a subsonic recirculation region and further combustion of unburned fuel with air entering this region. Fig. 11 shows that, with the 25-in. flat plate in the large 10×10 -ft tunnel, as with the short models in the 1×1 -ft tunnel, there is no large second pressure rise region over the downstream portion of the model. In the large tunnel the wall was over 6 ft from the flat plate surface. Therefore, the point where the reflected oblique shock wave impinged on the heated wake was so far downstream of the base of the model that there was

no disturbance of the heated zone next to the model. Thus Fig. 11 suggests that, because of the "fattening" effect of the heated flow about the model, the ratio of tunnel to model size should be much larger than is usually considered necessary to avoid tunnel effects.

Conclusion

A study of the combustion of various highly reactive fuels injected through the top wall of a 3.84×10 -in. wind tunnel into a supersonic airstream disclosed that:

1 Aluminum borohydride, pentaborane and mixtures of up to 41 per cent JP-4 fuel blended with aluminum borohydride could be burned in a Mach 2 airstream under the conditions of this experiment without the use of a flameholder. Combustion of these fuels gave associated pressure rises in the reaction zone.

2 Tandem aluminum borohydride and JP-4 injections gave high heat release rates, which tended to choke the supersonic flow in tunnels of this size.

3 JP-4 fuel could be burned in a Mach 2 airstream under the conditions of this experiment only as long as a piloting flame of aluminum borohydride was present.

4 Trimethylaluminum and diethylaluminum hydride could not be ignited at Mach 2 tunnel conditions. However, when water was simultaneously sprayed into the tunnel, there was a luminous reaction which produced heat.

5 Trimethylborane, triethylborane, alkylboron hydrides and vinylsilane could not be ignited or burned in the tunnel test section. These fuels frequently did ignite in the tunnel diffuser; therefore, they might be combustible under conditions where the recovery temperatures would be higher than those of the present study.

6 Studies in which the heated region was probed by water injections, indicated that the flow downstream of the flame front was subsonic and recirculating.

The combustion techniques developed in the 3.84×10 -in. tunnel were applied to aerodynamic studies of the effect of heat addition by combustion of aluminum borohydride on supersonic airstreams. The detailed aerodynamic results have been reported elsewhere in the literature. The follow-

ing observations should prove helpful to those wishing to do further aerodynamic studies of this nature:

1 The presence of a boundary layer is extremely helpful, if not essential, in achieving flashback and stable combustion even with the most highly reactive fuel of this investigation, aluminum borohydride.

2 The technique is well suited for aerodynamic studies of external combustion. However, the test facility must be large enough, or the model short enough so that disturbances which reflect from the tunnel walls intersect with the hot gases well downstream of the region of aerodynamic interest.

References

1 Hicks, B. L., Montgomery, D. J. and Wasserman, R. H., "On the One-Dimensional Theory of Steady Compressible Fluid Flow in Ducts with Friction and Heat Addition," *J. Appl. Phys.*, vol. 18, no. 10, Oct. 1947, pp. 891-903.

2 Pinkel, I. I. and Serafini, J. S., "Graphical Method for Obtaining Flow Field in Two-Dimensional Supersonic Stream to Which Heat is Added," NACA TN 2206, 1950.

3 Shapiro, A. H. and Hawthorne, W. R., "The Mechanics and Thermodynamics of Steady One-Dimensional Gas Flow," *J. Appl. Mech.*, vol. 1, no. 4, Dec. 1947, pp. A317-A336.

4 Tsien, H. S. and Berloch, M., "Heat Source in a Uniform Flow," *J. Aero. Sci.*, vol. 16, no. 12, Dec. 1949, p. 756.

5 Fletcher, E. A., Dorsch, R. G. and Gerstein, M., "Combustion of Aluminum Borohydride in a Supersonic Wind Tunnel," NACA RM E55D07a, 1955.

6 Dorsch, R. G., Serafini, J. S. and Fletcher, E. A., "A Preliminary Investigation of Static-Pressure Changes Associated with Combustion of Aluminum Borohydride in a Supersonic Wind Tunnel," NACA RM E55F07, 1955.

7 Nichols, J. A., Dabora, E. K. and Gealer, R. L., "Studies in Connection with Stabilized Gaseous Detonation Waves," in "Sixth Symposium (Int.) on Combustion," Butterworths Sci. Pub., London, p. 766.

8 Gross, R. A., "Research on Supersonic Combustion," *ARS JOURNAL*, vol. 29, no. 1, Jan. 1959, pp. 63-64.

9 Allen, H. Jr. and Fletcher, E. A., "Combustion of Various Highly Reactive Fuels in a 3.84×10 -Inch Mach 2 Wind Tunnel," NASA Memo 1-15-59E, 1959.

10 Dorsch, R. G., Serafini, J. S. and Fletcher, E. A., "Exploration Investigation of the Aerodynamic Effects of External Combustion of Aluminum Borohydride in Airstream Adjacent to Flat Plate in Mach 2.46 Tunnel," NACA RM E57E16, 1957.

11 Serafini, J. S., Dorsch, R. G. and Fletcher, E. A., "Exploration Investigation of Static- and Base-Pressure Increases Resulting from Combustion of Aluminum Borohydride Adjacent to Body of Revolution in Supersonic Wind Tunnel," NACA RM E57E15, 1957.

12 Dorsch, R. G., Serafini, J. S., Fletcher, E. A. and Pinkel, I. I., "Experimental Investigation of Aerodynamic Effects of External Combustion in Airstream Below Two-Dimensional Supersonic Wing at Mach 2.5 and 3.0," NASA Memo 1-11-59E, 1959.

Thermal Control of the Explorer Satellites

GERHARD HELLER¹

Army Ballistic Missile Agency
Redstone Arsenal, Ala.

Thermal control of the Explorer satellites is discussed. The theoretical studies that were made prior to the launching of these satellites are described, and examples of relationships are presented in graphs. The lower limit of the instrument temperature was zero deg C (determined by the efficiency of the chemical batteries). The upper limit was specified as 65 C (based on long-time temperature limits of transistors in the electronic package). This paper will relate some of the studies, describe the measuring results of telemetered temperatures and evaluate expected and obtained data.

IT IS generally assumed that the problems of thermal control of satellites are solved. Explorer I had inside a comfortable temperature of 20 C, maintained over an operating

Presented at the ARS Semi-Annual Meeting, San Diego, Calif., June 8-11, 1959.

¹ Deputy Director, Research Projects Laboratory, Development Operations Division.

period of 3 months. The temperature variations around this mean value were not more than ± 20 C; i.e., the climate on board the satellite had fewer variations than the temperature, for instance, in Huntsville, Ala. However, the thermal problems of satellites require a number of studies and prototype testing prior to launching.

Control of Explorer I was maintained between 0 and 40 C

during 90 days of operation; Explorer III was maintained between 0 and 40°C up to 43 days after launching. Then the transmitter ceased to operate; this was attributed to freezing of the batteries.

Explorer IV was controlled between 19 and 55°C during the operational time of 60 days.

Parameter Study of Thermal Problems

The temperature of a satellite is dependent on:

- 1 Orbital characteristics.
- 2 Surface properties, especially emissivities, of skin and of internal surfaces.
- 3 The attitude of the momentum vector of a spinning satellite to the direction of the sun.
- 4 The attitude of the spin axis to the direction of the sun.
- 5 The attitude of the satellite and attitude of the momentum vector to the center of Earth.
- 6 Heat capacity of skin and of instruments.
- 7 Conductive and radiative heat transfer between skin and instruments, and between parts of the skin. Convective heat transfer was excluded for the Explorers by letting the air escape through gaps.
- 8 Internal heat release of instruments.
- 9 Aerodynamic heating for satellites with a perigee of 200 miles or lower.
- 10 Environmental conditions, such as solar constant, albedo, Earth radiation.

The Explorer satellites are spin stabilized; therefore, temperatures on individual points of the surface equalize in any plane perpendicular to the spin axis.

Fig. 1 shows a cutaway of Explorer I. Explorer I data and instrumentation have been published elsewhere, e.g., in a previous paper by the author (1).² Therefore, only points that affect temperatures are described here. The satellite is shaped like a pencil. The empty fourth stage motor stays attached, but it is thermally and electrically insulated from the cylinder. The wire antennas were used only in Explorer I.

The parameter study was performed prior to Explorer I, and, to some extent, prior to each Explorer firing. Each of the parameters was treated as an independent variable and varied in a range wide enough to cover variations of the missile characteristics and their effect on the injection data, firing date and time, satellite properties and environmental conditions. The thermodynamic and celestial mechanics equations were programmed on an IBM 704 computer. Each parameter was varied independently by choosing three, four or five different values.

An important factor that influences the satellite temperatures is the time in sunlight. For the Explorer-type satellite, this value may fluctuate between 63 and 100 per cent. According to Krause (2), the shadow angle is given by

$$\sin X = \sin \beta / \cos \delta \quad [1]$$

where

- X = angle between 0600–1800 hours line and crossover from shadow to sunlight or from sunlight to shadow
- β = angle at center of Earth between satellite and tangent to Earth
- δ = angular distance of sun from orbital plane

The following approach was taken to solve the temperature problem with so many parameters, and to arrive at design criteria.

An analysis was made of the crossover points of the satellite in and out of the sunlight for each revolution as a function of the orbital characteristics and the position of the sun. The angle δ is a function of the orbital parameter and the

* Numbers in parentheses indicate References at end of paper.

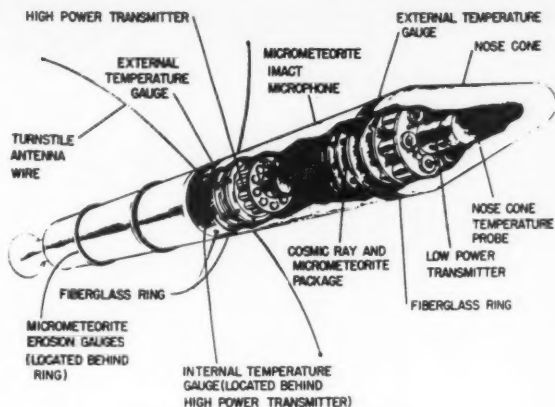


Fig. 1 Schematic of Explorer I

sun's position. Parameters used to describe the orbit were

- i = inclination of orbit to Equator
- Ω = right ascension of ascending node measured from spring point
- ω = argument of perigee
- e = eccentricity of orbit
- R_p = radius vector at perigee
- ϕ = time angle measured in orbital plane from east direction to perigee

The position of the satellite within this orbit is given by the true anomaly ν .

The position of the sun enters into the computation by its longitude L_0 measured along the ecliptic. A mean motion of the sun in the ecliptic plane was assumed. A check was made for some cases, using the true position from the Ephemeris and Nautical Almanac, and the difference was found to be negligible.

The quantities entering into Equation [1] can be expressed by the parameters above by coordinate transformation between orbital plane and ecliptic plane to the equatorial coordinate system that is commonly used for orbit parameters.

For orbiting during an extended period of time, it must be considered that the orbital characteristics change. First-order perturbation theory as developed by Krause (3) and by Cunningham (4) has been applied to compute these changes. Only secular changes have been considered, because the small periodic changes have only negligible effect on the temperature problem. For this purpose, the time dependent angles Ω , ϕ and α have been derived as functions of the hour of launching H_0 and the day of launching D_0 . The changes with respect to time are then expressed by the linearized equations

$$\Omega = \Omega_0 + k_1 (D - D_0) \quad [2]$$

$$\phi = \phi_0 + k_2 (D - D_0) \quad [3]$$

$$\alpha = \alpha_0 + k_3 (D - D_0) \quad [4]$$

where

k_1, k_2, k_3 = constants

$D - D_0$ = number of days after launching

For the conditions of Explorer I, the coefficients are

$k_1 = -4.35$ deg per day (rotation of orbital plane)

$k_2 = 6.49$ deg per day (rotation of line of apsides)

$k_3 = 0.9856$ deg per day (mean motion of sun)

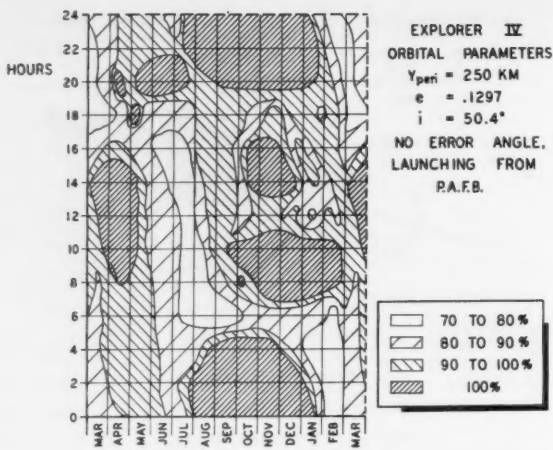


Fig. 2 Time in sunlight for a satellite as a function of day and hour of firing. Maximum values during first 60 days of orbiting

From the crossover points of the satellite in and out of the sunlight, the time can be computed by introduction of the eccentric anomaly E and the use of Kepler's equation

$$T_x = \frac{T_1 - T_2}{\tau} = \frac{1}{2\pi} [(E_1 - e \sin E_1) - (E_2 - e \sin E_2)] \quad [5]$$

where

T_x = ratio of time in sunlight to period

τ = period of satellite

T_1 = time when satellite enters sunlight

T_2 = time when satellite enters shadow

e = eccentricity

Attitude angle of satellite axis with respect to the sun is determined by the original coordinates with respect to the horizon coordinate system. In this system, the altitude angle is zero and the angular direction is given by the Earth-fixed azimuth. The initial attitude can be computed from these coordinates and the position angles of the sun as a function of the day D_0 and hour H_0 of launching.

Changes of the attitude angle to the sun with time are dependent on the movements of the sun with respect to the original launching plane and not on other time variable changes of this orbit. It is assumed that the initial momentum vector of the spinning satellite is maintained in space. Exchange of angular momentum from the longitudinal axis to an axis of greatest moment of inertia has been considered. However, this initial concept has been refined on the basis of results obtained from the Explorer measurements.

The surface temperatures of the satellite depend on the emissivities of the skin with respect to short wave solar radiation and infrared radiation from Earth and from satellite skin, and on the coefficients of solar radiation (solar constant), albedo and Earth radiation.

The following two simultaneous differential equations have to be solved (1,5,6)

$$A_1 \alpha S D_1 + A_2 \alpha B S D_2 + A_3 \epsilon E S - A_4 \sigma \epsilon T_s^4 - C_b \dot{T}_s - C_e \dot{T}_s + Q = 0 \quad [6]$$

$$C_e \dot{T}_s = C_r (T_s - T_i) + C_s \sigma (T_s^4 - T_i^4) \quad [7]$$

where

A_1 = projected area with respect to sun direction

α = absorptivity for solar radiation

S = solar constant

D_1 = step function ($D_1 = 1$ for sunlight, $D_1 = 0$ for shadow)

A_2 = effective area of satellite with respect to albedo

D_2 = step function ($D_2 = 1$ for orbit in hemisphere $\pm 90^\circ$ from

sun direction, $D_2 = 0$ for orbit in hemisphere opposite sun direction)

B = albedo of Earth

A_3 = effective area of satellite with respect to Earth radiation

ϵ = emissivity with respect to infrared radiation

E = ratio of infrared heat flux from Earth to solar constant

A_4 = total surface area of satellite

σ = Boltzmann constant

T_s = skin temperature

C_b = heat capacity of skin

\dot{T}_s = rate of temperature change of skin

C_e = heat capacity of instruments

T_i = instrument temperature

\dot{T}_i = rate of temperature change of instruments

Q = heat release of instruments

C_7 = heat transfer coefficient by conduction

C_8 = heat transfer coefficient by radiation

The areas are obtained from

$$A_1 = A_1^\circ \sin \gamma \quad [8]$$

$$A_2 = A_1^\circ f(\zeta) \left(1 - \sqrt{\frac{2R_0 H + H^2}{R_0^2 + 2R_0 H + H^2}} \right) \cos \theta \quad [9]$$

$$A_3 = A_1^\circ f(\zeta) \left(1 - \sqrt{\frac{2R_0 H + H^2}{R_0^2 + 2R_0 H + H^2}} \right) \quad [10]$$

where

A_1° = maximum area of cylinder as seen from side

γ = attitude angle to sun

$f(\zeta)$ = function of attitude angle ζ of satellite axis to radius vector to center of Earth. (It was approximated by a five-power polynomial of $\cos \zeta$)

R_0 = radius of Earth at Equator

H = altitude of satellite

θ = angle of radius vector and direction to sun

The thermal design is based on thermal insulation between skin and instrument package. The skin temperature can fluctuate in a wide range during each sunlight and shadow cycle. The instrument temperature is affected very little by this cycle. It is mainly dependent on long-time changes of time in sunlight, attitude to sun and Earth, long-time changes of surface emissivity and changes of the environmental conditions.

In order to eliminate, as far as possible, changes of surface emissivities by impact of micrometeorites and other environmental conditions whose nature and influence is still to be determined, surfaces were selected that are insensitive to such effects. The selection for Explorers I and III was sandblasted stainless steel, and 25 per cent of the area was covered by stripes of aluminum oxide known under the trade name of Rokide A. Explorer IV was sandblasted stainless steel only.

The discussion of the parameter study up to now has been made under the assumption that all parameters are variables. However, if the thermal design has been determined on the basis of the analysis, all on-board parameters become fixed. In further analysis, it was assumed that the thermal properties of the satellite do not change during its useful operating time of 2 to 3 months. At this time, usually, an additional variable becomes fixed: The date of the firing.

The following parameters remain variables: Environmental conditions, orbital characteristics at the injection point of the satellite into orbit, hour of satellite launching. The environmental conditions are subject to changes that are not completely predictable and will be investigated in future satellites. For the solar "constant," a variation of ± 3.5 per cent was assumed. Albedo was varied between 24 and 54 per cent and the ratio of Earth radiation to solar constant between 15.9 and 19.3 per cent. Change of orbital characteristics at the injection point is due to dispersion of

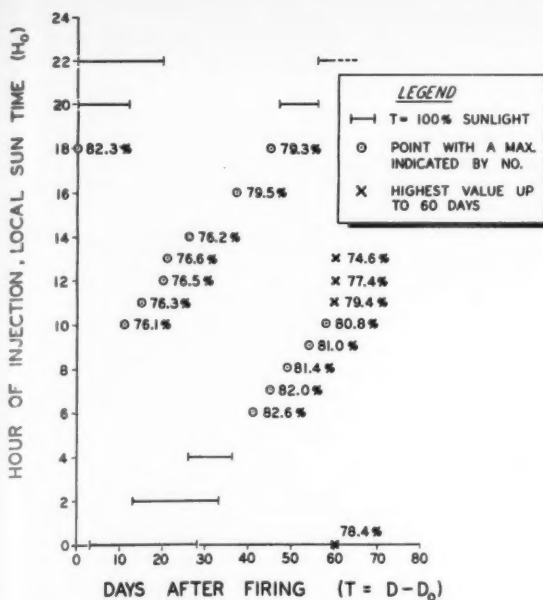


Fig. 3 Per cent time in sunlight (T_x) of Explorer IV vs. hour of firing and days after firing

booster and upper stages. A 2σ variation of all these parameters was assumed. The main influence was due to dispersions of the directions and the magnitude of the velocity vector. Variations of the injection values and of the environmental value determine upper and lower limits of temperatures.

The hour of the satellite launching can influence the initial plane of the satellite by 360 deg and the attitude of the satellite axis in space in a wide range.

The selection of the firing time for all Explorers has been used as a means to maintain temperature control. Explorers I and IV had a time in sunlight between 65 and 80 per cent during their operating time.

Results of the Parameter Studies

I will not describe all details of the parameter studies, especially since some of the results have already been published (1,7). Therefore, it will suffice to show the relationships in a few graphs and a table.

The time in sunlight was computed for orbital characteristics of Explorer IV as a function of day of firing D_0 and hour of firing H_0 . The 704 computer program was run for a simulated orbiting time of 60 days for each combination of D_0 and H_0 . The maximum values obtained at any point during this time are plotted in Fig. 2 as a function of D_0 and H_0 . The percentage time in sunlight is used as the parameter-like altitude lines on maps. For the selection of a firing time, variations of the initial orbital conditions had to be analyzed. The following effects were found. The areas of high time in sunlight values increase with the increase of: The eccentricity of the orbit; the injection altitude; inclination angle; and error angle in pitch, both plus and minus, and in yaw to the left for firing from Patrick Air Force Base.

A better understanding of the maxima of time in sunlight T_x can be obtained from Fig. 3 which shows T_x for Explorer IV. The day of firing is no longer a variable but fixed on July 26, 1958. The maxima of T_x are plotted as a function of the hour of firing and the days after firing. The maxima shift with the hour of firing, with a constant slope which is given by the daily change of the ascending node and the daily change due to the relative motion of the sun. The magnitude and extension of the maxima are determined by a combination of

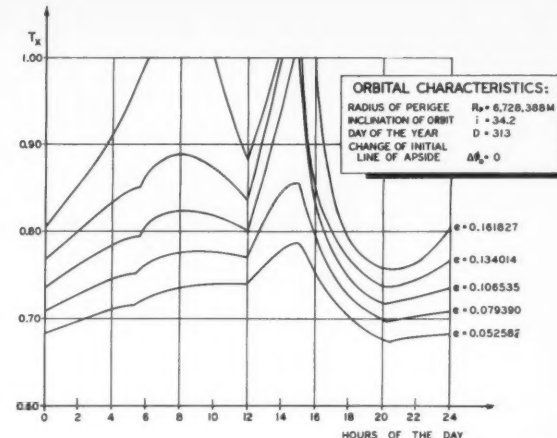


Fig. 4 Time in sunlight (T_x) vs. hour of the day of launching for Explorer I. Maximum values during first 60 days of orbiting

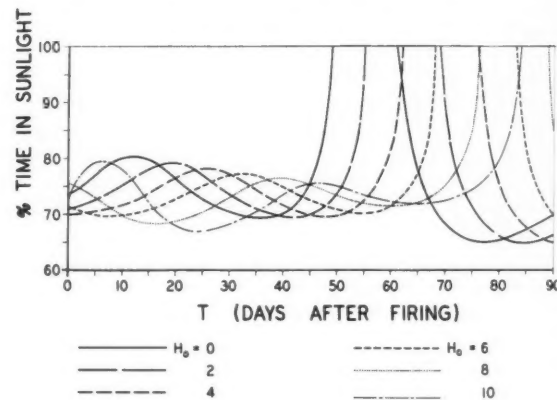


Fig. 5 Time in sunlight vs. days after firing Explorer V

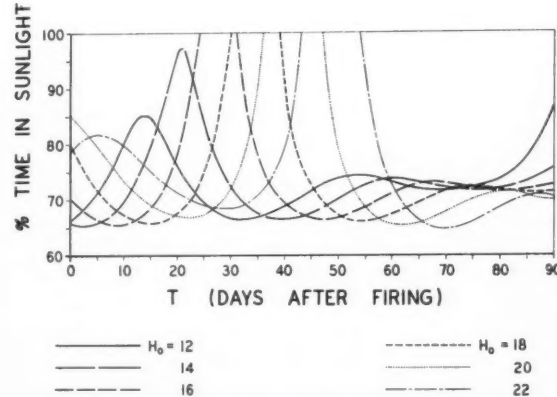


Fig. 6 Time in sunlight vs. days after firing Explorer V

these two factors and the progression of the line of apsides. This effect does not exist for circular orbits; for elliptical orbits, it increases strongly with the eccentricity.

The effect of eccentricity is shown in Fig. 4, which is a plot of the maximum time in sunlight vs. the hour of firing for Explorer I. In this case, the program was also run for a simulated orbiting time of 60 days. Time in sunlight T_x vs. the days $D - D_0$ after launching is shown in Figs. 5 and 6 for Explorer V. Fig. 5 shows the variation of T_x for the hours H_0 0–10 as parameters, and Fig. 6 shows the same for the hours 12 to 22.

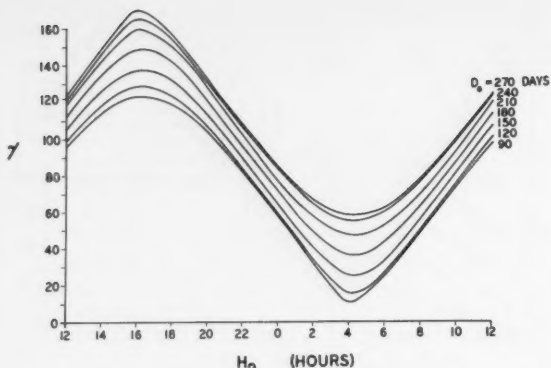


Fig. 7 Attitude angle (γ) of Explorer IV payload to sun

Table 1 Linearized influence parameters for Explorers I and III

Parameter	Nominal value	Variation	Change of instrument temp., C
albedo	0.34	± 0.20	± 5
ratio of Earth radiation to solar constant	0.175	± 0.0175	± 8
solar constant	2 cal/min-cm ²	± 0.07	$\pm 2\frac{1}{2}$
time in sunlight	0.73	± 0.1	± 10
projected area to sun	90 per cent of max. area	± 10 per cent	± 8
altitude of satellite	1300 km	± 100 km	∓ 1
ratio of emissivities	1.4	0.1	5

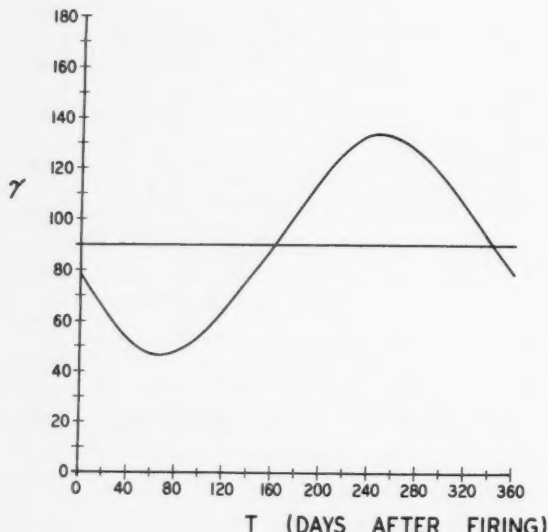


Fig. 8 Attitude angle (γ) vs. days after firing (T) for Explorer IV

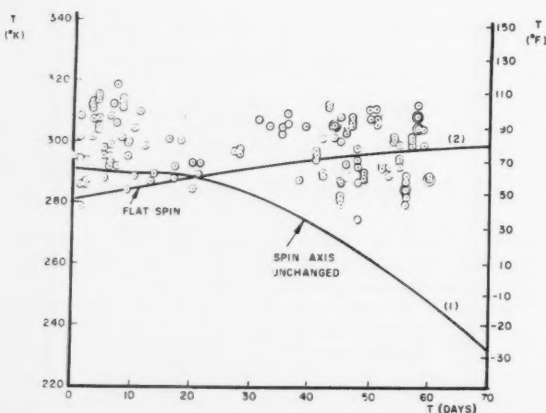


Fig. 9 Temperature of Explorer I. Nose cone instrument temperature

The effect of variations of several parameters applicable to Explorers I and III is shown in Table 1 in the form of linearized influence parameters. The expected temperature changes are quite large. A more detailed analysis and evaluation of Explorer results showed that variations of albedo, Earth radiation and satellite altitude affect only the skin temperature fluctuation, but had little effect on the mean temperature. A better analysis of this problem will be possible after results of the radiation balance are available from future satellites. Variations of solar constant are mainly due to the variable distance of Earth from the sun. For an operating time of 60 days, the variations are negligible.

This leaves as the main influencing parameters the time in sunlight and the projected area to the sun. Variations of the ratio of emissivities can have quite a decisive effect on the temperatures, and overshadow other effects. However, with the precautions taken to select surfaces insensitive to changes, it is reasonable to assume that the ratio of emissivities stayed constant.

Attitude of Satellite

The initial attitude of the satellite to the direction of the sun is easily determined from the direction of the velocity vector at injection into orbit and the known direction of the sun. This holds true for a spin stabilized satellite whose spin axis is aligned horizontally to Earth at the injection point and whose angular dispersion is negligible. These conditions were fairly well satisfied for Explorers I, III and IV at the time of injection. Fig. 7 shows the initial attitude angle to the sun for Explorer IV as a function of the day D_0 and the hour of firing H_0 . This initial attitude angle will change due to the relative motion of the sun, as shown in Fig. 8, as a function of the number of days after the firing. For the pencil-shaped Explorer satellites, the spin axis is not stable, since it has the smallest moment of inertia. The initial momentum vector was considered unchanged in space (pointing toward the same fixed star). However, an exchange of momentum from the minor axis of inertia to a major axis of inertia had to be considered in the analysis. It can be shown that such a momentum transfer is possible, if the energy equation can be satisfied. Since the spin around a major axis of inertia means a reduction of the spin rate, this mode of rotation corresponds to a lower energy level. Therefore, the transfer of momentum takes place if rotational energy is dissipated by internal friction. It was assumed prior to Explorer I that this transfer takes place during the active lifetime of the satellite instrumentation. Fig. 9 shows theoretical satellite temperatures of Explorer I for the two extreme cases: 1 Spin axis unchanged around longitudinal axis of the satellite; and 2 spin around the initial axis with

the satellite aligned perpendicular to this axis (flat spin). The graph shows that temperatures in case 1 start out with a comfortable 295 K and stay above 273 K for 30 days, but then drop rapidly below the lower operating limit of 273 K. As the temperature measurements obtained by telemetry show, this did not happen, but all measuring points shown in Fig. 9 follow the curve for case 2 after a few days of orbiting. From an analysis of the antenna patterns, it was determined that the transfer in Explorer I had occurred during the first revolutions. This is the first case in which temperature measurements were used to determine the behavior of the satellite in space. Curve 2 of the flat spin is shown as an extreme case. The actual attitude and mode of spin is between case 1 and case 2. Also, a random tumbling causes the temperature to equalize at 295 K. To distinguish between case 2 and a random tumbling, a higher accuracy was needed. Further analysis showed that due to the internal damping, the flat spin was reached in all cases. In Explorers III and IV, it took about 10 days. These satellites did not have the flexible antenna wires. The dissipation of energy took much longer. The cause for this dissipation is assumed to be due to inelastic flexing and damped vibrations inside the satellite. External forces on the satellite to be considered are magnetic forces and forces due to interaction with the atmosphere. Magnetic damping was found to be of minor influence. However, interaction with the atmosphere during each perigee pass means a transfer of momentum which causes a change of the momentum vector in space. The long-time vector sum of changes can have a decisive effect on the thermal design and was, therefore, considered for the basic design philosophy of Explorer IV.

Thermal Coefficients and Thermal Tests

The thermal design of the Explorers was based on the following concepts: The control is passive; i.e., no variable surfaces or heat switches are applied; and the instrument package is insulated from the skin of the satellite to minimize short-time fluctuation during one revolution.

The coefficients in Equations [6 and 7] have to be known. The Explorers consisted of two parts, the cylinder and the cone, separated by insulation. The surface properties were adjusted so that the average temperatures in both parts were about the same. However, if the insulation is too good, the internal heat release will cause the package to overheat. Without insulation, the instruments would take part in the strong temperature variations of the skin.

A prototype testing program was carried out to determine the soundness of the thermal concept and to measure the coefficients entering into Equations [6 and 7].

Tests were performed by applying as sudden a temperature rise as possible (step function), and to measure the rise of the inside temperatures at various places, such as the transmitter, batteries, structure. Fig. 10 shows a typical test run for Explorer IV.

The temperature range a satellite of the Explorer type might assume without thermal design is between 200 and 380 K, as shown in a previous paper (1). This wide range applies for a constant value of the ratio of emissivities α/ϵ of 1.5. For variable α/ϵ the range would increase.

Results of Temperature Measurements

Fig. 9 shows average daily temperatures obtained by telemetry from Explorer I. The relation between the mode of the spin and the measured temperatures has already been discussed. Fig. 11 shows the temperature changes as expected during one revolution of Explorer I inside the instrument package and on the satellite skin. The dotted line shows the mean of measured values during the first 10 days of orbiting. The dip in the skin temperature during the sunlit portion occurs when the satellite reaches its apogee.

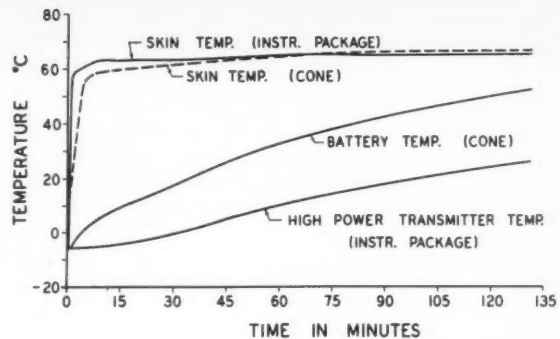


Fig. 10 Thermal test with prototype of Explorer IV

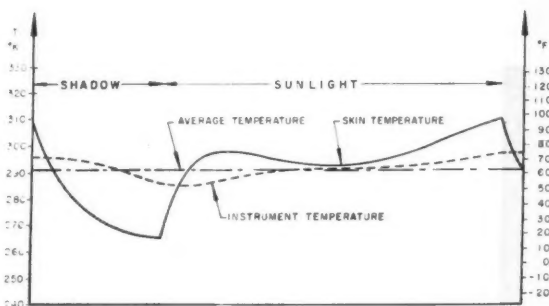


Fig. 11 Temperature of Explorer I during one sunlight and shadow cycle

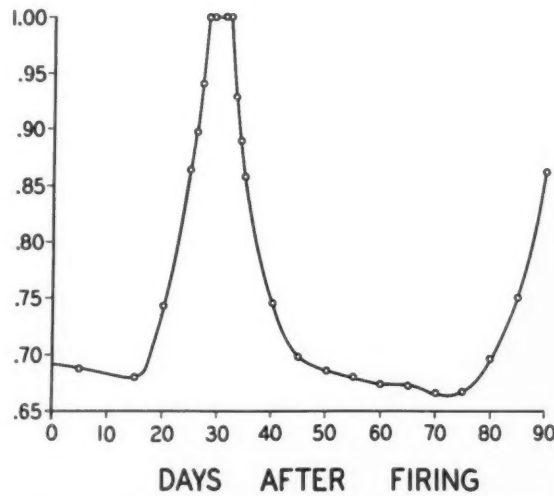


Fig. 12 Explorer III, per cent time in sunlight vs. days after firing

Explorer III is an example of a satellite that was allowed to have 100 per cent sunlight during 4 days of its operating time. Fig. 12 shows the time in sunlight vs. days after firing. The maximum temperature measured was 40°C 36 days after launch. Fig. 13 shows the theoretical temperature computed with the following assumptions for the satellite attitude:

0-10 days, spin axis unchanged.

After 10 days, flat spin.

Upper curve, momentum vector at zero angle to sun vector.

Lower curve, momentum vector at 90 deg to sun vector.

Fig. 14 shows the average of daily measurements and a third-order least square fit. Reception of data ceased after 43 days of operation, although the batteries were set up for 90 days. Signals were received twice at irregular intervals on the 62nd and 71st days. A number of theories have been offered to explain this. I would like to add one that seems plausible to me, although I cannot prove it by measurements.

After 43 days, the temperatures dropped below zero deg C. This caused the batteries to freeze, and no more signals were

received. During short intervals later on, the temperature rose above freezing, reviving the batteries and causing the transmitter to operate again. These later signals were too weak to enable telemetry evaluation. The temperatures dropping below zero prevented the reception of telemetry data to prove it.

Fig. 15 shows skin temperature and instrument temperature for a typical case of one daylight and night cycle of Explorer IV. Time in sunlight is 75 per cent. The apogee occurs during the shadow period. The instrument temperature variations are ± 5 deg, whereas the skin temperature varies between 255 and 330 K. Temperatures were determined from variations of the subcarrier oscillator frequencies. The temperature dependency of the oscillators was calibrated by Ludwig of the State University of Iowa prior to the launching. Fig. 16 shows the results of this temperature determination during the operating lifetime of 55 days. Two of the switching frequencies of channel 3 of the Explorer IV payload were used. Results of both are consistent, one frequency level always yielding higher values. Data were taken at the ABMA experimental tracking station at Huntsville, Ala. Measurements from this station were very good, and had almost no scatter. Measurements from other IGY stations confirmed the general trend of the measurements. As a most likely value, the arithmetic mean for each day has been used for the evaluation. The maximum temperature measured was 55 C, and the minimum temperature was 19 C. The overall average was near the design value of 39 C. As Fig. 17 shows, parameters of Explorer IV were chosen so that the time in sunlight was subject to small changes only during 60 days. The strong variations of temperatures were hard to reconcile with this smooth sunlight curve. The projected area as exposed to the sun is shown in Fig. 18 for the two extreme cases: 1 Spin about the original longitudinal axis; and 2 flat spin maintaining the original momentum vector. A transition from case 1 to case 2 can be expected within the first 5 to 10 days. The drop of the measured temperature from an initial value of 40 to 30 C seems to be connected with this changeover, as was observed in Explorer I. Fig. 19 shows a superposition of measured temperatures and theoretical temperatures, computed for a series of exposed area ratios. The minimum area for a flat spin, with the sun in a plane perpendicular to the momentum vector, is an average of $2/\pi$ or 63 per cent. Fig. 19 shows that the measured temperatures fit very well into this grid of theoretical temperatures. The point where an area of 100 per cent is exceeded corresponds to a temperature difference of 4 C. This is well within the accuracy, considering variations due to measuring error, variations of emissivity,

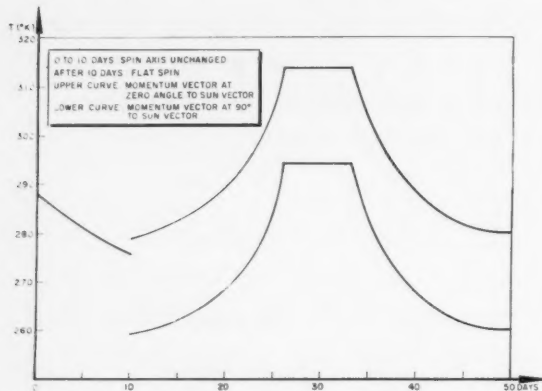


Fig. 13 Explorer III, theoretical mean instrument temperature

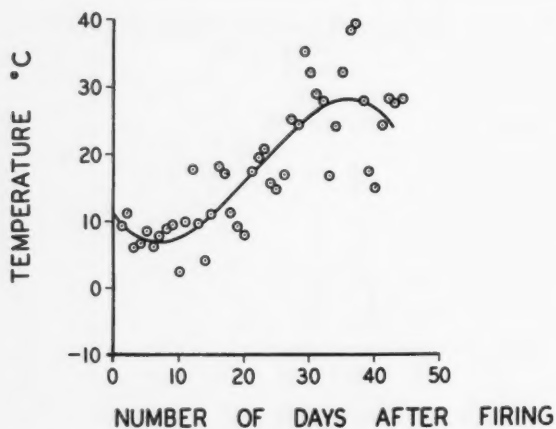


Fig. 14 Least square fit for Explorer III. Measured temperatures

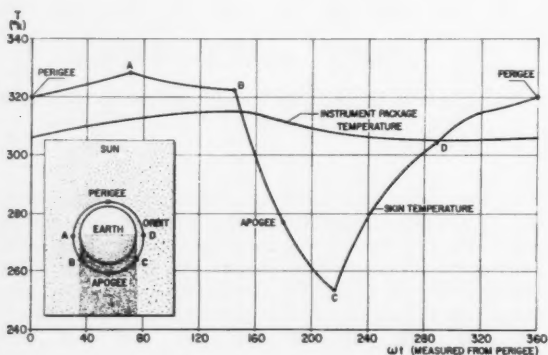


Fig. 15 Temperature during revolution. Typical Explorer IV curve

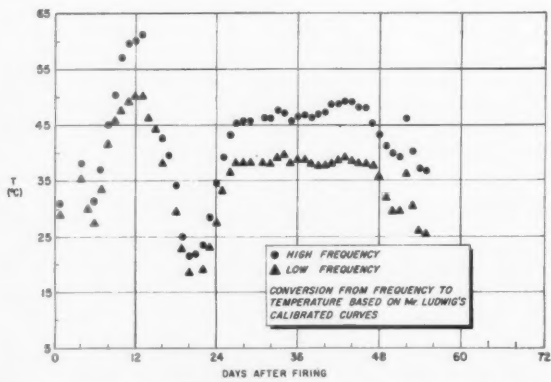


Fig. 16 Temperature of Explorer IV. Based on channel 3 frequencies received by ABMA tracking station

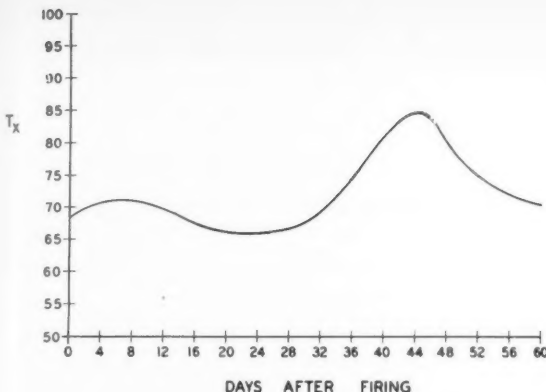


Fig. 17 Per cent time in sunlight (T_x) for Explorer IV vs. days after firing

variation of environmental conditions, accuracy of orbital characteristics and accuracy in determining time in sunlight. It can be concluded that the constancy and accuracy of these factors has been fairly close for Explorer IV. It is not intended to generalize this for other satellites, because of the many factors involved.

The temperature measurements allow an analysis of the spinning behavior and the direction of the momentum vector. The following interpretation is offered.

At the time of launching, the angle between the longitudinal axis of the satellite and the sun's direction was 75 deg. This was simultaneously the direction of the momentum vector. The area exposed to the sun was 97 per cent.

In the first 6 days of orbiting, the mode of spin changed to a rotation around a major axis of inertia. The momentum vector remained essentially the same. The angle between the momentum vector and the sun vector would decrease to 71 deg. It is interesting to note that the area did not reduce to the 63 per cent minimum, but to about 68 per cent, which corresponds to an angle of 77 deg between momentum vector and sun vector.

After 6 days, the flat spin had fully developed. Interaction with the atmosphere became strong and caused a rotation of the momentum vector. The rate of change was up to 15 deg per day. This caused the exposed area to fluctuate between the extremes of 100 and 63 per cent. After 26 days, the rate of change seemed to decrease considerably. However, since this is a three-dimensional problem, this break in the area curve may indicate merely a change in the direction of the rotation of the momentum vector.

It is possible to draw conclusions from the temperature measurements on the behavior of satellites in space. Since three angles are involved and only one measurement made, two types of ambiguities remain: Determination of the quadrant in which the momentum vector is located, and determination of whether the plane of momentum vector and sun vector has rotated from its original location. To resolve such ambiguities, additional measurements are needed. An entirely independent method of attitude determination has been used and published elsewhere (8).

This method uses the signal strength of received radio signals. Fig. 20 shows the correlation of the attitude obtained by temperature evaluation and the evaluation of radio signals.

Conclusions

The temperature of satellites can be controlled by passive means. The on-board instrument temperatures can be kept between 0 and 65 C during an operating time of 60 to 90

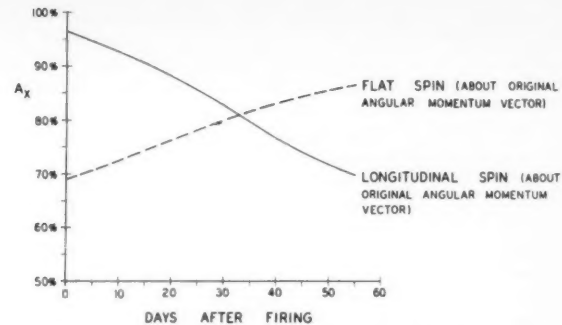


Fig. 18 Theoretical projected area (A_x) of Explorer IV vs. days after firing

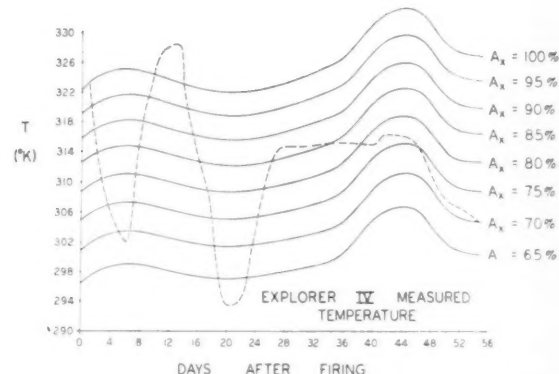


Fig. 19 Measured temperature of Explorer IV superimposed on theoretical curves

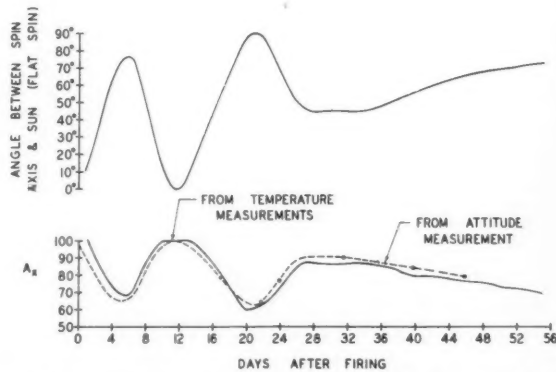


Fig. 20 Projected area and angle between spin and sun vs. days after firing (as deduced from Fig. 19)

days. Temperature variations of the skin can be kept between -30 and 90 C.

The thermal control of the Explorer satellites was based on an analysis of all influencing parameters. Relationships were developed by numerical evaluation on an IBM 704 computer, taking all variable factors into account.

Time in sunlight and attitude angle to the sun can be controlled by the time of firing. The launching date cannot be freely chosen, but the hour of firing allows an angular vari-

ation of the orbital plane by 360 deg. The time of firing has been used with the Explorer satellites as an effective control parameter.

The thermal design of the satellite was based on insulation between skin and instruments. Heat transfer coefficients by conduction and radiation were determined theoretically and experimentally by prototype testing.

The interval of ± 32 deg to which a satellite's instruments can be controlled is determined by the external parameters, such as orbital characteristics, firing time, solar constant, albedo, Earth radiation, attitude, mode of spin, and their variations with time.

The nominal value of the temperature which is the mean of the interval is determined mainly by the on-board parameters: Absorptivity to solar radiation, emissivity in infrared, heat capacities, heat transfer coefficients and internal heat release. For a body without heat release and without heat capacity, the ratio of emissivities has the decisive influence. See Table 2.

Explorers I and IV had times in sunlight between 65 and 80 per cent, during the operating time of 90 and 60 days, respectively. Explorer III went to 100 per cent sunlight during 4-5 days, 30 days after launching. Measured temperature during this time was 40 C.

Due to the low design temperature, the upper temperature limit was not exceeded. It is very likely that the temperature dropped below the lower limit after 43 days, causing the transmitter to drop out.

Acknowledgments

Work described in this paper was carried out as part of the Explorer assignment by the ABMA team. Main credit should go to this team rather than to individuals. However, I would like to mention those who were closely connected with the analyses and the evaluation of the satellite

Table 2 Explorer temperature control

Explorer	Mean design temp., C	Measured temp., C	
		Max.	Min.
I	20	40	0
III	20	41	0*
IV	40	55	19

* Actual temperature lower, but no measurements because transmitter ceased operating.

results described herein: Raymond Smith, Computation Laboratory; Klaus Schocken, William Jones, William Snoddy, Robert Naumann and Charles Cochran, Research Projects Laboratory.

References

- Heller, G., "The Explorer, the Explorer Story and the Temperature Control of the Satellite Package," in "Ten Steps to Space," Franklin Institute, Phila., 1958.
- Krause, H. G. L., "The Secular and Periodic Perturbations of the Orbit of an Artificial Earth Satellite," presented at the seventh IAF Congress, Rome, 1956.
- Krause, H. G. L., "The Motion of a Satellite Station Around the Earth in an Elliptical Orbit Inclined to the Earth's Equator," Rand Rep. no. T-52 (translated by R. E. Vernon), Oct. 21, 1955.
- Cunningham, L. E., "The Motion of a Nearby Satellite with Highly-Inclined Orbit," *Astron. J.*, vol. 62, Jan. 1957.
- Hibbs, A., "The Temperature of an Orbiting Missile," Jet Propulsion Laboratory, Calif. Institute of Technology, Pasadena, Calif., Rep. no. 20-294.
- Van Allen, J. A., "Scientific Uses of Earth Satellites," Univ. of Mich. Press, Ann Arbor, Mich.
- Heller, G., "Thermal Problems of Satellites," presented at Sagamore Conf. on Space Environment, Sept. 16-19, 1958. (To be published by Syracuse Univ., Syracuse, N.Y.)
- Naumann, R., "The Determination of Satellite Spatial Orientation, Using Explorer IV as an Example," Army Science Conf., 1959.

Minimum Time Flight Paths

G. M. Schindler¹

Advanced Technology Corp.
Santa Barbara, Calif.

A general condition is derived which must be satisfied by an aircraft or space vehicle in order to reach a predetermined point in a minimum time. The thrust, lift and drag can depend, in an arbitrary (differentiable) manner, on the instantaneous position and velocity coordinates (or Mach number) as well as on the angle of attack between the directions of the thrust and the velocity. In order to make the solution applicable to space vehicles as well as to aircraft, the cases of a spherical and a flat Earth are treated separately.

THE PROBLEM of determining brachistochronic trajectories has been investigated by numerous authors from different points of view and under different assumptions (2-6).² The most general treatment probably originates from Miele (1), who considers the present problem from the standpoint of a variational problem of Mayer type. In that paper, however, the minimum conditions (Euler equations) still seem

Received April 5, 1959.

¹ Chief Mathematician.

² Numbers in parentheses indicate References at end of paper.

to be quite inconvenient since, in addition to the trajectory parameters, a number of Lagrangian multipliers have to be determined. Only in very special cases can these equations be integrated in a closed form.

It is possible, however, to arrive at a rather simple minimum condition if the same problem is treated as a classical variational problem. This minimum condition and the equations of motion together represent the necessary number of equations for the complete determination of the desired trajectory and the required flight parameter.

The Case of a Spherical Earth

In a space fixed system of coordinates x, y , the instantaneous position of the space vehicle can be described by the radius vector

$$\mathbf{X} = \begin{pmatrix} x \\ y \end{pmatrix} = \begin{pmatrix} r \cos \varphi \\ r \sin \varphi \end{pmatrix} \quad [1]$$

Here r and φ are the circular polar coordinates. The instantaneous velocity is given by

$$\dot{\mathbf{X}} = \begin{pmatrix} \dot{x} \\ \dot{y} \end{pmatrix} = \begin{pmatrix} \dot{r} \cos \varphi - r\dot{\varphi} \sin \varphi \\ \dot{r} \sin \varphi + r\dot{\varphi} \cos \varphi \end{pmatrix} = \begin{pmatrix} v_1 \\ v_2 \end{pmatrix} \quad [2]$$

where a dot stands for the derivative with respect to the time t . The following forces are acting on the center of gravity of the vehicle: Thrust \mathbf{T} , lift \mathbf{L} , drag \mathbf{D} and gravitational force \mathbf{G} (Fig. 1). If m is the instantaneous mass of the vehicle, the equation of motion [3] can be written in components as follows

$$\frac{d}{dt}(m\dot{\mathbf{X}}) = \mathbf{T} + \mathbf{D} + \mathbf{L} + \mathbf{G} \quad [3]$$

Taking into account that the drag vector \mathbf{D} is pointing in the direction opposite to that of the velocity vector $\dot{\mathbf{X}}$, that \mathbf{L} is perpendicular to $\dot{\mathbf{X}}$, that \mathbf{T} forms the angle of attack α with $\dot{\mathbf{X}}$, and that \mathbf{G} is pointing toward the center of Earth O , the equation of motion [3] can be written in components as follows

$$m(\dot{v}_1 + \gamma \cos \varphi) = (\tau \cos \alpha - \delta - \dot{m}v) \frac{v_1}{v} - (\tau \sin \alpha + \lambda) \frac{v_2}{v} \quad [4a]$$

$$m(\dot{v}_2 + \gamma \sin \varphi) = (\tau \sin \alpha + \lambda) \frac{v_1}{v} + (\tau \cos \alpha - \delta - \dot{m}v) \frac{v_2}{v} \quad [4b]$$

Here τ, δ, λ and γ stand for the absolute magnitudes of $\mathbf{T}, \mathbf{D}, \mathbf{L}$ and \mathbf{G}/m , respectively, and the instantaneous velocity v is given by

$$v = |\dot{\mathbf{X}}| = \sqrt{v_1^2 + v_2^2} = \sqrt{\dot{r}^2 + r^2\dot{\varphi}^2} \quad [5]$$

The quantities τ, δ and λ are, in general, empirical functions of "altitude" r , Mach number M and angle of attack α . If the physical properties (density, temperature, etc.) of Earth's atmosphere are assumed to be spherically symmetrical and, therefore, functions of r only, the Mach number can be expressed in terms of r and v . For the mathematical treatment of this problem it suffices to assume these quantities to be arbitrary (differentiable) functions of the local coordinates r, φ , the velocity components v_1 and v_2 , and the angle of attack α . The fuel consumption \dot{m} is supposed to be a function of the same variables. Thus we assume

$$\begin{aligned} \tau &= \tau(r, \varphi, v_1, v_2, \alpha) \\ \delta &= \delta(r, \varphi, v_1, v_2, \alpha) \\ \lambda &= \lambda(r, \varphi, v_1, v_2, \alpha) \\ \dot{m} &= \dot{m}(r, \varphi, v_1, v_2, \alpha) \\ \gamma &= g_0 R^2 / r^2 \end{aligned} \quad [6]$$

Here R is the radius of Earth, and g_0 is the gravitational acceleration at Earth's surface.

Now, taking into account that the velocity components v_1 and v_2 are functions of r, \dot{r}, φ and $\dot{\varphi}$ according to Equation [2], one finds that the equations of motion [4a and 4b] represent two differential equations for the three unknown functions $r(t), \varphi(t)$ and $\alpha(t)$. If, therefore, one of these three functions is chosen to be a known function of time t , the remaining two functions are already determined by the equations of motion. This means that there is only one degree

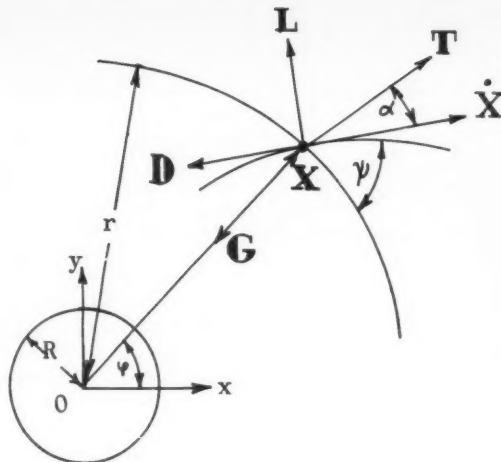


Fig. 1 Illustration of the coordinate system

of freedom which can be used for the determination of the minimum time trajectory in question. We now choose the function $\alpha(t)$ so that the time to reach a final point (r_1, φ_1) starting from a point (r_0, φ_0) is a minimum. For this purpose it is necessary to derive an explicit expression for the flight time itself. This can be done by first excluding the case where

$$\dot{v}_1 + \gamma \cos \varphi = 0 \quad [7a]$$

$$\dot{v}_2 + \gamma \sin \varphi = 0 \quad [7b]$$

These equations represent exactly Kepler's equation of motion of a mass under the influence of a central force. Dividing one of the equations of motion [4a and 4b] by the other, one obtains

$$\frac{\dot{v}_1 + \gamma \cos \varphi}{\dot{v}_2 + \gamma \sin \varphi} = \frac{Av_1 - Bv_2}{Bv_1 + Av_2} \quad [8]$$

where

$$A(r, \varphi, v_1, v_2, \alpha) = \tau \cos \alpha - \delta - \dot{m}v \quad [9a]$$

$$B(r, \varphi, v_1, v_2, \alpha) = \tau \sin \alpha + \lambda \quad [9b]$$

Rearrangement of Equation [8] leads to

$$\frac{v_1'(Bv_1 + Av_2) - v_2'(Av_1 - Bv_2)}{\gamma[(Av_1 - Bv_2) \sin \varphi - (Bv_1 + Av_2) \cos \varphi]} = 1 \quad [10]$$

Here we introduce φ to be the independent variable and denote the derivative with respect to φ by a prime. It follows that

$$\frac{v_1'(Bv_1 + Av_2) - v_2'(Av_1 - Bv_2)}{\gamma[(Av_1 - Bv_2) \sin \varphi - (Bv_1 + Av_2) \cos \varphi]} d\varphi = dt \quad [11]$$

where the time t is separated, if, in the expression on the left-hand side, the quantities r, v, v_1, v_2 and α are considered to be functions of φ . Integration with respect to φ from φ_0 to φ_1 leads to the relation

$$\int_{\varphi_0}^{\varphi_1} \frac{[v_1'(Bv_1 + Av_2) - v_2'(Av_1 - Bv_2)] d\varphi}{\gamma[(Av_1 - Bv_2) \sin \varphi - (Bv_1 + Av_2) \cos \varphi]} = \int_{\varphi_0}^{\varphi_1} F d\varphi = t_1 - t_0 \quad [12]$$

On the right-hand side, the flight time $t_1 - t_0$ needed to reach a point of the set (r, φ_1) occurs explicitly. The integrand F in [12] depends on $\varphi, r(\varphi), v_1(\varphi), v_1'(\varphi), v_2(\varphi), v_2'(\varphi), v(\varphi)$, and $\alpha(\varphi)$. It is clear that the time also occurs implicitly in the velocity $v(\varphi)$, since the functions $r(\varphi)$ and $v(\varphi)$ together completely describe both the geometrical and chronological motion of the vehicle. In order to obtain from Equation [12] a necessary condition for the minimum flight time, however, one can reason in the following manner: For arbitrary given flight path characteristics, which are represented by $\varphi, r(\varphi)$ and $v(\varphi)$ [the velocity components $v_1(\varphi)$ and $v_2(\varphi)$ are uniquely determined by $r(\varphi)$ and $v(\varphi)$], the integral in Equation [12] is a minimum only if the Euler equation with respect to α is satisfied. Since this is true for arbitrary $r(\varphi)$ and $v(\varphi)$, it is also true for the optimum flight path, if it exists. In the present case, the Euler equation with respect to α is

$$\frac{\partial F}{\partial \alpha} = \frac{\gamma}{N^2} \left[\frac{v_1'(Bv_1 + Av_2) - v_2'(Av_1 - Bv_2)}{\gamma \{(Av_1 - Bv_2) \sin \varphi - (Bv_1 + Av_2) \cos \varphi\}} \right] = 0 \quad [13]$$

Taking into account that α only occurs explicitly in the quantities A and B , one obtains for [13]

$$\begin{aligned} \frac{\gamma}{N^2} & \left\{ [(Av_1 - Bv_2) \sin \varphi - (Bv_1 + Av_2) \cos \varphi] \times \right. \\ & [v_1'(B_\alpha v_1 + A_\alpha v_2) - v_2'(A_\alpha v_1 - B_\alpha v_2)] - \\ & [(A_\alpha v_1 - B_\alpha v_2) \sin \varphi - (B_\alpha v_1 + A_\alpha v_2) \cos \varphi] \times \\ & \left. [v_1'(Bv_1 + Av_2) - v_2'(Av_1 - Bv_2)] \right\} = 0 \quad [14] \end{aligned}$$

where N is the expression in the denominator of F and the subscript α denotes the partial derivative with respect to α . A suitable collection of the particular terms within the braces in [14] leads to

$$\frac{\gamma}{N^2} (v_1' \sin \varphi - v_2' \cos \varphi)(AB_\alpha - BA_\alpha)v^2 = 0 \quad [15]$$

Multiplication by $d\varphi/dt \neq 0$ leads to the minimum condition

$$\begin{aligned} \frac{(v_1 \sin \varphi - v_2 \cos \varphi)v^2}{\gamma[(Av_1 - Bv_2) \sin \varphi - (Bv_1 + Av_2) \cos \varphi]^2} \times \\ (AB_\alpha - BA_\alpha) = 0 \quad [16] \end{aligned}$$

This condition has to be satisfied along with the equations of motion [4a and 4b]. Multiplying [4a] by $\sin \varphi$ and [4b] by $\cos \varphi$ and subtracting the second from the first, one obtains

$$\begin{aligned} v_1 \sin \varphi - v_2 \cos \varphi = \\ \frac{1}{mv} [(Av_1 - Bv_2) \sin \varphi - (Bv_1 + Av_2) \cos \varphi] \quad [17] \end{aligned}$$

Equation [16] then can be written as

$$\frac{(AB_\alpha - BA_\alpha)v^2}{mv\gamma[(Av_1 - Bv_2) \sin \varphi - (Bv_1 + Av_2) \cos \varphi]} = 0 \quad [18]$$

from which the minimum condition in question becomes

$$AB_\alpha - BA_\alpha = 0 \quad [19]$$

The quantities A and B are functions of r, φ, v_1, v_2 and α as stated in Equations [9a and 9b]. From [19] one obtains α as a function of r, φ, v_1 and v_2

$$\alpha = \alpha(r, \varphi, v_1, v_2) \quad [20]$$

Replacing α in the equations of motion [4a and 4b] by [20] and using for v_1 and v_2 the kinematic relations [2], one obtains

the equations of motion in the form

$$m[(\ddot{r} - r\dot{\varphi}^2) \cos \varphi - (2\dot{r}\dot{\varphi} + r\ddot{\varphi}) \sin \varphi] = f_1(r, \varphi, \dot{r}, \dot{\varphi}) \quad [21a]$$

$$m[(2\dot{r}\dot{\varphi} + r\ddot{\varphi}) \cos \varphi + (\ddot{r} - r\dot{\varphi}^2) \sin \varphi] = f_2(r, \varphi, \dot{r}, \dot{\varphi}) \quad [21b]$$

From these equations the functions $r(t)$ and $\varphi(t)$ can be determined. Under rather weak assumptions on f_1 and f_2 (Lipschitz condition), system [21a, 21b] leads to unique solutions $r(t)$ and $\varphi(t)$ which satisfy the initial conditions at $t = t_0$

$$r(t_0) = r_0 \quad \dot{r}(t_0) = \dot{r}_0 \quad [22a]$$

$$\varphi(t_0) = \varphi_0 \quad \dot{\varphi}(t_0) = \dot{\varphi}_0 \quad [22b]$$

The entirety of the solutions issuing from the initial point (r_0, φ_0) forms a two-parametric family of curves where \dot{r}_0 and $\dot{\varphi}_0$ are the parameters. For given fixed initial velocity

$$v_0 = \sqrt{\dot{r}_0^2 + r_0^2 \dot{\varphi}_0^2} \quad [23]$$

only the initial direction of the flight path can still be chosen. Measuring the initial flight path angle ψ_0 from the line tangent at the circle with radius r_0 , this angle is given by

$$\tan \psi_0 = \dot{r}_0/r_0 \dot{\varphi}_0 \quad [24]$$

By a suitable choice of ψ_0 a trajectory can be performed which passes through a given final point (r_1, φ_1) . Every point lying on that particular curve is then reached in a minimum time.

Finally it may be mentioned that one arrives at the same minimum condition, if in Equation [10] the variable r is chosen to be the independent variable instead of φ .

The Case of a Flat Earth

This case differs from that of a spherical Earth insofar as the force of gravity G is pointing toward the negative direction of the y axis (Fig. 1). The equations of motion are in the Cartesian system of coordinates x, y ,

$$mv_1 = (\tau \cos \alpha - \delta - \dot{m}v) \frac{v_1}{v} - (\tau \sin \alpha + \lambda) \frac{v_2}{v} \quad [25a]$$

$$mv_2 = (\tau \sin \alpha + \lambda) \frac{v_1}{v} + (\tau \cos \alpha - \delta - \dot{m}v) \frac{v_2}{v} \quad [25b]$$

where

$$\begin{aligned} v_1 &= \dot{x} \\ v_2 &= \dot{y} \\ v &= \sqrt{v_1^2 + v_2^2} = \sqrt{\dot{x}^2 + \dot{y}^2} \end{aligned} \quad [26]$$

The quantities τ , δ , λ and \dot{m} are assumed to be arbitrary (differentiable) functions of the horizontal distance x , the altitude y , the velocity components v_1 and v_2 and the angle of attack α

$$\begin{aligned} \tau &= \tau(x, y, v_1, v_2, \alpha) \\ \delta &= \delta(x, y, v_1, v_2, \alpha) \\ \lambda &= \lambda(x, y, v_1, v_2, \alpha) \\ \dot{m} &= \dot{m}(x, y, v_1, v_2, \alpha) \end{aligned} \quad [27]$$

γ is given by

$$\gamma = (y_0^2 g_0)/y^2 \quad [28]$$

where g_0 is the gravitational acceleration at altitude $y = y_0$. Excluding here the ballistic trajectories which result from

$$\begin{aligned} v_1 &= \dot{x} = 0 \\ v_2 + \gamma &= \dot{y} + \gamma = 0 \end{aligned} \quad [29]$$

and dividing one of the equations of motion [25a, 25b] by the

other, one obtains

$$\frac{\dot{v}_1(Bv_1 + Av_2) - \dot{v}_2(Av_1 - Bv_2)}{\gamma(Av_1 - Bv_2)} = 1 \quad [30]$$

Here A and B have the same significance as in Equations [9a and 9b]. Introducing x to be the independent variable and denoting the derivative with respect to x by a prime, it follows from [30] that

$$\frac{v_1'(Bv_1 + Av_2) - v_2'(Av_1 - Bv_2)}{\gamma(Av_1 - Bv_2)} dx = dt \quad [31]$$

Integration with respect to x from x_0 to x_1 leads to the flight time $t_1 - t_0$ needed to reach a point of the set (x_1, y)

$$\int_{x_0}^{x_1} \frac{v_1'(Bv_1 + Av_2) - v_2'(Av_1 - Bv_2)}{\gamma(Av_1 - Bv_2)} dx = \int_{x_0}^{x_1} F dx = t_1 - t_0 \quad [32]$$

To make the flight time a minimum we can reason in the same manner as we did in the previous case. The minimum condition is then

$$\frac{\partial F}{\partial \alpha} = 0 \quad [33]$$

which is equivalent to

$$v_1'(AB\alpha - BA\alpha)v^2/\gamma[Av_1 - Bv_2]^2 = 0 \quad [34]$$

Multiplying this equation by $dx/dt \neq 0$ and using the equations of motion, one obtains the minimum condition

$$AB\alpha - BA\alpha = 0 \quad [35]$$

which is the same as that in the case of a spherical Earth. The only difference is that the quantities τ , δ , λ , \dot{m} and γ which occur in A and B have to be replaced by those given in Equations [27 and 28].

The minimum time flight path in this case is again determined by first solving Equation [35] for α and then integrating the equations of motion for $x(t)$ and $y(t)$ with proper initial conditions at $t = t_0$

$$x(t_0) = x_0 \quad \dot{x}(t_0) = \dot{x}_0 \quad [36a]$$

$$y(t_0) = y_0 \quad \dot{y}(t_0) = \dot{y}_0 \quad [36b]$$

For given fixed initial velocity

$$v_0 = \sqrt{\dot{x}_0^2 + \dot{y}_0^2} \quad [37]$$

and a suitable choice of the initial flight path angle

$$\tan \psi_0 = \dot{y}_0/\dot{x}_0 \quad [38]$$

a trajectory can be performed which passes through the given final point (x_1, y_1) . Every point lying on this particular curve is reached in a minimum time.

Remarks

The Euler equations [18 and 34] represent necessary conditions for a stationary behavior of the corresponding integrals [12 and 32]. As it can be seen, these equations involve also the necessary condition for the maximum flight time, namely $v = 0$. If, therefore, the function F in each case is continuous and not identically constant, the stated conditions for the minimum flight time paths are even sufficient.

It may happen that for different sets of initial values the corresponding brachistochronic trajectories will both pass through the two given points (x_0, y_0) and (x_1, y_1) . This, however, is not surprising, since the Euler equations in general do not furnish unique solutions for extremals "in the large." The question for the absolute minimum time trajectory in such a case can be answered after determining the flight times explicitly according to Equations [12 and 32].

References

- 1 Miele, A., "General Variational Theory of Flight Paths of Rocket Powered Aircraft, Missiles and Satellite Carriers," *Aeronautica Acta*, vol. IV, 1958, pp. 264-288.
- 2 Cicala, P. and Miele, A., "Brachistochronic Maneuvers of a Variable Mass Aircraft in a Vertical Plane," *J. Aeron. Sci.*, vol. 22, no. 8, Aug. 1955, pp. 577-578.
- 3 Carstoiu, J., "On a Minimum Time Flight Path of a Jet Aircraft," *J. Aeron. Sci.*, vol. 24, no. 9, Sept. 1957, pp. 704-706.
- 4 Lawden, D. F., "Optimum Rocket Trajectories," *JET PROPULSION*, vol. 27, no. 12, Dec. 1957, p. 1263.
- 5 Dommasch, P. O., "Methods of Dynamic Performance as Applied to the Minimum Time to Climb," *Aeron. Engng. Rep.* 331, Princeton Univ., 1956.
- 6 Theodorson, T., "Optimum Path of an Airplane—Minimum Time to Climb," *J. Aero/Space Sci.*, vol. 26, no. 10, Oct. 1959, pp. 637-642.
- 7 Courant, R. and Hilbert, D., "Methods of Mathematical Physics," Intersc. Pub., Inc., N.Y., 1953.
- 8 Weise, K. H., "Gewöhnliche Differentialgleichungen," Wolfenbütteler Verlagsanstalt G.m.b.H., Wolfenbüttel und Hannover, 1948.

ROCKETRY LETTER SYMBOLS NOW AVAILABLE

The American Society of Mechanical Engineers has just published the new American Standard Letter Symbols for Rocket Propulsion, ASA Y10.14-1959, approved last September by the American Standards Assn. Sponsored by ASME, in collaboration with the AMERICAN ROCKET SOCIETY and the Institute of the Aeronautical Sciences, the standard letter symbols are available from the American Society of Mechanical Engineers, 29 West 39th St., New York 18, N.Y., at a price of \$2 per copy, with quantity discounts available.

Combustion Intensity in a Heterogeneous Stirred Reactor

WELBY G. COURTNEY¹

Experiment Incorporated
Richmond, Va.

A theoretical analysis of combustion intensity of liquid monopropellant in a heterogeneous stirred reactor is presented. The argument consists mainly of deducing the steady-state concentration of partly burned drops with radius r which remain in the reactor when a polydispersed spray is fed into the reactor. The resulting equation is intractable, but an approximation to this equation shows that combustion intensity increases with increasing density of burned gas in the reactor, increasing burning rate of a single droplet, and particularly with increasing number of smaller size droplets in the feed spray. Quantitative prediction of combustion intensity is limited by severe uncertainty in the burning rates of droplets under the turbulent reactor conditions.

A DETAILED theoretical analysis of combustion intensity in an actual combustion chamber in terms of elementary transport and chemical reactions will be very difficult in view of the tortuous flow patterns in the chamber. However, it may be hoped that chamber performance can be predicted to a satisfactory degree in terms of simple idealized flow patterns or simple combinations of these patterns.

Theories of chamber performance can, in general, be divided into the one-dimensional and well-stirred flow patterns. In the one-dimensional or plug flow approach it is assumed that a combustible material is passed down a tube and progressively undergoes combustion. Combustion of a gaseous material for simple plug flow has been analyzed by numerous investigators (1)² and for plug flow with recycle of part of the burned products by Spalding (2). Combustion of a heterogeneous dust or spray in simple plug flow has also been widely investigated (3,4,5). Penner (6) and Hartwig (7) analyzed evaporation of liquid droplets during simple plug flow in a rocket motor, assuming that a droplet was surrounded by the hot gas products during its residence in the motor.

In the well-stirred reactor approach (8) it is assumed that fresh material is instantaneously and perfectly mixed with a volume of burning material, and that the composition everywhere in this volume is the same as the material leaving the volume. Homogeneous combustion of a gas in a single stirred reactor was analyzed by Longwell et al. (9) and others (10,11), who related blowout conditions to combustion kinetics.³

Two stirred homogeneous reactors in series were discussed by DeZubay (12). Hottel et al. (13) analyzed two stirred homogeneous reactors in parallel with part of the products from the first reactor being fed into the second reactor, and the products from the second reactor being mixed with fresh combustible gas and fed into the first reactor. An infinite series of well-stirred homogeneous reactors with fresh combustible gas added to each reactor was analyzed by Avery and Hart (14) and Rosen and Hart (15).

Although the stirred reactor scheme seems intuitively to resemble closest the chaotic conditions in an actual combustion chamber, there appears to have been no theoretical analysis of combustion in a heterogeneous stirred reactor, where combustion intensity depends upon the burning rate

Presented at the ARS Semi-Annual Meeting, June 8-12, 1959,
San Diego, Calif.

¹ Senior Scientist.

² Numbers in parentheses indicate References at end of paper.

³ Spalding (2) surmised that the actual flow patterns in these experimental studies involved turbulent plug flow surrounded by an envelope of recirculating burned gas rather than true well-stirred flow.

of a liquid droplet or a solid particle. A theoretical analysis of the combustion of liquid monopropellant in a heterogeneous stirred reactor is presented herein.

Theory

Consider a liquid monopropellant combustion chamber which is operated as a well-stirred heterogeneous reactor. Liquid monopropellant is fed into the chamber as a spray, which is instantaneously mixed with the chamber contents. A flame envelope forms around a droplet, and the droplet progressively burns. A proportion of the chamber contents (gaseous products plus partially burned droplets) then passes through the exhaust nozzle. We will assume:

1 The rate of combustion in the chamber is limited by the rate at which a droplet burns.

2 Essentially all drops leave the chamber before being completely burned.

3 There is no droplet agglomeration or fracture in the chamber.

4 Steady state.

The mathematical analysis given here often follows the discussion of nucleation and growth of solid particles in a stirred reactor given by Bransom et al. (16).

Let a monopropellant liquid with mass flow rate W_0 gm per sec per unit chamber volume be fed as a spray into a decomposition chamber of volume V liters. Let the concentration distribution of the unburned spray be $n_0(r_0)$, where $n_0(r_0)dr_0$ is the number of unburned spray drops per liter of chamber volume whose radii are between r_0 and $r_0 + dr_0$. The rate of addition of these drops is thus $n_0(r_0)dr_0$, but for present purposes the derivative with respect to time may be neglected since the steady-state drop population in the chamber does not change with time. At a later time some of the drops added earlier will have been lost through the nozzle, and those which have remained in the chamber, $n(r_0)$, will have been partly burned. The rate of loss of these drops through the nozzle is

$$-\frac{dn(r_0)}{d\theta} = n(r_0) \cdot \frac{v}{V} \quad [1]$$

where

θ = age of drop in the chamber, sec

v = rate of flow of burned gas from the chamber, liters per sec

Integration of Equation [1] gives

$$n(r_0) = n_0(r_0) \cdot e^{-v\theta/V} \quad [2]$$

where $n(r_0)d\theta$ is the steady-state concentration of burned drops whose initial radii were between r_0 and $r_0 + dr_0$ and which have age between θ and θ plus $d\theta$.

Investigations of the burning behavior of single drops indicate an induction period for the formation of a flame envelope around a drop and then steady burning of the drop. Nishiwaki (17) concluded that the induction period decreased with

$$\epsilon = \frac{8\pi\rho_l}{3k\rho_g} \int_0^{r_0} \cdot dr$$

decreasing drop radius. The specific value of the burning constant k (and probably the induction period also) depends upon the temperature (18), pressure (18) and particularly the turbulence (18,19) of the gaseous environment. For the present illustrative purpose we will neglect the induction period and assume that k is a constant, or

$$-d(r^2)/d\theta = k \quad [3]$$

$$dr/d\theta = -k/2r \quad [4]$$

$$\theta = (r_0^2 - r^2)/k \quad [5]$$

Converting $n(r_0)d\theta$ to $n(r_0)dr$ by Equations [2, 4 and 5], and multiplying by -1 (to make dr go from 0 to r_0 instead of r_0 to 0) gives

$$n(r_0) = \frac{2r n_0(r_0) \cdot \exp[v(r^2 - r_0^2)/kV]}{k} \quad [6]$$

where $n(r_0)dr$ is the steady-state concentration of burned drops with radii between r and $r + dr$, and whose initial radii were between r_0 and $r_0 + dr_0$. The total concentration of burned drops $N(r)dr$ with radii between r and $r + dr$ includes, for example, those with small initial diameter and short residence time plus those with large initial diameter and long residence time, or

$$N(r) = \frac{2r \cdot \exp[vr^2/kV] \cdot \int_{r_{0\min}}^{r_{0\max}} \exp[-vr_0^2/kV] \cdot n_0(r_0) \cdot dr_0}{k} \quad [7]$$

where $r_{0\max}$ and $r_{0\min}$ are the maximum and minimum drop radii in the initial spray.

The steady-state weight of drops per liter of chamber volume is

$$W = \int_{r_{0\min}}^{r_{0\max}} w(r) \cdot dr \quad [8]$$

where

$$w(r) = 4\pi r^3 \rho_l N(r)/3$$

ρ_l = density of the liquid drops which is assumed to be constant

The lower integration limit is the radius of the smallest droplet in the chamber and can probably be replaced by zero without introducing appreciable error. Therefore

$$W = \frac{8\pi\rho_l}{3k} \int_0^{r_{0\max}} r^4 \cdot \exp\left[\frac{vr^2}{kV}\right] \cdot \left[\int_{r_{0\min}}^{r_{0\max}} \exp\left(\frac{-vr_0^2}{kV}\right) \cdot n_0(r_0) \cdot dr_0 \right] \cdot dr \quad [9]$$

Combustion intensity ϵ in grams of monopropellant burned per liter of chamber volume per sec is equal to the mass rate of flow of monopropellant into the chamber minus the mass rate of loss of droplets from the chamber, or

$$\epsilon = \dot{W}_g - W \cdot v \quad [10]$$

Also

$$v = \dot{W}_g/\rho_g \quad [11]$$

where

\dot{W}_g = rate of flow of gas from the chamber, gm per sec

ρ_g = density of the outflowing gas

Material balance gives $\epsilon = \dot{W}_g$ [12]

Finally, combustion intensity is obtained by substituting Equations [9, 11 and 12] into Equation [10], giving

$$\dot{W}_g = \frac{\dot{W}_0}{1 + 2r_0^2 \dot{W}_0 / (5k\rho_g)} \quad [13]$$

Equation [13] appears to be intractable for explicitly relating combustion intensity to the other parameters, but could be solved numerically if the values of the parameters were known. Unfortunately, k is unknown and there would seem to be little hope of guessing a reasonable value of k on theoretical grounds in view of the uncertain but undoubtedly high degree of turbulence in the combustion chamber. An experimental investigation with a heterogeneous stirred reactor is required to investigate k , and even then the value of k will probably vary with combustion intensity.

However, if we assume for convenience a monodispersed spray with initial drop radius r_0 , the integral in Equation [13] is dominated by r_0^4 , and Equation [13] may be approximated by neglecting the exponential factors, giving

$$\epsilon \sim \frac{\dot{W}_0}{1 + 2r_0^2 \dot{W}_0 / (5k\rho_g)} \quad [14]$$

In Equation [14], combustion intensity increases as k or ρ_g increases and particularly as r_0 decreases. Thus, combustion intensity with a polydisperse spray would increase with increasing number of smaller size droplets.

References

- 1 Hirschfelder, J. O., Curtiss, C. F. and Campbell, D. E., "The Theory of Flames and Detonations," in "Fourth Symposium (International) on Combustion," Williams and Wilkins, Baltimore, 1953, p. 190.
- 2 Spalding, D. B., "Theoretical Relationships between Combustion Intensity and Pressure Drop for One-Stream Combustion Chambers," A.R.C. 19, 18 C.F. 393, Aeronautical Research Council, Gt. Britain, April 10, 1957.
- 3 Miesse, C. C., "On the Combustion of a Liquid Fuel Spray," in "Sixth Symposium (International) on Combustion," Reinhold Publishing Co., Inc., N. Y., 1957, p. 732.
- 4 Cassel, H. M., Liebman, I. and Mock, W. K., "Radiative Transfer in Dust Flames," in "Sixth Symposium (International) on Combustion," Reinhold Publishing Co., Inc., N. Y., 1957, p. 602.
- 5 Burgoyne, J. H. and Cohen, L., "The Effect of Drop Size on Flame Propagation in Liquid Aerosols," Proc. Royal Society, vol. A, no. 225, 1954, p. 242.
- 6 Penner, S. S., "On Maximum Evaporation Rates of Liquid Droplets in Rocket Motors," JOURNAL OF THE AMERICAN ROCKET SOCIETY, vol. 23, 1953, p. 85.
- 7 Hartwig, F. W., "Maximum Evaporation Rates for Nonisothermal Droplets," JOURNAL OF THE AMERICAN ROCKET SOCIETY, vol. 23, 1953, p. 242.
- 8 Denbigh, K. G., "Velocity and Yield in Continuous-Reaction Systems," Trans. Faraday Society, vol. 40, 1944, p. 352.
- 9 Longwell, J. P., Frost, E. E. and Weiss, M. A., "Flame Stability in Bluff Body Recirculation Zones," Ind. Engng. Chem., vol. 45, 1953, p. 1629.
- 10 Longwell, J. P. and Weiss, M. A., "High Temperature Reaction Rates in Hydrocarbon Combustion," Ind. Engng. Chem., vol. 47, 1955, p. 1634.
- 11 Hottel, H. C., Williams, G. C. and Baker, M. W., "Combustion Studies in a Stirred Reactor," in "Sixth Symposium (International) on Combustion," Reinhold Publishing Co., Inc., N. Y., 1957, p. 398.
- 12 DeZubay, E. A., "A Comparative Investigation of a Homogeneous Combustion Chamber With a Two-Stage Combustion Chamber," JET PROPULSION, vol. 26, 1956, p. 77.
- 13 Hotel, H. C., Williams, G. C. and Bonnell, A. H., "Application of Well-Stirred Reactor Theory to the Prediction of Combustor Performance," Combustion and Flame, vol. 2, 1958, p. 13.
- 14 Avery, W. H. and Hart, R. W., "Combustor Performance with Instantaneous Mixing," Ind. Engng. Chem., vol. 45, 1953, p. 1634.
- 15 Rosen, P. and Hart, R. W., "A Constant-Area, Constant-Temperature Combustor," J. Aeron. Sci., vol. 20, 1953, p. 549.
- 16 Bransom, W. H., Dunning, W. J. and Millard, B., "Kinetics of Crystallization in Solution. Part I," Disc. Faraday Society, vol. 5, 1949, p. 83.
- 17 Nishiwaki, Niichi, "Kinetics of Liquid Combustion Processes: Evaporation and Ignition Lag of Fuel Droplets," in "Fifth Symposium (International) on Combustion," Reinhold Publishing Co., Inc., N. Y., 1955, p. 148.
- 18 Goldsmith, M., "Experiments on the Burning of Single Drops of Fuel," JET PROPULSION, vol. 26, 1956, p. 172.
- 19 Agoston, G. A., Wise, H. and Rosser, W. A., "Dynamic Factors Affecting the Combustion of Liquid Spheres," in "Sixth Symposium (International) on Combustion," Reinhold Publishing Co., Inc., N. Y., 1957, p. 708.

Technical Notes

Estimation of Nonequilibrium Reaction Flight Regimes for Blunt Bodies at Hypersonic Speeds¹

T. C. ADAMSON Jr.²

University of Michigan, Ann Arbor, Mich.

AN IMPORTANT question which arises in the consideration of aerodynamic heating problems is that of ascertaining the flight regimes in which nonequilibrium reaction occurs. A general idea of this regime may be gained by an order of magnitude analysis where the characteristic time of reaction is compared to the characteristic residence time, with limiting values of the ratios obtained, arbitrarily assigned. Moreover, such an order of magnitude analysis is useful in those cases where the flow is very far from equilibrium; and recombination may take place, finally, along the surface, since an idea of the wetted area of reaction may be obtained. This type of study is of value in those cases where either catalytic or reaction poisoning surfaces are being considered.

In this analysis, the flow field is assumed to be that around a blunt body at hypersonic speeds such that a detached shock exists. The field is divided into two separate regions, each with its own characteristic time. One is the stagnation point flow between the detached shock and the body. The other is the laminar boundary layer flow along the body surface. Each region has a characteristic residence time which is to be compared with the characteristic chemical reaction time.

According to Li and Geiger (1) the detachment distance between a detached shock and the stagnation point is, as in Fig. 1

$$b = \left\{ \frac{-1 + \sqrt{1 - (1 - k)^2}}{(1 - k)^2} \right\} k R_{s_0} \quad [1]$$

where

$k = \rho_\infty / (\rho_s)_{x=0}$

s = conditions immediately behind the shock

R_{s_0} = radius of curvature if the shock at $x = 0$

If, as assumed by Li, the radius of curvature of the shock is the same as that of the body, at $x = 0$, then b may be calculated. Also, from his calculations, the velocity in the y direction outside the boundary layer is essentially proportional to y ; since the v velocity in the boundary layer is well approximated by a linear function, the average velocity in the region between the detached shock and the body along the stagnation streamline is, to good approximation

$$v_{avg} = v_s / 2 \quad [2]$$

The residence time in this region is thus

$$t_r = 2b / v_{avg} \quad [3]$$

Original received Nov. 18, 1958 and revised Feb. 1, 1960.

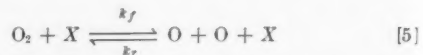
¹This work was supported by Air Force Contract no. AF 18(600)-1607 under a subcontract with Bell Aircraft Corp.

²Associate Professor of Aeronautical and Astronautical Engineering.

The characteristic chemical time consistent with Equation [3] is then

$$t_c = \frac{(\rho_2)_s}{(w_2)_{recombination}} = \frac{(\rho_2)_s}{(k_r N \Omega_2 N_2^2)} \quad [4]$$

for the reaction



where X is any third body and the subscript 2 refers to oxygen atoms. $(w_2)_{recombination}$ is that part of the reaction rate which holds for the recombination of oxygen atoms, since this is the essential reaction in the decreasing temperature field. It is calculated using the concentration of O and O_2 existing behind a normal shock, but at the wall temperature. This is a very conservative calculation, since an average temperature between the wave and the body would certainly be higher than the wall temperature, and the recombination rate term is sensitive to changes in temperature. Since no accurate value for the average temperature was known and since it is evident that a linear variation is unrealistic, the conservative value for the reaction rate constant was chosen. For a

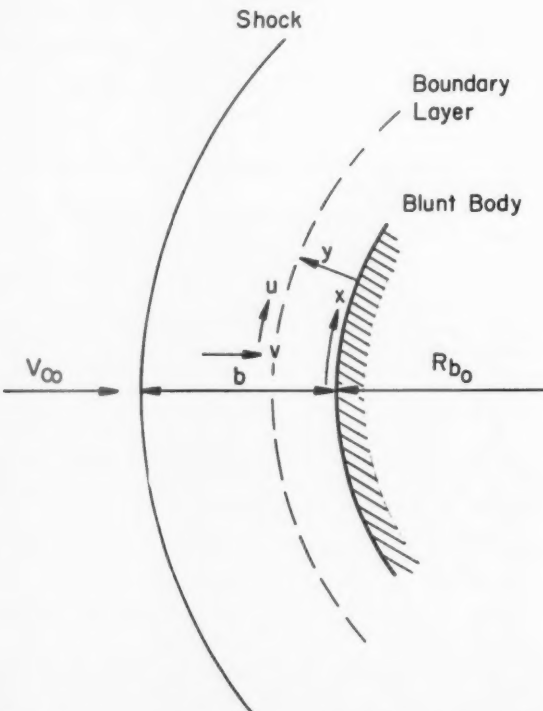


Fig. 1 Stagnation point region between a detached shock and a blunt body

EDITOR'S NOTE: The Technical Notes and Technical Comments sections of ARS JOURNAL are open to short manuscripts describing new developments or offering comments on papers previously published. Such manuscripts are usually published without editorial review within a few months of the date of receipt. Requirements as to style are the same as for regular contributions (see masthead page).

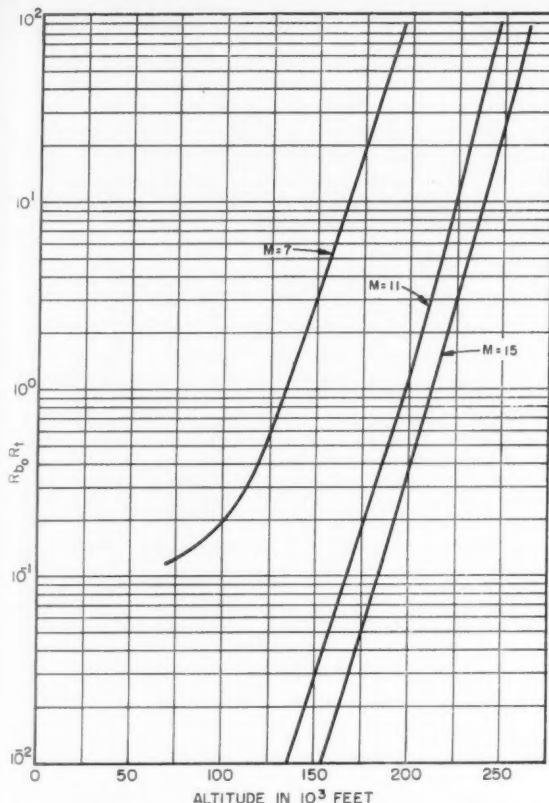


Fig. 2 Variation of time ratio function with altitude with flight Mach number as parameter for blunt nose body with radius of curvature R_{b0} ft, $T_{wall} = 1500$ K

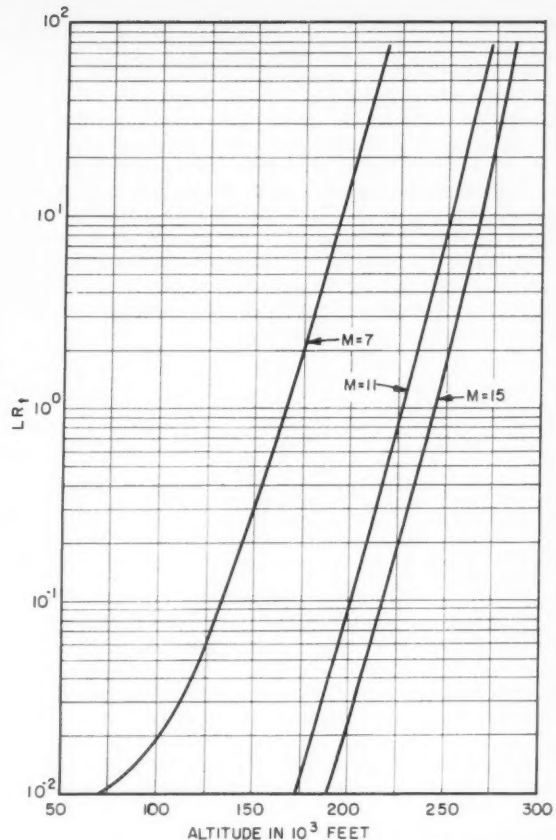


Fig. 3 Variation of time ratio function with altitude with flight Mach number as parameter for downstream distance along body surface L ft, $T_{wall} = 1500$ K

more complete comparison, one could use the values of the temperature behind the normal shock for another limit, although this was not done for the present calculation.

From Equations [1, 2 and 3], the ratio of characteristic times R_t can be written as

$$R_t = \frac{t_c}{t_r} = \frac{1}{R_{b0}} \frac{v_a}{2k} \left[\frac{-1 + (1 - (1 - k)^2)^{1/2}}{(1 - k)^2} \right] \frac{(\kappa_2)_e}{2k_r \left(\frac{P}{R_0} \right)_e \frac{1}{T_w^2} \left(\frac{\kappa_2^2}{\kappa_2 + 1} \right)_e} \quad [6]$$

where relative mass fractions have been introduced for the mole fractions in the rate term. According to Hirschfelder (2)

$$k_r = 1.2 \times 10^{16} \left(\frac{T}{300} \right)^{5/2} \frac{cm^6}{(moles)^2 sec} \quad [7]$$

and as noted, is calculated using T_w .

Using values given in (3 and 4), R_t , R_{b0} was computed and plotted as a function of altitude with Mach number as a parameter (Fig. 2). In these calculations, T_w was taken to be 1500 K. It is interesting to note that according to Fig. 2, as the Mach number increases at a constant altitude $R_{b0}R_t$ decreases. Thus the characteristic chemical time decreases faster than the characteristic residence time. Although the velocity behind the bow wave increases, the reaction rate in-

creases as the square of the pressure, and this effect is stronger than the velocity increase. Since the temperature behind the wave increases along with the Mach number, it is clear that the use of some average temperature behind the wave, rather than the wall temperature, would cause R_t to decrease even more as the Mach number increases, if the reaction rate is proportional to $T^{5/2}$.

For any arbitrary limiting value of R_t with a given nose radius R_{b0} , the range of flight Mach numbers and altitudes can be found, below which the stagnation flow can be considered to be in chemical equilibrium. For example, if $R_t \leq 10^{-2}$ is chosen as a limiting value, then for a blunt body of 1-ft nose radius at flight Mach number 11 the flow is considered to be in equilibrium for altitudes less than 135,000 ft. As the altitude increases the existence of chemical equilibrium becomes less and less probable until nonequilibrium reaction results. Since this was a conservative calculation, the altitude in the example noted must represent the lower limit for non-equilibrium reaction.

R_t may also be used to find the approximate conditions at which surface reaction can take place. Thus when $R_t \geq 1$, the oxygen atoms could reach the body surface before reacting. In order to calculate the order of magnitude of the possible wetted area of reaction, another characteristic residence time, the boundary layer residence time, must be compared with the chemical reaction time. In this case, a convective term and the reaction term in the species continuity equation may be compared to obtain the desired time ratio.

$$R_t = \frac{t_c}{t_r} = \frac{\rho u (\partial \kappa_2 / \partial x)}{(w_2)_{\text{recombination}}} \quad [8]$$

This ratio is then the mass of oxygen atoms convected per unit volume per unit time to the mass of oxygen atoms disappearing by recombination per unit volume per unit time. It should be noted that the diffusion terms, in the boundary layer equations, are the same order as the convection terms, so that this ratio should hold for the time associated with the cross stream diffusion of mass as well as the time associated with the convection of mass, as long as the Schmidt number $\mu/\rho D$ is of order 1. If $\partial \kappa_2 / \partial x \sim (\kappa_2)_s / L$ and $u \sim v_s$, then substituting for w_2 as in Equation [6] one can calculate $R_t L$ in a similar manner. Thus

$$R_t = \frac{1}{L} \frac{v_s (\kappa_2)_s}{2k_r \left(\frac{P}{R_0} \right)^2 \frac{1}{T_w^2} \left(\frac{\kappa_2^2}{\kappa_2 + 1} \right)} \quad [9]$$

Fig. 3 contains the plot of $R_t L$ vs. altitude with Mach number as a parameter. As in the previous calculation, the values of κ_2 were approximated by those existing behind the normal shock, whereas the same temperature was used to calculate k_r .

Fig. 3 may be used to obtain an order of magnitude of the possible atom wetted area for these cases where (according to Fig. 2) $R_t \gg 1$, i.e., where the characteristic chemical time is greater than the residence time, and hence atomic species enter the boundary layer. For example, for a blunt nose body of 1-ft nose radius traveling at Mach number 11 at 225,000-ft altitude, R_t is 10, according to Fig. 2, so that atomic species enter the boundary layer. To calculate the order of the distance back along the body where one might find atomic species, one finds from Fig. 3 that at 225,000-ft altitude, when $M = 11$, $R_t L$ is 0.85. Therefore $R_t \leq 1$ if $L \geq 0.85$ ft; i.e., the atom wetted area extends downstream to the order of 0.85 ft, so that surface reaction could extend back to this distance.

It is evident that the same type of calculation could be carried out to find the conservative downstream limit of the region of nonequilibrium flow for those cases where R_t is greater than the arbitrarily assigned value of 10^{-2} in the stagnation point calculation. That is, if the initial computation at

the stagnation point indicated that $R_t > 10^{-2}$ the downstream distance L to the point where $R_t = 10^{-2}$ could be calculated using Fig. 3.

It should be emphasized that the values obtained in Figs. 2 and 3 depend entirely on the chemical parameters used in the reaction rate term, and since there is some argument as to what these values should be, the results of these analyses are inconclusive insofar as absolute values are concerned. However, they do illustrate a method of calculation which should become of more quantitative value when more accurate chemical parameters are available.

Nomenclature

b	= distance between body and detached shock along stagnation streamline
k_f	= forward specific reaction rate constant
k_r	= reverse specific reaction rate constant
L	= distance along body surface downstream from stagnation point
M	= molecular weight
N_2	= moles of atomic oxygen per unit volume
N	= moles of mixture per unit volume
P	= pressure
R_b	= radius of curvature of blunt nosed body
R_0	= universal gas constant
R_t	= ratio of characteristic chemical time to characteristic residence time
T	= temperature
w_2	= rate at which mass of atomic oxygen is formed by chemical reaction per unit volume per unit time
ρ_2	= density of atomic oxygen
κ_2	= relative mass fraction of atomic oxygen

Subscripts

0	= at stagnation point
s	= immediately downstream of detached shock
w	= at wall
∞	= flight conditions

References

- Li, T. Y. and Geiger, R. E. "Stagnation Point of a Blunt Body in Hypersonic Flow," *J. Aeron. Sci.*, vol. 24, Jan. 1957, pp. 25-32.
- Hirschfelder, J. O., "Heat Transfer in a Chemically Reacting Gas Mixture," University of Wisconsin, WIS-ONR-18, Feb. 6, 1956, pp. 15-16.
- "The Standard Atmosphere Sea Level to 300,000 Feet," Bell Aircraft Information Note, no. 3, June 1956.
- McKown, P., "Equilibrium Composition and Flow Variables for Air Dissociated by a Strong Shock Wave," Bell Aircraft Report no. 02-984-040, March 8, 1957.

Sloshing of Liquids in Cylindrical Tanks of Elliptic Cross Section¹

WEN-HWA CHU²

Southwest Research Institute, San Antonio, Texas

An analysis is made of the sloshing of liquids in partially filled rigid cylindrical tanks of elliptic cross section. By application of potential theory, the forces and moments acting on the tank are determined for the case of translational and rotational excitation along or about the major and minor axes of the cross section, and expressions for the resonant frequencies are found in terms of the roots of the derivatives of modified Mathieu functions. The lowest few

Received April 17, 1959.

¹ The results presented in this paper were obtained during the course of research carried out under sponsorship of the Army Ballistic Missile Agency, Huntsville, Ala., under Contract DA-23-072-ORD-1251.

² Research Engineer, Engineering Analysis Section, Department of Applied Mechanics.

resonant frequency parameters, as computed from those expressions, are compared with those of a circular cylinder having the same cross-sectional area.

SLOSHING motions of fuel in partially filled tanks of missiles may be established by essentially lateral accelerations of the vehicle. Such liquid motions are of importance, for there is the possibility of extreme oscillations if the frequency of excitation is in the neighborhood of one of the natural frequencies of the liquid fuel. The forces exerted by the fuel on the tank walls may then lead to perturbations in the flight trajectory, or may even impose severely high stresses on structural components.

The force and moment resulting from free oscillations of the fuel in a rectangular tank have been presented in (1),³ and those resulting from horizontal (translational), pitching (rocking) and yawing oscillations of the rectangular tank are given in (2). The free oscillations of fuel in tanks of other cross sectional shapes are also given in (1). The same prob-

³ Numbers in parentheses indicate References at end of paper.

lem for circular tanks undergoing horizontal and rotational oscillations is treated in (3 through 5). Sloshing in flexible tanks, considering such elastic vibrations as breathing, bending and rotationally symmetric modes, are treated in (6 through 8).

The tank of circular cross section is simple and is generally employed in missiles; however, some out-of-roundness may exist in practice or in laboratory models, and it is conceivable that tanks of elliptic cross section may even be desired for certain applications. It has been noted (9) that the wave motion can become very complex when the variation in tank diameter is on the order of 0.4 per cent or greater. Consequently it is of some interest to investigate analytically the sloshing of liquids in elliptic tanks. The result of the analysis

(13) is presented in this paper. Although only a limited amount of computational effort has been carried out, it is possible to infer some of the dynamic effects resulting from even a small ellipticity. The theory is not, however, restricted to tanks with small ellipticity.

Force and Moment Acting on the Tank

The tank is assumed to possess translational oscillations x_b , y_b and rotational oscillation θ_x , θ_y , all of small amplitude. The incompressible potential problem (3, 4, 5, 13) is solved by separation of variables and expansions analogous to those in the problem of vibration of elliptic membrane (10).

The forces and moments are given as follows

$$F_x = -M\ddot{x}_b - \frac{1}{2}Mh\ddot{\theta}_y \sum_{m=1}^{\infty} \sum_{n=1,3,\dots}^{\infty} \left[\frac{L_{mn}^{(1)}}{\cosh \xi_b} \right] \cdot \frac{2 \sinh (\mu_{mn}^{(1)} h)}{\mu_{mn}^{(1)} h} Ce_n(\xi_b q_{mn}^{(1)}) A_1^{(n)}(q_{mn}^{(1)}) - M \sum_{m=1}^{\infty} \sum_{n=1,3,\dots}^{\infty} \left[\frac{L_{mn}^{(1)}}{\cosh \xi_b} \right] \times \\ Ce_n(\xi_b q_{mn}^{(1)}) A_1^{(n)}(q_{mn}^{(1)}) \tanh (\mu_{mn}^{(1)} h) \left\{ \omega^2 \ddot{x}_b + h\ddot{\theta}_y \left(\omega^2 \left[1 - \frac{2 \sinh (\mu_{mn}^{(1)} h)}{\mu_{mn}^{(1)} h} \right] - \frac{\alpha_T}{h} [1 - 2 \cosh (\mu_{mn}^{(1)} h)] \right) \right\} + Mg\theta_y \quad [1a]$$

where

$$L_{mn}^{(1)} = \frac{\int_0^{\xi_b} \int_0^{2\pi} \cosh \xi \cos \eta Ce_n(\xi, q_{mn}^{(1)}) ce_n(\eta, q_{mn}^{(1)}) [\cosh(2\xi) - \cos(2\eta)] d\eta d\xi}{\pi \int_0^{\xi_b} Ce_n(\xi, q_{mn}^{(1)}) [\cosh(2\xi) - \theta_n(q_{mn}^{(1)})] d\xi} \quad [1b]$$

$$L_{mn}^{(1)} = 0 \quad [1c]$$

when n is even

$$\theta_n(q_{mn}^{(1)}) = \frac{1}{\pi} \int_0^{2\pi} ce_n^2(\eta, q_{mn}^{(1)}) \cos(2\eta) d\eta \quad [1d]$$

$$F_y = -M\ddot{y}_b + \frac{1}{2}Mh\ddot{\theta}_x - Mh\ddot{\theta}_x \sum_{m=1}^{\infty} \sum_{n=1,3,\dots}^{\infty} \left[\frac{L_{mn}^{(1)}}{\sinh \xi_b} \right] \frac{2 \sinh (\mu_{mn}^{(2)} h)}{\mu_{mn}^{(2)} h} Se_n(\xi_b q_{mn}^{(2)}) B_1^{(n)}(q_{mn}^{(2)}) - M \sum_{m=1}^{\infty} \sum_{n=1,3,\dots}^{\infty} \left[\frac{L_{mn}^{(2)}}{\sinh \xi_b} \right] \times \\ \tanh (\mu_{mn}^{(2)} h) Se_n(\xi_b q_{mn}^{(2)}) B_1^{(n)}(q_{mn}^{(2)}) \left\{ \omega^2 \ddot{y}_b - h\ddot{\theta}_x \left(\omega^2 \left[1 - \frac{2 \sinh (\mu_{mn}^{(2)} h)}{\mu_{mn}^{(2)} h} \right] - \frac{\alpha_T}{h} [1 - 2 \cosh (\mu_{mn}^{(2)} h)] \right) \right\} - Mg\theta_x \quad [2a]$$

where

$$L_{mn}^{(2)} = \frac{\int_0^{\xi_b} \int_0^{2\pi} \sinh \xi \sin \eta Se_n(\xi, q_{mn}^{(2)}) se_n(\eta, q_{mn}^{(2)}) [\cosh(2\xi) - \cos(2\eta)] d\eta d\xi}{\pi \int_0^{\xi_b} Se_n^2(\xi, q_{mn}^{(2)}) [\cosh \xi - \psi_n(q_{mn}^{(2)})] d\xi} \quad [2b]$$

$$L_{mn}^{(2)} = 0 \quad [2c]$$

when n is even

$$\psi_n(q_{mn}^{(2)}) = \frac{1}{\pi} \int_0^{2\pi} se_n^2(\eta, q_{mn}^{(2)}) \cos(2\eta) d\eta \quad [2d]$$

$$My = -Mh\ddot{x}_b \left(\frac{1}{2} + \frac{a^2}{4h^2} \right) - \frac{1}{3}Mh^2\ddot{\theta}_y + Mh^2\ddot{\theta}_y \sum_{m=1}^{\infty} \sum_{n=1,3,\dots}^{\infty} \frac{L_{mn}^{(1)}}{\cosh \xi_b} \cdot \frac{2[\mu_{mn}^{(1)} h \cosh(\mu_{mn}^{(1)} h) - \sinh(\mu_{mn}^{(1)} h)]}{(\mu_{mn}^{(1)} h)^3} \times \\ Ce_n(\xi_b q_{mn}^{(1)}) A_1^{(n)}(q_{mn}^{(1)}) - Mh \sum_{m=1}^{\infty} \sum_{n=1,3,\dots}^{\infty} \frac{L_{mn}^{(1)} Ce_n(\xi_b q_{mn}^{(1)}) A_1^{(n)}(q_{mn}^{(1)})}{\cosh \xi_b (\mu_{mn}^{(1)} h)^2[(\omega_{mn}^{(1)})^2 - \omega^2]} \left\{ \mu_{mn}^{(1)} h \tanh(\mu_{mn}^{(1)} h) - 1 + \operatorname{sech}(\mu_{mn}^{(1)} h) \right\} \times \\ \left\{ \omega^2 \ddot{x}_b + \theta_y h \left(\omega^2 \left[1 - \frac{2 \sinh(\mu_{mn}^{(1)} h)}{\mu_{mn}^{(1)} h} \right] - \frac{\alpha_T}{h} [1 - 2 \cosh(\mu_{mn}^{(1)} h)] \right) \right\} - Mh \sum_{m=1}^{\infty} \sum_{n=1,3,\dots}^{\infty} \frac{L_{mn}^{(1)}}{\cosh \xi_b} \cdot \frac{\operatorname{sech} \mu_{mn}^{(1)} h}{(\mu_{mn}^{(1)} h)^2[(\omega_{mn}^{(1)})^2 - \omega^2]} \times \\ \left\{ \frac{q_{mn}^{(1)}}{\sinh \xi_b} [T_{n,2}^{(1)}(\xi_b) A_1^{(n)}(q_{mn}^{(1)}) - T_{n,1}^{(1)}(\xi_b) A_3^{(n)}(q_{mn}^{(1)})] \right\} \cdot \left\{ \omega^2 \ddot{x}_b + h\ddot{\theta}_y \left(\omega^2 \left[1 - \frac{2 \sinh (\mu_{mn}^{(1)} h)}{\mu_{mn}^{(1)} h} \right] - \frac{\alpha_T}{h} [1 - 2 \cosh (\mu_{mn}^{(1)} h)] \right) \right\} + \\ gMh\theta_y \left[\frac{1}{2} + \frac{a^2}{4h^2} \right] \quad [3a]$$

where

$$T_{n,l}^{(1)}(\xi_b) = \int_0^{\xi_b} C e_n(\xi, q_{mn}^{(1)}) \cosh(l\xi) d\xi \quad [3b]$$

and

$$\begin{aligned} M_x &= \ddot{y}_b M h \left(\frac{1}{2} + \frac{b^2}{4h^2} \right) - \frac{1}{3} M h^2 \ddot{\theta}_x + M h^2 \ddot{\theta}_z \sum_{m=1}^{\infty} \sum_{n=1,3,\dots}^{\infty} \left[\frac{L_{mn}^{(2)}}{\sinh \xi_b} \right] \cdot \frac{2[\mu_{mn}^{(2)} h \cosh(\mu_{mn}^{(2)} h) - \sinh(\mu_{mn}^{(2)} h)]}{(\mu_{mn}^{(2)} h)^3} \times \\ S e_n(\xi_b, q_{mn}^{(2)}) B_1^{(n)}(q_{mn}^{(2)}) &- M h \sum_{m=1}^{\infty} \sum_{n=1,3,\dots}^{\infty} \frac{L_{mn}^{(2)}}{\sinh \xi_b} \cdot \frac{e_n(\xi_b, q_{mn}^{(2)}) B_1^{(n)}(q_{mn}^{(2)})}{(\mu_{mn}^{(2)} h)^2[(\omega_{mn}^{(2)})^2 - \omega^2]} \left\{ \mu_{mn}^{(2)} h \tanh(\mu_{mn}^{(2)} h) - 1 + \operatorname{sech}(\mu_{mn}^{(2)} h) \right\} \times \\ \left\{ -\omega^2 \ddot{y}_b + h \ddot{\theta}_x \left(\omega^2 \left[1 - \frac{2 \sinh(\mu_{mn}^{(2)} h)}{\mu_{mn}^{(2)} h} \right] - \frac{\alpha_r}{h} [1 - 2 \cosh(\mu_{mn}^{(2)} h)] \right) \right\} - M h \sum_{m=1}^{\infty} \sum_{n=1,3,\dots}^{\infty} \frac{L_{mn}^{(2)} \operatorname{sech}(\mu_{mn}^{(2)} h)}{\sinh \xi_b (\mu_{mn}^{(2)} h)^2[(\omega_{mn}^{(2)})^2 - \omega^2]} \times \\ \left\{ \frac{q_{mn}^{(2)}}{\cosh \xi_b} \left[T_{n,3}^{(2)}(\xi_b) B_1^{(n)}(q_{mn}^{(2)}) - T_{n,1}^{(2)}(\xi_b) B_2^{(n)}(q_{mn}^{(2)}) \right] \right\} \times \\ \left\{ -\omega^2 \ddot{y}_b + h \ddot{\theta}_x \left(\omega^2 \left[1 - \frac{2 \sinh(\mu_{mn}^{(2)} h)}{\mu_{mn}^{(2)} h} \right] - \frac{\alpha_r}{h} [1 - 2 \cosh(\mu_{mn}^{(2)} h)] \right) \right\} + g M h \theta_z \left[\frac{1}{2} + \frac{b^2}{4h^2} \right] \quad [4a] \end{aligned}$$

where

$$T_{n,l}^{(2)}(\xi_b) = \int_0^{\xi_b} S e_n(\xi, q_{mn}^{(2)}) \sinh(l\xi) d\xi \quad [4b]$$

In the limiting case of zero ellipticity ($c \rightarrow 0$, $\frac{1}{2}ce^k \rightarrow r$), the previous results agree with those of a circular cylindrical tank (4,5).

Numerical Examples

In order to obtain some idea of the change in resonant frequencies, two elliptic cylinders of 1 and 5 per cent out-of-roundness, respectively, are considered, the out-of-roundness being defined by $(a-b)/(a+b)$.

The lowest six parametric zeros entering the general problem of these two cases are calculated by making use of the available asymptotic formulas (10) and are given in Table 1.

Define a frequency parameter $N = \omega^2 R / \alpha_r$, where R is the radius of a circular cylinder of the same cross-sectional area. The resonant frequency parameters are then

$$N_{mn} = \lambda_{mn} \sqrt{\frac{b}{a}} \tanh \left[\lambda_{mn} \sqrt{\frac{b}{a}} \frac{h}{R} \right]$$

$$(\lambda_{mn} = 2\sqrt{q_{mn}} \cosh \xi_b)$$

As $h/R \rightarrow \infty$ (or sufficiently large), the lowest six resonant frequencies of the given examples are compared with the lowest two of the equivalent circular cylinder in Table 2.

Discussion

It is noted that although the calculated values of $\lambda_{mn}^{(1)}$ and $\lambda_{mn}^{(2)}$ are higher than the corresponding $\lambda_{mn}^{(0)}$, the reso-

Table 1 Parametric zeros

(1a)	$(a-b)/(a+b) = 0.01$	(1b)	$(a-b)/(a+b) = 0.01$
$q_{11}^{(1)} = 0.03334$	$q_{11}^{(2)} = 0.03460$	$q_{11}^{(1)} = 0.15743$	$q_{11}^{(2)} = 0.18678$
$q_{21}^{(1)} = 0.28143$	$q_{21}^{(2)} = 0.28740$	$q_{21}^{(1)} = 1.3630$	$q_{21}^{(2)} = 1.5144$
$q_{13}^{(1)} = 0.17648$	$q_{13}^{(2)} = 0.17648$	$q_{13}^{(1)} = 0.87887$	$q_{13}^{(2)} = 0.88058$
...

Table 2 Comparison of resonant frequency parameters $h/R \rightarrow \infty$

(2a)	$(a-b)/(a+b) = 0.01$	(2b)	$(a-b)/(a+b) = 0.05$	$(a-b)/(a+b) = 0$
A	B	C	D	E
$N_{11}^{(1)} = 1.8259$	$N_{11}^{(2)} = 1.8599$	$N_{11}^{(1)} = 1.7569$	$N_{11}^{(2)} = 1.9303$	$N_1^{(0)} = 1.841 = \lambda_{11}^{(0)}$
$N_{12}^{(1)} = 4.2008$	$N_{12}^{(2)} = 4.2008$	$N_{12}^{(1)} = 4.1872$	$N_{12}^{(2)} = 4.1912$	$4.201 = \lambda_{12}^{(0)}$
$N_{21}^{(1)} = 5.3047$	$N_{21}^{(2)} = 5.3607$	$N_{21}^{(1)} = 5.2145$	$N_{21}^{(2)} = 5.4964$	$N_2^{(0)} = 5.332 = \lambda_{21}^{(0)}$
...

A = Horizontal motion along the major axis or rotation around the minor axis

B = Horizontal motion along the minor axis or rotation around the major axis

C = Same as A

D = Same as B

E = Horizontal and rocking oscillation of a circular cylinder of the same cross-sectional area

nant frequency parameters $N_{11}^{(1)} < N_1^{(0)} < N_{11}^{(2)}$ and $N_{21}^{(1)} < N_2^{(0)} < N_{21}^{(2)}$. Furthermore, there are additional resonant frequencies introduced, due to the small ellipticity, corresponding to modified Mathieu functions of odd integer order higher than one. The numerical values of $N_{31}^{(1)}$ and $N_{31}^{(2)}$ are both slightly less than $\lambda_{13}^{(0)}$.

With some positive empirical damping (12), the maximum magnitude of the additional terms as well as the dominant terms can be calculated [see (13)]. In practice, it is often sufficient to consider only the lowest few modes.

To obtain some idea of the amplitudes, assume q_{mn} small and $h \rightarrow 0$; then, the coefficient of $1/[(\omega_{mn}/\omega)^2 - 1]$ of the additional modes due to ellipticity is roughly of the order

$$\frac{A_{11}^{(n)}(q_{mn}^{(1)})}{A_{11}^{(1)}(q_{11}^{(1)})} \cong \frac{\left(n - \frac{n-1}{2} - 1\right)!}{\left(\frac{n-1}{2}\right)! (n-1)!} \left(\frac{q_{mn}^{(1)}}{4}\right)^{(n-1)/2} = 0 \left(\frac{q_{mn}^{(1)}}{4}\right)$$

as compared with the coefficient of the fundamental mode, or of the order

$$\frac{B_{11}^{(n)}(q_{mn}^{(2)})}{B_{11}^{(1)}(q_{11}^{(1)})} = 0 \left(\frac{q_{mn}^{(2)}}{4}\right)$$

In the case of 1 per cent out-of-roundness, the values of $q_{13}^{(1)}/4$ and $q_{13}^{(2)}/4$ are slightly more than 4 per cent; therefore the actual amplitude of the lowest additional modes may be not really serious near the corresponding resonant frequency parameter. The case of larger q_{mn} cannot be easily discussed. The qualitative conclusion remains to be confirmed by experiments.

Acknowledgment

The author wishes to express his appreciation to Dr. H. N. Abramson and Mr. G. E. Ransleben Jr. for their suggestions and advice; and to Miss M. M. Schmitz and Mr. R. Gonzales for their assistance in carrying out the numerical computations.

Nomenclature

$2a$	= major axis of the elliptic cylinder
$2b$	= minor axis of the elliptic cylinder
c	= location of the foci of the ellipse
g	= magnitude of the gravitational acceleration
h	= height of the undisturbed liquid level
$q_{mn}^{(1)}$	= m th parametric zero of $Ce_n'(\xi_b, q) = 0$
$q_{mn}^{(2)}$	= m th parametric zero of $Se_n'(\xi_b, q) = 0$
x, y, z	= tank fixed Cartesian coordinates with origin at the center of the tank bottom (z upward along the tank axis)
x_b, y_b	= x - and y -components of the small displacement of the cylinder, respectively, with respect to Earth fixed coordinate system
$A_{mn}^{(n)}$	= coefficient of $\cos(m\eta)$ of the expansion of $ce_n(\eta, q)$
$B_{mn}^{(n)}$	= coefficient of $\sin(m\eta)$ of the expansion of $se_n(\eta, q)$
$Ce_n(\xi, q)$	= even modified Mathieu function of order n
$Ce_n'(\xi, q)$	= first derivative of $Ce_n(\xi, q)$ with respect to ξ
$ce_n(\eta, q)$	= even Mathieu function of order n
F_x, F_y	= x - and y -components of force acting on the tank
$L_{mn}^{(1)}$	= coefficient of the expansion of $\cosh \xi \cos \eta$ in modified Mathieu functions, defined by Equations [1b, 1c]
$L_{mn}^{(2)}$	= coefficient of the expansion of $\sinh \xi \sin \eta$ in modified Mathieu functions, defined by Equations [2b, 2c]

M_x, M_y	= moment about x and y axis, respectively, acting on the tank, due to liquid sloshing
M	= total mass of the fuel = $\pi\rho abh$
N_{mn}	= $(\omega_{mn})^2 R/\alpha_T$, resonant frequency parameter
$N_{mn}^{(0)}$	= m th resonant frequency parameter of a circular cylinder of radius R
R	= \sqrt{ab} , the radius of circular cylinder of the same area
$Se_n(\xi, q)$	= odd modified Mathieu function of order n
$Se_n'(\xi, q)$	= first derivative of $Se_n(\xi, q)$ with respect to ξ
$se_n(\eta, q)$	= odd Mathieu function of order n
ξ, η, z	= elliptic cylinder coordinates
θ_x, θ_y	= small, angular displacement of the tank about the x' and y' axis, respectively, measured from the vertical upward direction (x', y' are Cartesian coordinates translating but not rotating with tank)
ρ	= liquid density
ω	= frequency of oscillation
ω_{mn}	= resonant frequency corresponding to q_{mn}
$(\omega_{mn}^{(i)})^2$	= $\alpha_T \mu_{mn}^{(i)} \tanh(\mu_{mn}^{(i)} h)$; ($i = 1, 2$)
λ_{mn}	= $2\sqrt{q_{mn}} \cosh \xi$
$\lambda_{mn}^{(0)}$	= m th zero of the first derivative of the Bessel function of the first kind of order n , i.e., $J_n'(\lambda_{mn}^{(0)}) = 0$
μ_{mn}	= $2\sqrt{q_{mn}}/c$, separation constant corresponding to q_{mn}
α_T	= axial acceleration of the tank in the absence of gravity, i.e., axial acceleration minus axial component of gravity

Subscripts

(\cdot)	= first time derivative of $()$
$(\cdot\cdot)$	= second time derivative of $()$
$(\cdot)^{(0)}$	= quantities related to the cylinder of radius R , unless defined otherwise
$(\cdot)^{(1)}$	= quantities related to $q_{mn}^{(1)}$
$(\cdot)^{(2)}$	= quantities related to $q_{mn}^{(2)}$
$(\cdot)_b$	= for quantities related to the boundary

References

- Graham, E. W., "The Forces Produced by Fuel Oscillation in a Rectangular Tank," Douglas Aircraft Co., Inc., Santa Monica, Rep. no. SM-13748, April 1950, revised April 1951.
- Graham, E. W. and Rodriguez, A. M., "The Characteristics of Fuel Motion Which Affect Airplane Dynamics," *J. Appl. Mech.*, vol. 19, no. 3, Sept. 1952, pp. 381-388.
- Kachigan, K., "Forced Oscillations of a Fluid in a Cylindrical Tank," Convair, San Diego, Rep. ZU-7-046, Oct. 1956.
- Schmitt, A. F., "Forced Oscillations of a Fluid in a Cylindrical Tank Undergoing Both Translation and Rotation," Convair, San Diego, Rep. ZU-7-069, Oct. 1956.
- Bauer, H. F., "Fluid Oscillations in Circular Cylindrical Tank," ABMA, Huntsville, Ala., Rep. no. DA-TR-1-58, April 1958.
- Miles, J. W., "On the Sloshing of Liquid in a Flexible Tank," *J. Appl. Mech.*, vol. 25, no. 2, pp. 277-283, June 1958.
- Bauer, H. F., "Fluid Oscillations in a Circular Cylindrical Tank Due to Bending of Tank Wall," ABMA, Huntsville, Ala., Rep. no. DA-TR-3-58, April 1958.
- Reissner, E., "Notes on Forced and Free Vibrations of Pressurized Cylindrical Shells Which Contain a Heavy Liquid with a Free Surface," Ramo-Woolridge Corp., Los Angeles, Rep. no. AM6-15, GM-TR-87, Nov. 1956.
- Jacobsen, L. S. and Ayre, R. S., "Hydrodynamic Experiments with Rigid Cylindrical Tanks Subjected to Transient Motions," *Bull. Seismol. Soc. Amer.*, vol. 41, no. 4, pp. 313-346, Oct. 1951.
- McLachlan, N. W., "Theory and Application of Mathieu Functions," Clarendon Press, Oxford, Eng., first ed. 1947, reprinted 1951, pp. 10, 16-17, 19, 21, 28-29, 33-37, 46-47, 175-177, 221-223 and 294-299.
- Lord Rayleigh, "The Theory of Sound," Dover Publications, N. Y., first American ed. (A45), p. 298.
- Bauer, H. F., "Fluid Oscillations in a Cylindrical Tank with Damping," ABMA, Huntsville, Ala., Rep. no. DA-TR-4-58, April 1958.
- Chu, W. H., "Sloshing of Liquids in Cylindrical Tanks of Elliptic Cross-Section," Southwest Research Institute, San Antonio, Tech. Rep. no. 2, Contract DA-23-072-ORD-1251, SwRI Project 43-768-2, Sept. 1958.

Simple Formula for Prediction and Automatic Scrutiny

R. J. DUFFIN¹
Duke University, Durham, N. C.

T. W. SCHMIDT²

U. S. Army Office of Ordnance Research, Durham, N. C.

Prediction from data obtained at regular time intervals is discussed. Attention is restricted to the case in which the more recent data should be given more weight than past data. Thus a polynomial is fitted to the data by exponentially weighted least squares. It is found that the formula for predicting the next datum is quite simple. This formula needs to "remember" only a limited amount of data. The prediction formula can be used to automatically scrutinize data for gross error. A gross error or a gap in the data may be replaced by a predicted value, and the prediction and scrutiny process can be continued.

THIS paper deals with data obtained at regular time intervals. From a knowledge of a regular sequence of such observation, it is desired to predict the next observation. This prediction is carried out here by use of a least squares fit of the data with a polynomial.

We are concerned with a situation in which observations in the distant past should be given less weight than those more recent. More precisely, it is assumed that the observations should be discounted by a certain percentage in every time interval. This is taken to mean that the least squares formula has an exponential weight factor. It is found that this method of discounted least squares lends itself nicely to algebraic analysis. In particular, the constants of the prediction formula can be explicitly evaluated.

It is supposed that the sequence of observations is infinite, because this actually simplifies the formal considerations. On the other hand, the resulting prediction formula is a linear expression in the infinite sequence of observations. Such an infinite series is not too convenient for numerical evaluation. It proves possible, however, to obtain a finite formula which is essentially equivalent. Thus suppose the fit is to be given by a polynomial of degree less than m . Then the prediction is given by a simple formula involving only the last m observed values and the last m predicted values.

By "scrutiny of data" we mean rejection of obvious errors or blunders. In hand calculation this is often accomplished by visual inspection of a graph of the data. The trend in data processing is toward elimination of human judgment. The prediction formula can be employed as an automatic scrutator, to this end.

In automatic scrutiny, predicted and observed values are compared. If the "error" exceeds a prescribed tolerance, the observed value is rejected and is replaced by the predicted value. This process can be used also to replace gaps in observational data. The programming of the prediction and scrutiny formula for a digital computer is straightforward. The method and principal formulas are given in this paper. A more complete mathematical analysis and proof will be published elsewhere.

Discounted Least Squares

Let y_1, y_2, y_3, \dots be a sequence of real numbers. It may be supposed that these numbers are a time series of observations and that y_n is the observation at time $t = -n$. The developments considered in this paper stem from a certain approxima-

Presented at ARS Flight Testing Conference, Daytona Beach, Fla., March 23-25, 1959.

¹ Director of Special Research in Applied Mathematics.

² Chief, Systems Research Office.

Table 1 Straight line predictors

n	$Q(n)$	n	$Q(n)$
1	0.4000 0000	51	0.0000 2997
2	0.2800 0000	52	2455
3	0.1920 0000	53	2010
4	0.1280 0000	54	1644
5	0.0819 2000	55	1345
6	0.0491 5200	56	0.0000 1099
7	0.0262 1440	57	898
8	0.0104 8576	58	733
9	0.0000 0000	59	599
10	0.0067 1089	60	489
11	0.0107 3742	61	0.0000 0398
12	128 8490	62	325
13	137 4390	63	265
14	137 4390	64	216
15	131 9414	65	176
16	0.0123 1453	66	0.0000 0143
17	112 5900	67	117
18	101 3310	68	95
19	90 0720	69	77
20	79 2634	70	63
21	0.0069 1753	71	0.0000 0051
22	59 9519	72	41
23	51 6509	73	34
24	44 2722	74	27
25	37 7789	75	22
26	0.0032 1121	76	0.0000 0018
27	27 2008	77	15
28	22 6696	78	12
29	19 3428	79	10
30	16 2480	80	8
31	0.0013 6173	81	0.0000 0006
32	11 3890	82	5
33	9 5074	83	4
34	7 9228	84	3
35	6 5918	85	3
36	0.0005 4763	86	0.0000 0002
37	4 5433	87	2
38	3 7644	88	1
39	3 1154	89	1
40	2 5754	90	1
41	0.0002 1268	91	0.0000 0001
42	1 7546	92	1
43	1 4462	93	1
44	1 1910	94	0.0000 0000
45	9800		
46	0.0000 8058		
47	6621		
48	5436		
49	4460		
50	3657		

$$\text{Long formula: } m = 2, \theta = 0.8, y_0^* = \sum_{n=1}^{\infty} Q(n)y_n$$

$$\text{Short formula: } m = 2, \theta = 0.8, y_0^* = 0.4y_1 + 1.6y_1^* - 0.36y_2 - 0.64y_2^*$$

tion of the observations y_n by a polynomial

$$p(x) = \sum_{k=0}^{m-1} a_k x^k \quad [1]$$

The degree of $p(x)$ is taken to be less than a given integer m . As a matter of notation, it is convenient to write p_n if n is an integer.

A measure of the error of the approximation is defined to be

$$E = \sum_{n=1}^{\infty} \theta^n (p_n - y_n)^2 \quad [2]$$

Here the constant θ satisfies the inequality $0 < \theta < 1$. The

least square approximant is taken to be the polynomial p_n of degree less than m which minimizes E . Because the weight function θ^n is an exponential, an approximation of this type can be termed *discounted least squares*.

It is required to choose the coefficients a_k of $p(x)$ so that $p(x)$ minimizes E . This implies that $\partial E / \partial a_k = 0$ for $k = 0, 1, \dots, m - 1$. Carrying out the differentiations results in a system of m equations for the m coefficients. Solving these normal equations gives the least squares polynomial $p(x)$.

The polynomial $p(x)$ is used to extrapolate the sequence y_n . Of main concern is the "next value" y_0 . The predicted value of y_0 will be defined as $p(0)$. Since $p(0) = a_0$, it is simply necessary to solve the normal equations for a_0 . This yields a formula of the type

$$y_0^* = \sum_{n=1}^{\infty} Q(n)y_n \quad [3]$$

Here y_0^* denotes the predicted value y_0 , and $Q(n)$ denotes coefficients which depend on m and θ but not on the sequence y_n . We term Equation [3] "the long formula of prediction."

It proves possible to solve the normal equations explicitly. If we write $Q(n) = \theta^n q(n)$, then it is found that

$$q(x) = - \sum_{k=1}^m (1 - \theta^{-1})^k \binom{m}{k} \binom{x-1}{k-1} \quad [4]$$

Here $\binom{m}{k}$ denotes the binomial coefficient. It is seen that $q(x)$ is a polynomial of degree $m - 1$ in x . The polynomial $q(x)$ may be termed an associated Laguerre polynomial of discrete type because of a certain difference equation it satisfies.

Finite Prediction Formula

A practical difficulty with the long formula [3] is that if θ is close to unity, a great number of terms in the series must be retained. This might well put a burden on the computer's memory. The procedure described here avoids this difficulty because it is found sufficient to store only $2m$ properties of the infinite time series.

Let y_k^* be the predicted value of y_k in terms of preceding values. Then

$$y_k^* = \sum_{n=1}^{\infty} Q_n y_{n+k} \quad [5]$$

It is found that the following identity holds between the observed values y_k and the predicted values y_k^*

$$y_k^* = \sum_{j=1}^m (-1)^{j+1} \binom{m}{j} [y_j + \theta^j (y_j^* - y_j)] \quad [6]$$

This identity may be employed as a prediction formula, and we term it "the short formula of prediction." Thus the predicted value is given as a linear function of the last m observed values and the last m predicted values. Of course the short formula and the long formula are basically equivalent.

It is seen that the short formula for y_k^* is

$$y_k^* = \sum_{j=1}^m (-1)^{j+1} \binom{m}{j} [y_{j+k} + \theta^j (y_{j+k}^* - y_{j+k})] \quad [7]$$

For $k = 0$ this reduces, of course, to Equation [6]. For $k = -1$ it would appear that Equation [7] cannot be applied because y_0 is not known. However, if we assume $y_0 = y_0^*$, then Equation [7] does yield a value for y_{-1}^* . It can be shown, moreover, that $y_{-1}^* = p(-1)$ where $p(x)$ is the polynomial minimizing Equation [2]. This process can be continued to obtain $y_{-2}^* = p(-2)$, and so forth. It is thereby seen that the prediction formula [7] is not limited to one-step predictions.

Automatic Scrutiny

The programming of the finite prediction formula for a digital computer presents no difficulties. It is first necessary to select a starting index $k = K$. Thus y_K^* is to be the first prediction. The values of $y_{K+1}^*, \dots, y_{K+m}^*$ appearing in Equation [7] are not known. Let us assume them to be equal to y_{K+1}, \dots, y_{K+m} , respectively. This is essentially the same as assuming that the values of y_n for $n > K$ are given by a certain polynomial. This method of starting has the desirable property of giving perfect prediction if y_n is actually defined by a polynomial of degree less than m .

In the programming of [7], provision can be made for scrutiny of the data. Suppose by theoretical or empirical means an estimate can be made of the standard deviation of y_n , say $\sigma(y_n)$. Then if

$$|y_n^* - y_n| > 3\sigma(y_n) \quad [8]$$

y_n is considered to be a blunder and is replaced by y_n^* . The factor 3 in relation [8] is merely a conventional value.

A common type of excess error is a missing observation. For example, it may be that at some periods a missile whose path is being observed is obscured by clouds. Thus if y_n is lost, it is replaced by y_n^* , and the program proceeds. Presumably a fair number of gaps in the data can be bridged in this way.

We have been speaking of prediction as if it were occurring in "real time." However, it may be used to speed certain types of data processing. It could be used to locate the probable position of a missile in a series of photographs.

For other applications this automatic program could be employed solely as a scrutator. Then the short formula would serve to reject blunders and to fill in gaps in a data sequence.

Specific Example

To obtain a quantitative feeling for the prediction problem, it is of value to consider a specific example. To this end we give the simple case of straight line prediction, $m = 2$. We somewhat arbitrarily select $\theta = 0.8$. Table 1 displays $Q(x) = (0.8)^x (9 - x)/16$ to eight decimal places. Since $\sum [Q(n)]^2 = 221/729$, the variance of the prediction would be about three tenths of the variance in the observations.

Thermally Induced Bond Stresses in Case-Bonded Propellant Grains¹

ERIC E. UNGAR² and
BERNARD W. SHAFFER³

New York University, New York, N. Y.

Expressions are presented for the stresses induced by radial temperature gradients in assemblies consisting of cylindrical propellant grains which are bonded to thin walled casings. Very long and very short assemblies are studied under the condition of sudden environmental change. It is shown that under otherwise identical conditions the bond stress in a very long assembly always exceeds that in a very short assembly. An optimization study indicates the effect of geometry and material properties on the maximum stress in the bond.

THE PROBLEM of thermal stresses in an infinite, hollow, case bonded cylinder was analyzed in detail in a recent, very elegant paper by Zwick (1).⁴ As he pointed out, the solution of this problem may be used to approximate the stresses in a long but finite propellant grain and case assembly. The solution is not directly applicable, however, to the many practical designs where the length of the grain is of the same order of magnitude as the diameter.

A completely general analysis, dealing with the thermally induced stresses in cylindrical propellant and case assemblies of all possible length to diameter ratios, appears to be so complex as to be infeasible at present. However, the problem of very short assemblies may be solved with relative ease. Once the stress solution for both very long and very short assemblies are available, they may provide a guide for the design of practical units.

This note presents the solutions applicable to very long and to very short assemblies, with emphasis on those assemblies having casings that are elastically stiff but thermally thin. In addition, the stresses in the bonds joining the propellant grains to their casings are discussed in detail, with a view toward determining design criteria which can be used to minimize these stresses. Further, the relation between the

bond stresses in very long and very short assemblies is established in order to demonstrate the effect of length.

Thermal Stresses in Very Long and Very Short Assemblies

Let us consider a cylindrical propellant grain of inside radius a ; it is bonded at its outside radius b to a casing whose inside radius is also b and whose outside radius is c . It is assumed that the stresses and deformations, resulting when the assembly is subjected to temperature changes, are small enough so that the Hooke's law may be used in the analysis of the entire assembly. We also assume that the temperature rise everywhere in the assembly (as measured from the tem-

Received Nov. 2, 1959.

¹ The research presented in this note was sponsored by the Allegany Ballistics Laboratory under Bureau of Ordnance, Department of the Navy Contract no. NOrd - 16640, with New York University. The results shown in this note were originally presented in References (2 and 3).

² Formerly Assistant Professor of Mechanical Engineering; presently Senior Engineering Scientist, Bolt Beranek and Newman, Inc., Cambridge, Mass.

³ Professor of Mechanical Engineering.

⁴ Numbers in parentheses indicate References at end of paper.

perature corresponding to the stress free condition of the assembly) is a function of only the radial coordinate r , that is, $T = T(r)$.

Throughout the discussion the subscript P refers to the propellant grain, and the subscript C to the casing. The expressions for the radial stresses σ_r and the circumferential stresses σ_θ resulting from analysis of very long cylinders (generalized plane strain) or from very short cylinders (plane stress) may conveniently be written (1,2,3) as

$$\begin{aligned}(\sigma_r)_P &= k_P[(1 - a^2/r^2)(T_P + W_P) - \bar{T}_P] \\ (\sigma_\theta)_P &= k_P[(1 + a^2/r^2)(T_P + W_P) + \bar{T}_P - 2T] \\ (\sigma_r)_C &= k_C[(1 - c^2/r^2)(T_C + W_C) - \bar{T}_C] \\ (\sigma_\theta)_C &= k_C[(1 + c^2/r^2)(T_C + W_C) + \bar{T}_C - 2T]\end{aligned}\quad [1]$$

where r denotes the radial coordinate, T the local temperature rise, and where

$$\begin{aligned}r^2 T_P(r) &= 2 \int_a^r T(\rho) \rho d\rho \\ r^2 T_C(r) &= 2 \int_c^r T(\rho) \rho d\rho \\ T_P(1 - a^2/b^2) &= T_P(b) \\ T_C(1 - c^2/b^2) &= T_C(b)\end{aligned}\quad [2]$$

so that T_P and T_C denote the mean temperature of the propellant grain and of the case, respectively.⁵ Further, for short assemblies

$$k = \alpha E / 2$$

and for long assemblies

$$k = \alpha E / 2(1 - \mu) \quad [3]$$

where

$$\begin{aligned}\alpha &= \text{linear thermal expansion coefficient} \\ E &= \text{modulus of elasticity} \\ \mu &= \text{Poisson's ratio}\end{aligned}$$

Of course, properties of the propellant must be used to evaluate k_P , and those of the case to calculate k_C . Also, for short assemblies

$$W_P = \frac{(\alpha_C T_C - \alpha_P T_P)/\alpha_P}{1 - \left(\frac{1 + \mu_P}{2}\right)\left[1 - \frac{a^2}{b^2}\right] + \frac{E_P}{E_C}\left[\frac{b^2 - a^2}{c^2 - b^2} + \left(\frac{1 + \mu_C}{2}\right)\left(1 - \frac{a^2}{b^2}\right)\right]} \quad [4a]$$

for long assemblies

$$W_P = \frac{(\alpha_C T_C - \alpha_P T_P)/\alpha_P}{1 - \frac{\beta}{1 - \mu_P} + \frac{E_P}{E_C}\left[\frac{b^2 - a^2}{c^2 - b^2}\right]\left(\frac{1 - \mu_C - \beta}{1 - \mu_P}\right)} \quad [4a]$$

where

$$\begin{aligned}\beta &= \frac{1}{2}\left[1 - \frac{a^2}{b^2}\right]\left[1 - \left(\frac{b^2 - a^2}{c^2 - a^2} + \epsilon\right)^{-1}\right] \\ \epsilon &= \frac{E_C}{E_P}\left[\frac{1 + \mu_P}{1 + \mu_C}\right]\left[\frac{c^2 - b^2}{c^2 - a^2}\right]\end{aligned}\quad [4b]$$

and

$$\frac{W_C}{W_P} = \frac{k_P}{k_C} \left[\frac{b^2 - a^2}{b^2 - c^2} \right] \quad [5]$$

The latter applies for long and short assemblies, provided the proper expressions for k are chosen from Equations [3].

⁵ The notation defined in Equations [2], introduced by Zwick (1), serves to simplify the analysis.

The stress in the bond may be determined by setting $r = b$ in the radial stress expressions of Equations [1] and in the auxiliary Equations [2]. One then finds that

$$\sigma_b = k_P(1 - a^2/b^2)W_P = k_C(1 - c^2/b^2)W_C \quad [6]$$

which of course agrees with Equation [5], and thus indicates satisfaction of radial stress continuity at the propellant case interface at $r = b$.

Assemblies With Elastically Stiff, Thermally Thin Casings

For the many practical instances where the casing is much stiffer than the propellant, as exhibited by the fact that $E_C \gg E_P$, one may note that

$$\frac{E_C}{E_P} \left[\frac{c^2 - b^2}{c^2 - a^2} \right] \gg 1 \quad \frac{E_C}{E_P} \left[\frac{c^2 - b^2}{b^2 - a^2} \right] \gg 1 \quad [7]$$

so that the expressions of Equation [4a] may be replaced by the approximations

$$W_P = \frac{(\alpha_C T_C - \alpha_P T_P)/\alpha_P}{1 - (1/2)(1 - a^2/b^2)\eta} \quad [8a]$$

where for short assemblies

$$\eta = 1 + \mu_P$$

for long assemblies

$$\eta = 1/(1 - \mu_P) \quad [8b]$$

and the ratio expressed in Equation [5]

$$W_C/W_P \ll 1 \quad [9]$$

Extreme Stress Conditions

Zwick's proof (1) of the monotonic variation of temperature with time throughout the grain of a propellant and case assembly with a stiff but thermally thin case, applies equally well to assemblies of all lengths, as long as purely radial temperature gradients are assumed. Consequently the maximum stress conditions must occur either immediately upon immersion of the assembly in a new temperature environment, or after a long period of immersion. If the environmental temperature is an amount T_0 above the temperature corresponding to the stress free assembly, the initial stresses may be evaluated on the basis that the temperature throughout the propellant grain has not yet had time to change, whereas the thermally thin case assumes the temperature of the surrounding environment instantaneously upon exposure.

The initial stresses may thus be computed by setting $T = T_P = \bar{T}_P = 0$ in the first two of Equations [1] and in Equation [8a], and by setting $T = T_C = T_0$ in the last two of Equations [1], in Equation [2] and in Equation [8a]. The results may, in view of Equation [5], conveniently be summarized as

$$\begin{aligned} [(\sigma_r)_P]_{t=0} &= (1 - a^2/r^2)N \\ [(\sigma_\theta)_P]_{t=0} &= (1 + a^2/r^2)N \\ [(\sigma_r)_C]_{t=0} &= \left[1 - \frac{c^2}{r^2} \right] \left[\frac{b^2 - a^2}{b^2 - c^2} \right] N \\ [(\sigma_\theta)_C]_{t=0} &= \left[1 + \frac{c^2}{r^2} \right] \left[\frac{b^2 - a^2}{b^2 - c^2} \right] N \end{aligned} \quad [10]$$

where

$$N = \frac{k_P T_0 \alpha_C / \alpha_P}{1 - (1/2)(1 - a^2/b^2)\eta} \quad [11]$$

and η obeys Equations [8b].

Similarly, the stresses occurring after a long period of immersion may be computed by setting $T = T_P = T_C = T_0$ in Equations [1,2 and 8]. One finds that the final stresses under

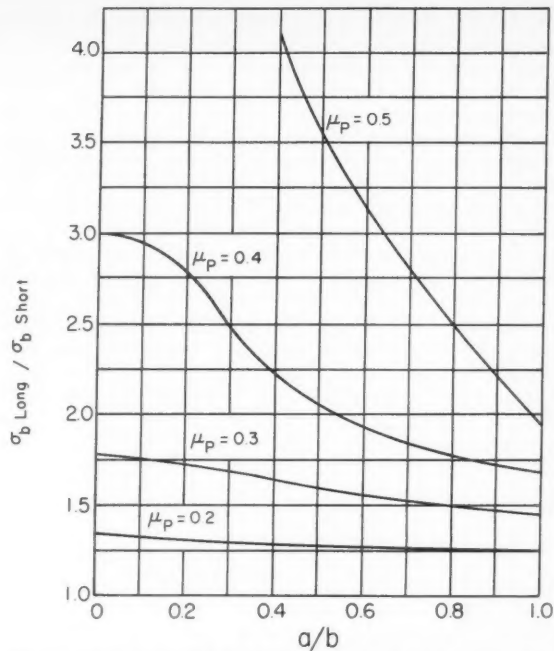


Fig. 1 Variation of ratio of bond stress in long assembly to bond stress in short assembly with ratio of propellant inside to outside radius, for several values of propellant Poisson's ratio

all circumstances are simply related to the initial stress in accordance with the expression

$$[(\sigma_i)_j]_{t \rightarrow \infty} = (1 - \alpha_P/\alpha_C)[(\sigma_i)_j]_{t=0} \quad i = r, \theta \quad j = P, C \quad [12]$$

The bond stresses corresponding to the foregoing conditions may, of course, be computed simply by setting $r = b$ in the appropriate radial stress expressions.

Bond Stress Optimization

In many practical instances the bond between the propellant and the case is considerably weaker than either of these two components, so that evaluation of the maximum bond stress becomes particularly important. Compressive failure of the bond is extremely unlikely and need not be considered further, but tensile bond stresses may be significant and warrant further analysis. If the environmental temperature is greater than that at which the assembly is stress free, then T_0 is positive and the initial bond stress is positive (i.e., tensile) in view of the first of Equations [10] and Equation [11]. Inspection of Equation [12] then reveals that the final bond stress is negative if α_P is greater than α_C , and that it is positive but less than the initial stress if α_P is less than α_C . On the other hand, for negative values of T_0 (which correspond to conditions where the environment is at temperatures which are lower than that of the stress free state) the initial and the final bond stresses both are compressive, unless α_P is greater than α_C . In the latter case the final stress is tensile. In summary then, the maximum tensile bond stress is

$$\sigma_{b_{\max} \text{ tensile}} = \begin{cases} (1 - a^2/b^2)N & \text{for } T_0 > 0 \\ 0 & \text{for } \alpha_P > \alpha_C \\ (1 - \alpha_P/\alpha_C)(1 - a^2/b^2)N & \text{for } \alpha_P < \alpha_C \end{cases} \quad [13]$$

where N is given in Equation [11].

The designer may naturally raise the question as to what may be done to decrease the maximum tensile bond stress

that occurs with given environmental conditions without altering the physical or geometric properties of the propellant grain. Inspection of Equations [11 and 13] indicates that for positive T_0 the maximum tensile bond stress may be reduced by selecting a casing material with a lower thermal expansion coefficient α_c , whereas the final tensile bond stress (if it is nonzero) may be reduced by selecting a casing material whose thermal expansion coefficient approaches that of the propellant. Further, from Equations [6] used in conjunction with Equations [4], one may determine that the bond stress under all conditions may be decreased by the use of a casing having a lower modulus of elasticity, as may be expected intuitively.

The effect of the Poisson's ratio of the casing material is not obvious from inspection of the previous equations, but may be determined by differentiation of the bond stress expressions of Equations [6] with respect to μ_c . One finds that an increase in μ_c leads to an increase in the bond stress of long assemblies and to a decrease in the bond stress of short assemblies. The aforementioned derivatives, however, are found to have very small absolute values for assemblies with stiff casings, so that the effect of μ_c on the bond stress is virtually negligible.

Of course, practical assemblies are neither infinitely long nor infinitesimally thin, so it is necessary that the previously listed results be applied judiciously. In order to compare the values one obtains for bond stresses in units which are identical except for length and which are subject to the same temperatures, one may use Equations [6] in conjunction with Equations [3 and 8] to determine the ratio of the bond stress in an infinitely long, to that in an infinitesimally short, unit

$$\frac{\sigma_b \text{ long}}{\sigma_b \text{ short}} = \frac{2 - (1 - a^2/b^2)(1 + \mu_p)}{1 + a^2/b^2 - 2\mu_p} \quad [14]$$

This equation, which is plotted in Fig. 1 as a function of a/b for several values of μ_p , reveals that this ratio approaches

unity as μ_p approaches zero, but that the ratio increases with μ_p and is considerably greater than unity for practical values of μ_p . Calculations based on the assumption of an infinitely long assembly thus always lead to bond stress values which are greater than those calculated for a very short assembly.

Concluding Remarks

It has been demonstrated that the bond stress induced in a very long assembly always exceeds that induced in a similar but very short assembly under identical conditions; this fact may be a useful guide for design purposes.

It is interesting to note also that a number of conclusions were found to be equally valid for very short and for very long assemblies. These conclusions pertain to assemblies with elastically stiff but thermally thin casings and are:

1 All thermally induced stresses attain their maximum (absolute) values either immediately when the assembly is subjected to a new environmental temperature, or else after a long exposure.

2 The bond stresses obtained in a given assembly, when the grain configuration and propellant material cannot be changed, may be reduced by selecting a case which: Is thinner, has a smaller modulus of elasticity, and has a smaller linear thermal expansion coefficient (to reduce the initial stress) and one more nearly equal to that of the propellant (to reduce the final stress).

3 The bond stresses are virtually unaffected by changes in the Poisson's ratio of the casing material.

References

1 Zwick, S. A., "Thermal Stresses in an Infinite, Hollow Case-Bonded Cylinder," *JET PROPULSION*, vol. 27, no. 8, Aug. 1957, pp. 872-876.

2 Ungar, E. E. and Shaffer, B. W., "Thermal Stresses in Long Cylindrical Case-Bonded Propellant Grains," New York University Tech. Rep., prepared for Allegany Ballistics Lab. under U. S. Navy Bureau of Ordnance Contract no. NOrd-16640, Sept. 1958.

3 Ungar, E. E. and Shaffer, B. W., "Thermal Stresses in Propellant Disks Bonded to Cylindrical Casings," New York University Tech. Rep., prepared for Allegany Ballistics Lab. under U. S. Navy Bureau of Ordnance Contract no. NOrd-16640, May 1957.

Short Hypersonic Contour Nozzles

R. E. GEIGER¹

General Electric Co., Missile and Space Vehicle Dept., Philadelphia, Pa.

IT IS well known that the lengths of hypersonic nozzles contoured to produce uniform test section flows are often prohibitive. In such a nozzle the flow along the centerline very rapidly expands to the desired test section conditions, and the remainder of the nozzle is devoted to bringing the rest of the flow to these conditions. The rate at which the uniform flow region widens with nozzle length is, of course, given by the tangent of the test section Mach angle. For hypersonic Mach numbers, where the Mach angle is very low, this section of the nozzle constitutes a major portion of the total nozzle length. Some illustrative values are shown in Fig. 1 for a family of axisymmetric nozzles² computed by WADC.³ It is evident that elimination of a significant fraction of this

Received Nov. 4, 1959.

¹ Advanced Aerodynamics, Space Sciences Laboratory.

² Nozzles whose initial contour downstream of the throat is taken as conical and in which pure source flow is assumed.

³ Cresci, R. J., "Tabulation of Coordinates for Hypersonic Axisymmetric Nozzles, Part I—Analysis and Coordinates for Test Section Mach Numbers of 8, 12, and 20," WADC Tech. Note 58-300 Part I (ASTIA 204 213), Oct. 1959.

terminal portion of the hypersonic nozzle represents a significant saving in total nozzle length.

If a test section flow can be tolerated in which the central "core" is uniform and the remainder is slightly nonuniform, then such a reduction in total nozzle length can be achieved. Such a nozzle would be determined in the following manner. For a given contour, choose the desired uniform core diameter (see Fig. 2). From this diameter on the exit characteristic, Point A, trace along the upstream characteristic to the nozzle wall, Point B. This is the nozzle contour cutoff point, downstream of which any deviations of the wall from the original contour will not be felt inside the test section uniform center core provided these deviations do not initially (i.e., immediately downstream of the contour cutoff point) produce a wall more concave than the original contour. If greater concavity is permitted somewhat further downstream of the cutoff point, it cannot be sufficient to produce a shock that would intrude upon the model flow field. If the axial location of the chosen core diameter on the exit characteristic is taken as the nozzle exit, the length of the shortened nozzles for the WADC contours may be readily calculated. Ratios of these lengths to the full nozzle lengths are presented (Fig. 3) as a function of Mach number for various initial wall angles. For comparison, Fig. 3 of Cresci's paper is reproduced in Fig. 4. It gives the full nozzle lengths in terms of exit or test section diameters. The savings in nozzle length shown in Fig. 3 are noteworthy.

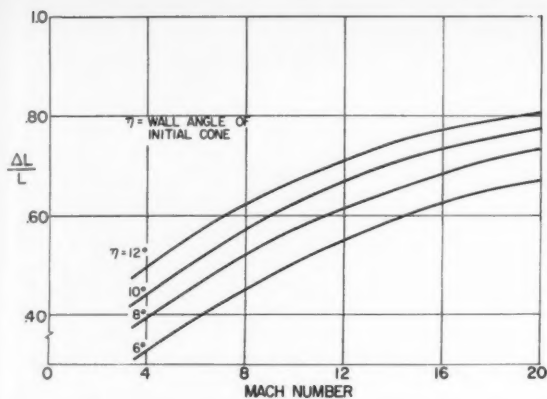


Fig. 1 Length of final Mach cone as fraction of total length for WADC nozzles

The practical value of these considerations is certainly a function of the degree of test section flow nonuniformity outside the chosen uniform core. This will, of course, depend on the wall shape between the exact contour cutoff point and the exit of the shortened nozzle. Without solutions of the flow in specific nozzle shapes, it is not possible to state with quantitative precision the extent of these nonuniformities. However, for a test section uniform core diameter of 0.4 times the test section diameter, or greater, an examination of the Mach 12 and 20 WADC contours and consideration of appropriate Mach angles strongly suggests that the worst case (Mach 12, initial cone angle of 12 deg) would be a conefrustum of about 3.5-deg wall angle between the exact contour cutoff point and the exit. In such a nozzle, the flow angle of the outer six-tenths of the test section flow would vary from zero to about 3.5 deg at the wall, which is a considerable improvement over a conical nozzle flow. Furthermore, since the major portion of the expansion takes place in the upstream section of the nozzle, the axial gradients in the nonuniform flow outside the center core will be very much less than at the corresponding point at the exit of a purely conical nozzle. The case for the short nozzle is even stronger at higher Mach number, lower initial cone angle and (especially) larger uniform flow cores, since for these nozzles the wall angle at the test section would be significantly less than 3.5 deg.

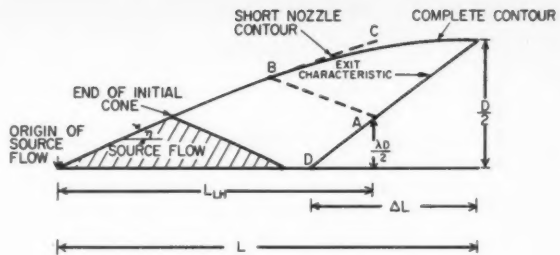


Fig. 2 Schematic sketch of contour nozzle flow

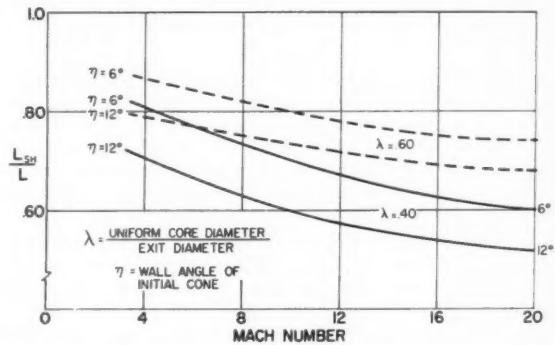


Fig. 3 Length of shortened nozzle as fraction of full length for WADC nozzles

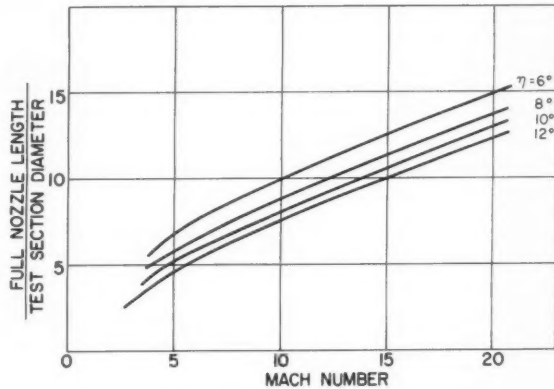


Fig. 4 Full length of WADC contour nozzles

Design Method for Spherical Grains

H. M. SEGAL¹

Aerojet-General Corp., Sacramento, Calif.

This paper presents a simplified method for obtaining the burning area of a spherically shaped grain. With this information the thrust-time curve can be plotted. A descriptive geometry rather than a mathematical approach was taken because it can be developed easily and does not require extensive calculations. This method will describe the burning characteristics not only of a spherical motor but also of the hemispherical or elliptical portion of a cylindrical motor. The application of this method is demonstrated for a 20-in. diameter spherical grain.

A SIMPLE method has been developed for predicting the performance of spherical motors. Since this method is applicable to any spherical configuration, it can also be used to describe the burning characteristics of the hemispherical ends of a cylindrical motor. With minor modification this method can be used to predict the performance of other shaped grains (ellipses, cassanian ovals, etc.).

In order to analyze the grain, two approaches are possible: The burning area can be calculated mathematically, or the burning area can be presented by means of descriptive geometry.

The mathematical approach is complex, costly and time consuming; however, the descriptive geometry approach is simple, fast and inexpensive. Using this method no complex mathematics, expensive computer operation or high priced engineering talent is needed to analyze the grain. Within two days a draftsman can generate the information needed to plot the required thrust-time curve.

The burning area at various times is obtained by projecting the lines which encompass a given burning area into a true length view. These lines can be broken up into increments, laid out in flat pattern and measured with a planimeter.

Application of a Descriptive Geometry Analysis to the Design of a Spherical Motor

A 20-in. OD spherical motor with a star-shaped grain, as shown in Fig. 1, has been selected for illustration.

Analysis of burning process

The first problem is to determine how the grain regresses during burning. Fig. 1 shows the grain pattern at a cross section along the equator of the sphere. It can readily be seen that burning proceeds in two distinct phases.

Phase one encompasses the time from ignition to web burnout; that is, to the moment when the flame first touches the chamber wall. During this time, since the burning areas remain essentially the same (neutral burning), burning rates are constant and pressures and thrust can be obtained by a simple proportional relationship.

In phase two (Fig. 2) the silver is burning out. Since the burning area is diminishing rapidly, the neutral condition present in phase one no longer exists. Now thrust and pressure are no longer proportional to burning area, and a more involved analysis is needed.

Attempt to determine the burning area

Because burning of the grain occurs in two distinct phases, the analysis must be carried out in the two steps previously described.

Phase one: Let us consider the end condition of this phase, the moment when the flame first touches the chamber wall. The total burning area at this time is analogous to the surface

area of a pumpkin, made up of various ripples. The problem is to find the surface area of such a ripple. This is done by dividing the ripple into four equal parts (see Fig. 2), a simplifying operation which enables us to obtain the true length of the three lines which encompass the desired area. Once the true lengths of these lines have been obtained, they can be broken up into increments and laid out into a flat pattern which can be measured with a planimeter.

Let us select, as an example, a typical burnback area, such as burnback area "E," represented by the shaded portion in Fig. 2. Line E_1, E_1 is a part of circle with the known radius (r_1). Line E_1, E_5 , is a circle segment within the torus of radius (r_2) and therefore also known. The problem then is to find the true length of the remaining line E_5, E_1 . The true length of this line is shown in Fig. 3 as line E_1, E_5 in view 2, which is a projection from view 1. The true lengths of these three lines have now been obtained; if they can be spread out in a flat pattern, the area they circumscribe can be measured. This has been done, as can be seen in view 3. This cycle can then be repeated for burnback areas D, C, B and A and these burning areas can then be plotted into a thrust-time curve for this phase of motor firing.

Phase two: Silver burnout begins at the time when the flame first touches the walls of the chamber. At this time, the burning areas at web burnout and at the beginning of tailoff are equal. Pressure and, consequently, the burning rate at this instance are known. However, as burning progresses, the silver diminishes rapidly. As a result the pressure within the

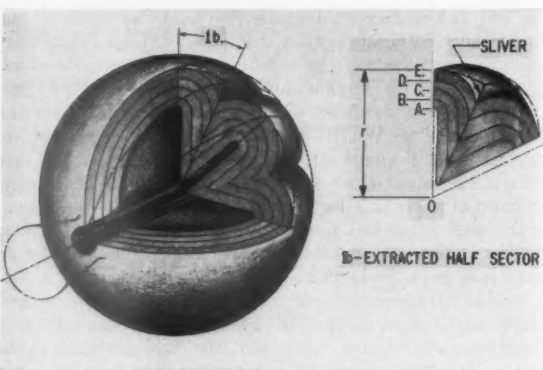


Fig. 1 Burning area of a spherical grain

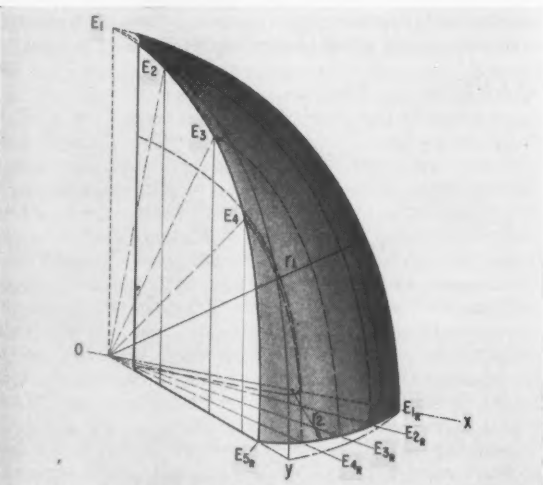


Fig. 2 Quarter section of spherical grain segment showing burning area at burnback position E

Received Oct. 29, 1959.

¹ Design Engineer, Proposal Division.

sphere drops sharply, which in turn slows down the burning rate.

Now when we trace the burning intervals during sliver burnback, these distances do not represent uniform time periods. The burning rate is no longer constant. While this nonuniform burning complicates the analysis slightly, the same concepts can be used to obtain the thrust-time curve during sliver burnout. First the burning area for each of the selected sliver burnback positions is determined by the method described in phase one. Chamber pressures and burning rates are then calculated by substituting these measured values in the mass balance equation. Therefore, the rate at which the sliver propellant is consumed between two burnback positions is the average of the burning rate at these two positions. A relationship has thus been established between the geometrical distance between burnback position and the time it takes the flame front to move between them.

Practical application

One of the requirements for the hypothetical spherical motor was an essentially neutral thrust-time curve. Since thrust and burning area are approximately proportional until web burnout, our problem is to establish that at each moment of motor firing the burning areas are equal.

First we assume that the burning area at web burnout would be equal to the surface area of the sphere. Since this grain must be neutral burning, we then designed the port area to be equal to this figure. To do this it was necessary to assume a web and ray thickness.

Now the grain was graphically laid out and the burning areas were projected with the help of the Modified Gore Layout, as previously described. The layout method produces burning area considerably less than the assumed value but this must be expected since the overall purpose of the first grain design is to establish sliver volume, port volume, and an indication of burning area neutrality.

Using this new burning area and anticipating what the new loading would be, a new cycle of ballistic calculations was made which resulted in a slightly different web thickness. Using this data, a final layout was made, and the desired thrust-time curve was plotted.

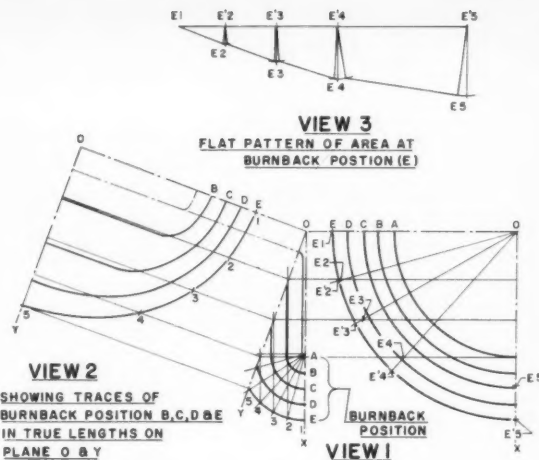


Fig. 3 Flat pattern layout of burning area of a spherical grain

Conclusion

The approach which has been used is that of a descriptive geometry analysis conducted in the following way: By projecting the lines which encompass a given burning area, the true lengths of these lines are determined. Breaking them up into increments, area segments are drawn which are then measured with a planimeter.

While it is fully realized that a more sophisticated method based on mathematical philosophies is needed, the method presented will provide the preliminary design engineer with a fast, sufficiently accurate means for predicting the performance of spherical grains.

Curves for Rapid Determination of Orbital Transfer Requirements

PHILIP J. BONOMO¹

Westinghouse Electric Corp., Baltimore, Md.

Nondimensional curves are presented which permit the determination of minimum energy requirements for orbit to orbit transfer in a central force field. The curves are general and apply to minimum energy transfers with any body (Earth, sun, etc.) as the primary gravitational source. Four examples are given to illustrate the utility of the curves: Transfer from a 1000-mile Earth orbit to an orbit in the vicinity of the moon, successive transfers from a 200-mile Earth orbit to a 22,400-mile "stationary" orbit, and interplanetary transfer from Earth to Mars and from Earth to Venus (Hohmann transfer ellipses).

Received Oct. 29, 1959.

¹ Engineer, Space Studies Group, Air Arm Division.

APRIL 1960

TRANSFER from one Keplerian orbit to another within a central force field is effected by modification of the velocity vector of the transferring body. In a two-body situation, a unique velocity, corresponding to a circular orbit, is associated with each radius r above the center of the primary gravitational source; i.e., V_{circle} is proportional to the square root of 1 over r . Variations in this velocity will modify the circular orbit into an elliptical orbit of major axis greater or less than the diameter of the circular orbit. A decrease in velocity will result in an interior ellipse, while an increase in velocity will result in an exterior ellipse. The maximum increase in velocity is limited, for transfer purposes, to the escape velocity associated with the radius of the circular orbit ($V_{\text{escape}} = \sqrt{2} V_{\text{circle}}$). These facts permit transfer from one circular (or elliptical, if transfer is initiated at perigee or apogee) orbit to another and form the basis of the transfer requirement curves described next.

An orbital transfer problem is specified by λ and the transfer requirements are given by k and ϵ .²

² See Nomenclature.

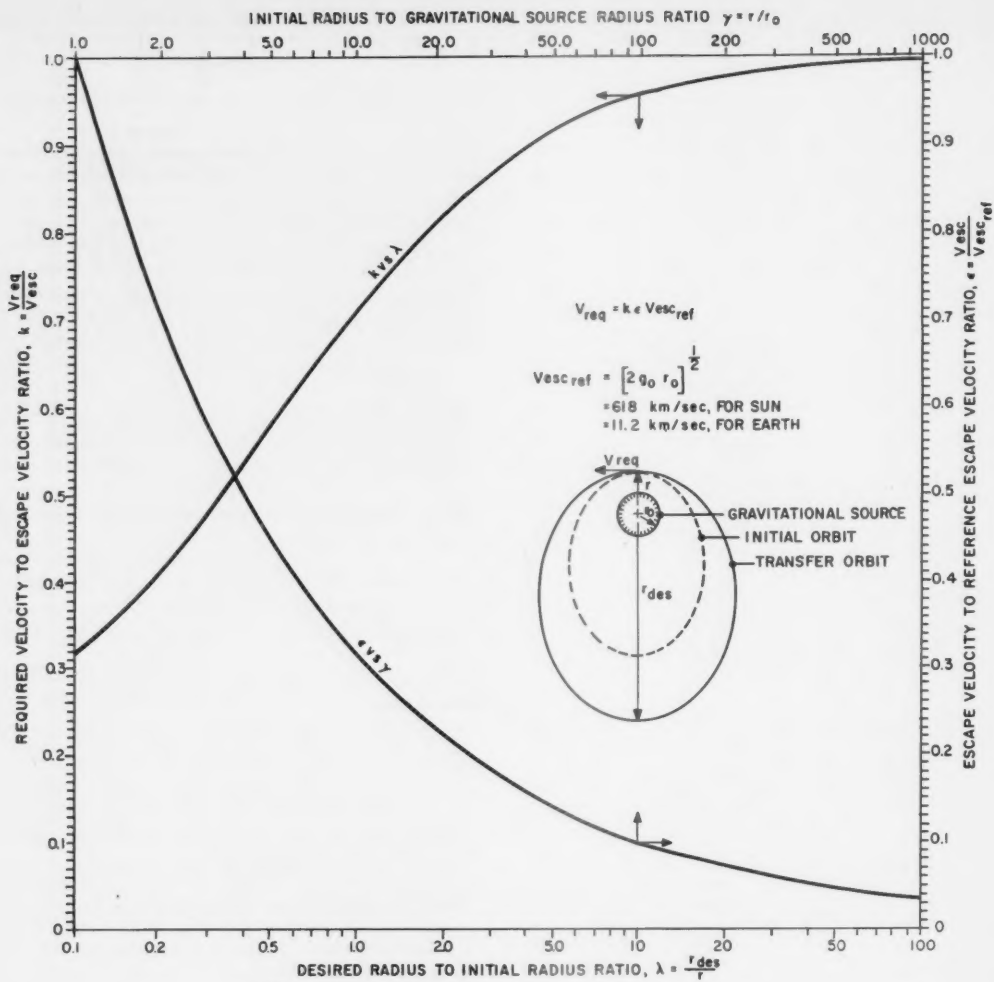


Fig. 1 Transfer requirement curves: k vs. λ , ϵ vs. γ

Development of Curves

The velocity at any point in an elliptical orbit is given by

$$V^2 = u \left(\frac{2}{r} - \frac{1}{a} \right) \quad [1]$$

and the escape velocity associated with the radius r by

$$V_{esc}^2 = \frac{2u}{r} = \frac{2g_0 r_0^2}{r} \quad [2]$$

Assume that the initial orbit is circular (or that the initial orbit is elliptical with transfer initiated at perigee or apogee), and that the velocity of the orbiting body is instantaneously changed; the orbiting body will then enter a transfer elliptical orbit. Assume further that the new total velocity V_{req} is some fraction k of the escape velocity associated with the initial radius r ($k < 1.0$). Then from Equations [1] and [2]

$$V_{req}^2 = u \left(\frac{2}{r} - \frac{1}{a} \right) = k^2 V_{esc}^2 = k^2 \left(\frac{2u}{r} \right) \quad [3]$$

The initial radius r and the desired radius r_{des} will be either the perigee and apogee or apogee and perigee radii of the transfer ellipse (depending on whether $r_{des}/r > 1$ or $r_{des}/r < 1$). In either case, for an ellipse

$$2a = r_p + r_a = r + r_{des} \quad [4]$$

Combining Equations [3] and [4] and solving for k

$$k^2 = 1 - \frac{r}{2a} = \frac{2a - r}{2a} = \frac{r_{des}}{r + r_{des}}$$

Defining λ as the desired radius to initial radius r_{des}/r , k may be expressed as

$$k = \left[\frac{\lambda}{1 + \lambda} \right]^{1/2} \quad [5]$$

From Equation [2]

$$\frac{V_{esc}^2}{2g_0 r_0} \equiv \frac{V_{esc}^2}{V_{esc_ref}^2} = \frac{1}{r/r_0}$$

or

$$\epsilon = (\gamma)^{-1/2} \quad [6]$$

where ϵ and γ are as defined below. Note that $V_{req} = k \epsilon V_{esc_ref}$. Also, since $r_a V_a = r_p V_p$ for an ellipse, the velocity V at r_{des} is given by

$$V = \frac{r}{r_{des}} V_{req} = \frac{V_{req}}{\lambda} \quad [7]$$

Equations [5 and 6], which are plotted in Fig. 1, together with Equation [7], are sufficient to determine the velocity requirements for transfer from one orbit to another, as will be illustrated. Since all quantities are nondimensional, the equations apply for any two-body transfer situation.

Illustrative Examples

Four examples illustrate the application of Fig. 1.

(Continued on page 421)

y
l
l
= y
l
h
-
L